



**GEOFORSCHUNGSZENTRUM POTSDAM**  
STIFTUNG DES ÖFFENTLICHEN RECHTS

---

# Scientific Technical Report

ISSN 1610-0956

Combined structural and magnetotelluric investigation across  
the West Fault Zone in northern Chile

---

Dissertation  
zur Erlangung des akademischen Grades  
Doktor der Naturwissenschaften (Dr. rer. nat.)  
in der Wissenschaftsdisziplin Geowissenschaften

eingereicht an der  
Mathematisch-Naturwissenschaftlichen Fakultät  
der Universität Potsdam

Arne Hoffmann-Rothe

Potsdam, April 2002

---

## Abstract

The characterisation of the internal architecture of large-scale fault zones is usually restricted to the outcrop-based investigation of fault-related structural damage on the Earth's surface. A method to obtain information on the downward continuation of a fault is to image the subsurface electrical conductivity structure.

This work deals with such a combined investigation of a segment of the West Fault, which itself is a part of the more than 2000 km long trench-linked Precordilleran Fault System in the northern Chilean Andes. Activity on the fault system lasted from Eocene to Quaternary times. In the working area (22°04' S, 68°53' W), the West Fault exhibits a clearly defined surface trace with a constant strike over many tens of kilometers. Outcrop condition and morphology of the study area allow ideally for a combination of structural geology investigation and magnetotelluric (MT) / geomagnetic depth sounding (GDS) experiments. The aim was to achieve an understanding of the correlation of the two methods and to obtain a comprehensive view of the West Fault's internal architecture.

Fault-related brittle damage elements (minor faults and slip-surfaces with or without striation) record prevalent strike-slip deformation on subvertically oriented shear planes. Dextral and sinistral slip events occurred within the fault zone and indicate reactivation of the fault system. Youngest deformation increments mapped in the working area are extensional and the findings suggest a different orientation of the extension axes on either side of the fault. Damage element density increases with approach to the fault trace and marks an approximately 1000 m wide damage zone around the fault. A region of profound alteration and comminution of rocks, about 400 m wide, is centered in the damage zone. Damage elements in this central part are predominantly dipping steeply towards the east (70-80°).

Within the same study area, the electrical conductivity image of the subsurface was measured along a 4 km long MT/GDS profile. This main profile trends perpendicular to the West Fault trace. The MT stations of the central 2 km were 100 m apart from each other. A second profile with 300 m site spacing and 9 recording sites crosses the fault a few kilometers away from the main study area. Data were recorded in the frequency range from 1000 Hz to 0.001 Hz with four real time instruments S.P.A.M. MkIII.

The GDS data reveal the fault zone for both profiles at frequencies above 1 Hz. Induction arrows indicate a zone of enhanced conductivity several hundred meters wide, that aligns along the WF strike and lies mainly on the eastern side of the surface trace. A dimensionality analysis of the MT data justifies a two dimensional model approximation of the data for the frequency range from 1000 Hz to 0.1 Hz. For this frequency range a regional geoelectric strike parallel to the West Fault trace could be recovered. The data subset allows for a resolution of the conductivity structure of the uppermost crust down to at least 5 km.

Modelling of the MT data is based on an inversion algorithm developed by Mackie et al. (1997). The features of the resulting resistivity models are tested for their robustness using empirical sensitivity studies. This involves variation of the properties (geometry, conductivity) of the anomalies, the subsequent calculation of forward or constrained inversion models and check for consistency of the obtained model results with the data. A fault zone conductor is resolved on both MT profiles. The zones of enhanced conductivity are located to the east of the West Fault surface trace. On the dense

MT profile, the conductive zone is confined to a width of about 300 m and the anomaly exhibits a steep dip towards the east (about 70°). Modelling implies that the conductivity increase reaches to a depth of at least 1100 m and indicates a depth extent of less than 2000 m. Further conductive features are imaged but their geometry is less well constrained.

The fault zone conductors of both MT profiles coincide in position with the alteration zone. For the dense profile, the dip of the conductive anomaly and the dip of the damage elements of the central part of the fault zone correlate. This suggests that the electrical conductivity enhancement is causally related to a mesh of minor faults and fractures, which is a likely pathway for fluids. The interconnected rock-porosity that is necessary to explain the observed conductivity enhancement by means of fluids is estimated on the basis of the salinity of several ground water samples (Archie's Law). The deeper the source of the water sample, the more saline it is due to longer exposure to fluid-rock interaction and the lower is the fluid's resistivity. A rock porosity in the range of 0.8 - 4% would be required at a depth of 200 m. That indicates that fluids penetrating the damaged fault zone from close to the surface are sufficient to explain the conductivity anomalies. This is as well supported by the preserved geochemical signature of rock samples in the alteration zone. Late stage alteration processes were active in a low temperature regime (<95°C) and the involvement of ascending brines from greater depth is not indicated. The limited depth extent of the fault zone conductors is a likely result of sealing and cementation of the fault fracture mesh due to dissolution and precipitation of minerals at greater depth and increased temperature.

Comparison of the results of the apparently inactive West Fault with published studies on the electrical conductivity structure of the currently active San Andreas Fault, suggests that the depth extent and conductivity of the fault zone conductor may be correlated to fault activity. Ongoing deformation will keep the fault/fracture mesh permeable for fluids and impede cementation and sealing of fluid pathways.

## Kurzfassung

Untersuchungen zur internen Architektur von großen Störungszonen beschränken sich üblicherweise auf die, an der Erdoberfläche aufgeschlossene, störungsbezogene Deformation. Eine Methode, die es ermöglicht Informationen über die Tiefenfortsetzung einer Störung zu erhalten, ist die Abbildung der elektrischen Leitfähigkeit des Untergrundes.

Die vorliegende Arbeit beschäftigt sich mit der kombinierten struktureologischen und magnetotellurischen Untersuchung eines Segmentes der 'West Fault'-Störung in den nordchilenischen Anden. Die West Fault ist ein Abschnitt des über 2000 km langen Präkordilleren-Störungssystem, welches im Zusammenhang mit der Subduktion vor der südamerikanischen Westküste entstanden ist. Die Aktivität dieses Störungssystem reichte vom Eozän bis in das Quartär. Der Verlauf der West Fault ist im Untersuchungsgebiet ( $22^{\circ}04' S$ ,  $68^{\circ}53' W$ ) an der Oberfläche klar definiert und weist über viele zehner Kilometer eine konstante Streichrichtung auf. Die Aufschlussbedingungen und die Morphologie des Arbeitsgebietes sind ideal für kombinierte Untersuchungen der störungsbezogenen Deformation und der elektrischen Leitfähigkeit des Untergrundes mit Hilfe magnetotellurischer Experimente (MT) und der erdmagnetischen Tiefensondierung (GDS). Ziel der Untersuchungen war es, eine mögliche Korrelation der beiden Meßmethoden herauszuarbeiten, und die interne Störungsarchitektur der West Fault umfassend zu beschreiben.

Die Interpretation von Sprödbbruch-Strukturen (kleinmaßstäbliche Störungen sowie Störungsflächen mit / ohne Bewegungslineationen) im Untersuchungsgebiet weist auf überwiegend seitenverschiebende Deformation entlang von subvertikal orientierten Scherflächen hin. Dextrale und sinistrale Bewegungsrichtungen können innerhalb der Störungszone bestätigt werden, was auf Reaktivierungen des Störungssystem schliessen läßt. Die jüngsten Deformationen im Arbeitsgebiet haben dehnen-Charakter, wobei die kinematische Analyse eine unterschiedliche Orientierung der Extensionsrichtung beiderseits der Störung andeutet. Die Bruchflächendichte nimmt mit Annäherung an die Störung zu und zeichnet einen etwa 1000 m breiten Bereich erhöhter Deformationsintensität um die Störungsspur aus (damage zone). Im Zentrum dieser Zone weist das Gestein eine intensive Alteration und Brekzierung auf, die sich über eine Breite von etwa 400 m erstreckt. Kleine Störungen und Scherflächen in diesem zentralen Abschnitt der Störung fallen überwiegend steil nach Osten ein ( $70-80^{\circ}$ ).

Innerhalb desselben Arbeitsgebietes wurde ein 4 km langes MT/GDS Profil vermessen, welches senkrecht zum Streichen der West Fault verläuft. Für die zentralen 2 km dieses Hauptprofils beträgt der Abstand der Meßstationen jeweils 100 m. Ein weiteres Profil, bestehend aus 9 Stationen mit einem Abstand von 300 m zueinander, quert die Störung einige Kilometer entfernt vom eigentlichen Arbeitsgebiet. Die Aufzeichnung der Daten erfolgte mit vier S.P.A.M MkIII Apparaturen in einem Frequenzbereich von 1000 Hz bis 0.001 Hz.

In den GDS Daten beider Profile ist die Störung für Frequenzen  $> 1$  Hz deutlich abgebildet: Die Induktionspfeile kennzeichnen eine mehrere hundert Meter breite Zone erhöhter Leitfähigkeit, welche sich entlang der West Fault erstreckt. Die Dimensionalitätsanalyse der MT Daten rechtfertigt die Anpassung der gemessenen Daten mit einem zwei-dimensionalen Modell für einen Frequenzbereich von 1000 Hz bis 0.1 Hz. In diesem Frequenzbereich, der eine Auflösung der Leitfähigkeitsstruktur bis mindestens 5 km Tiefe ermöglicht, läßt sich eine regionale geoelektrische Streichrichtung parallel zum Verlauf der West Fault nachweisen.

Die Modellierung der MT Daten beruht auf einem Inversionsalgorithmus von Mackie et al. (1997). Leitfähigkeitsanomalien, die sich aus der Inversions-Modellierung ergeben, werden anhand von empirischen Sensitivitätsstudien auf ihre Robustheit überprüft. Dabei werden die Eigenschaften (Geometrie, Leitfähigkeit) der Strukturen systematisch variiert und sowohl Vorwärts- als auch Inversionsrechnungen der modifizierten Modelle durchgeführt. Die jeweiligen Modellergebnisse werden auf ihre Konsistenz mit dem Ausgangsdatensatz überprüft. Entlang beider MT Profile wird ein guter elektrischer Leiter im zentralen Abschnitt der West Fault aufgelöst, wobei die Bereiche erhöhter Leitfähigkeit östlich der Störungsspur liegen. Für das dicht vermessene MT Profil ergibt sich eine Breite des Störungsleiters von etwa 300 m sowie ein steiles Einfallen der Anomalie nach Osten (70°). Der Störungsleiter reicht bis in eine Tiefe von mindestens 1100 m, während die Modellierungsstudien auf eine maximale Tiefenerstreckung < 2000 m hinweisen. Das Profil zeigt weitere leitfähige Anomalien, deren Geometrie aber weniger genau aufgelöst ist.

Die Störungsleiter der beiden MT Profile stimmen in ihrer Position mit der Alterationszone überein. Im zentralen Bereich des Hauptprofils korreliert darüber hinaus das Einfallen der Sprödbrechstrukturen und der Leitfähigkeitsanomalie. Dies weist darauf hin, daß die Erhöhung der Leitfähigkeit im Zusammenhang mit einem Netzwerk von Bruchstrukturen steht, welches mögliche Wegsamkeiten für Fluide bietet. Der miteinander in Verbindung stehende Gesteins-Porenraum, der benötigt wird, um die gemessene Erhöhung der Leitfähigkeit durch Fluide im Gestein zu erklären, kann anhand der Salinität einiger Grundwasserproben abgeschätzt werden (Archies Gesetz). Wasserproben aus größerer Tiefe, weisen aufgrund intensiverer Fluid-Gesteins-Wechselwirkung eine höhere Salinität, und damit eine verbesserte Leitfähigkeit, auf. Für eine Probe aus einer Tiefe von 200 m ergibt sich demnach eine benötigte Porosität im Bereich von 0.8-4%. Dies legt nahe, daß Wässer, die von der Oberfläche in die Bruchzone der Störung eindringen, ausreichen, um die beobachtete Leitfähigkeits-erhöhung zu erklären. Diese Deutung wird von der geochemischen Signatur von Gesteinsproben aus dem Alterationsbereich bestätigt, wonach die Alteration in einem Regime niedriger Temperatur (<95°C) stattfand. Der Einfluß von aufsteigenden Tiefenwässern wurde hier nicht nachgewiesen. Die geringe Tiefenerstreckung des Störungsleiters geht wahrscheinlich auf Verheilungs- und Zementationsprozesse der Bruchstrukturen zurück, die aufgrund der Lösung und Fällung von Mineralen in größerer Tiefe, und damit bei erhöhter Temperatur, aktiv sind.

Der Vergleich der Untersuchungsergebnisse der zur Zeit seismisch inaktiven West Fault mit veröffentlichten Studien zur elektrischen Leitfähigkeitsstruktur der aktiven San Andreas Störung, deutet darauf hin, daß die Tiefenerstreckung und die Leitfähigkeit von Störungsleitern eine Funktion der Störungsaktivität ist. Befindet sich eine Störung in einem Stadium der Deformation, so bleibt das Bruchnetzwerk für Fluide permeabel und verhindert die Versiegelung desselben.

# Contents

<b>Introduction</b>	<b>1</b>
<b>1 The magnetotelluric sounding method</b>	<b>6</b>
1.1 The skin depth . . . . .	7
1.2 The MT impedance tensor . . . . .	7
1.3 Magnetic transfer functions (GDS) . . . . .	10
<b>2 Geological overview</b>	<b>11</b>
2.1 The Central Andes of northern Chile . . . . .	11
2.2 The Precordilleran Fault System and the West Fault Zone . . . . .	15
2.2.1 The PFS as seen with large scale magnetotelluric surveys . . . . .	17
<b>3 The study area</b>	<b>19</b>
3.1 Local geology . . . . .	19
<b>4 Structural geology</b>	<b>22</b>
4.1 Mesoscopic structural inventory . . . . .	22
4.2 Damage element characteristics . . . . .	23
4.2.1 Fault type . . . . .	23
4.2.2 Density profile of damage elements . . . . .	25
4.3 Kinematic interpretation . . . . .	27
4.3.1 Synoptic analysis - multiple deformation events . . . . .	27
4.3.2 Outcrop by outcrop analysis - paleo-strain / stress reconstruction . . . . .	29
4.3.3 Discussion of results with reference to published studies . . . . .	34
4.4 The late stage alteration process . . . . .	38
4.5 Summary . . . . .	39
<b>5 The magnetotelluric experiment</b>	<b>40</b>
5.1 The magnetotelluric profiles . . . . .	40
5.2 The data processing . . . . .	41
5.3 Geomagnetic depth sounding results . . . . .	42
5.4 Dimensionality and directionality of MT data . . . . .	46
5.5 Inversion and forward modelling of MT data . . . . .	51
5.5.1 The inversion result . . . . .	51

---

5.5.2	Model parameter and sensitivity studies: alternative models . . . . .	55
5.6	Summary . . . . .	62
<b>6</b>	<b>Correlation and discussion</b>	<b>64</b>
6.1	Correlation of structural damage and conductivity anomaly . . . . .	64
6.2	Comparison with other WFZ segments and San Andreas Fault, California . . . . .	74
6.3	Fault scaling relationships . . . . .	76
6.4	Conclusion . . . . .	80
	<b>Appendix</b>	<b>82</b>
A.1	Methods applied for paleo-strain/stress reconstruction . . . . .	82
A.2	Magnetotelluric data and model response . . . . .	85
A.3	Photo plates . . . . .	91
A.4	Map of the Gorila region . . . . .	93
	<b>Symbols and abbreviations</b>	<b>94</b>
	<b>References</b>	<b>107</b>
	<b>Acknowledgements</b>	<b>108</b>
	<b>Curriculum vitae</b>	<b>110</b>



# Introduction

Large scale strike-slip faults cut the continental crust in many regions of the world and contribute to the earthquake hazard. The most well known strike-slip faults are the San Andreas Fault in California and the North Anatolian Fault System in Turkey. The San Andreas Fault is a plate bounding transform fault, that cuts the lithosphere, while the North Anatolian Fault results from indenting continental blocks (indent-linked strike-slip fault) and is believed to be confined to the crust (Sylvester, 1988). A third type of large scale strike-slip faults is connected to oblique convergence in subduction zones and is classified as 'trench-linked strike-slip faults' (Woodcock, 1986). These faults are thought to accommodate the margin parallel component of convergence within the forearc or arc region of the overriding plate (Fitch, 1972; McCaffrey, 1996). Probably the clearest example is the Semangko Fault on Sumatra (Yu et al., 1993; McCaffrey, 1992). Due to the fact that these faults can generally be traced for several hundreds or even thousands of kilometers it is believed that they extend through the lithosphere (Sylvester, 1988).

Within the framework of the collaborative research program 267 'Deformation Processes in the Andes'<sup>1</sup>, the work onhand deals with the investigation of such a trench-linked strike-slip fault, located in the Central Andes. Two large scale margin-parallel shear zones have formed in the course of convergence of the Nazca (Farallon) and South America tectonic plates in the north Chilean Andean orogen: the Atacama Fault Zone and the Precordilleran Fault System (PFS). A segment of the latter is the focus of this study.

The PFS is located in the Andean Precordillera of north Chile and is traceable for more than 2000 km parallel to the N-S trending continental plate margin or subduction trench (Lindsay et al., 1995). Although apparently inactive, this fault system appears as a region of enhanced electrical conductivity at greater depth between 10 and > 100 km (Echternacht et al., 1997; Echternacht, 1998; Schwalenberg, 2000; Lezaeta, 2001). Scientific and economic interest in this fault system is due to the fact that many economically important copper mines align along its northern segment, the West Fault Zone (WFZ) and its master fault, the West Fault (WF), which is roughly located between 24.5°S and 20.5°S. Ossandón et al. (2001) describe this fault zone as »a major, long-lived, and very dynamic regional fault zone, which focused hydrothermal activity at least intermittently over millions of years« and which is »almost surely the major reason why (the Chuquicamata Copper-) deposit became such a huge concentration of metal and sulfur«. We chose this fault zone as a natural laboratory to investigate aspects concerning the geometry, mechanics and evolution of a mayor strike-slip fault system that cuts at least the brittle part of the crust. The following paragraphs outline some fault zone characteristics.

---

<sup>1</sup>The SFB (SonderForschungsBereich) 267 is a joint program of the Free University of Berlin, the Technical University of Berlin, the University of Potsdam and the GeoForschungsZentrum Potsdam.

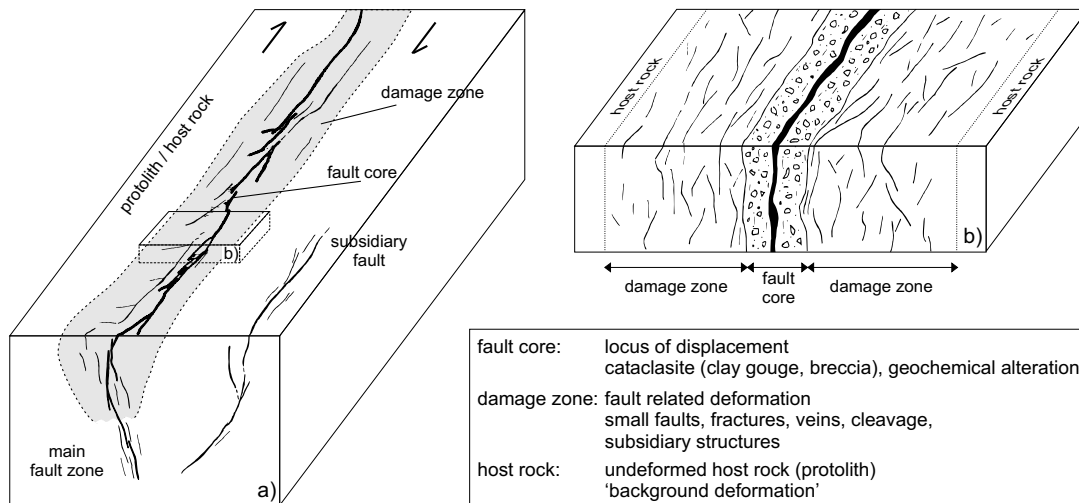


Fig. 1: Conceptual model of a fault zone with its structural units. A scale is omitted on purpose, in order to account for the supposed scale invariance of fault geometries.

Upper-crustal fault zones are structurally complex and lithologically heterogeneous zones of brittle deformation. They control subsurface fluid flow (melts, brines, meteoric waters) either by localising flow in the fault zone or by impeding cross fault fluid mobility (Caine et al., 1996). Fault zones may form vertical-flow conduits (Rice, 1992) or control groundwater flow along the fault's strike (Gudmundsson, 2000). A fault zone's behaviour as conduit or barrier is not a permanent characteristic but is a function of space and time (Evans et al., 1997). The presence of high-pressure fluids within faults, furthermore, is hold liable for often observed inherent weakness of crustal scale faults (Faulkner & Rutter, 2001; Chester et al., 1993; Hickman et al., 1995). Byerlee (1993), Blanpied et al. (1992) or Sleep & Blanpied (1992), among others, relate the time varying permeability structure of faults to the earthquake cycle. Knowledge about fluid movement through fault zones and its governing principles has implications in many different fields: the role fluids have in the earthquake cycle, geothermal energy production, leakage of buried waste disposal close to fault zones, presence of corrosive brines and, of course, the development of economical important mineral deposits (McCaig, 1989).

In the past decades, we have achieved a better understanding of the internal structure of brittle fault zones and discrete fractures from field work in many different settings (e.g. Janssen et al., 2002; Rawling et al., 2001; Schulz & Evans, 2000, 1998; Cello et al., 2000; Cello, 2000; Unsworth et al., 1997; Caine et al., 1996; Chester et al., 1993). Combined with results from laboratory fracture experiments and numerical models, we have learned, that faults grow through complex breakdown processes at the faults tip (Chester & Chester, 1998; Sibson, 1986). Throughgoing shears form by coalescence and linkage of isolated cracks or fractures, and a characteristic fault architecture remains.

Commonly, three architectural elements are discriminated for brittle fault zones in low-porosity rocks (e.g. Rawling et al., 2001; Caine et al., 1996, Fig. 1): (i) the host rock (country rock) or protolith, which is the unfaulted rock volume bounding the fault related structures; (ii) the damage zone, which comprises minor faults, fractures, fracture networks, veins, cleavages or other subsidiary structures all related to the main fault growth processes; (iii) the fault core, where most of the fault

displacement is localised. The fault core is rarely developed as a discrete slip surface, but commonly found to be composed of cataclastic rocks like breccias, clay rich gouges of variable degree of induration/consolidation or geochemically altered zones. The transition from the damage zone to the undeformed host rock is gradual. Therefore, the width of a damage zone is mostly structurally defined as the regions that bound the fault core and in which fracture density is above a certain threshold value (Cello et al., 2000; Janssen et al., 2002). A fourth structural element, which plays a significant role in describing the growth processes of a single discrete fracture is the 'process zone'. Following the definition of Vermilye & Scholz (1998) the process zone comprises those features that result directly from propagation of the fault tip. It is an element which can only be clearly distinguished from the fault core in small scale natural fault studies with relatively simple displacement history (e.g. Vermilye & Scholz, 1998) or in laboratory fracture experiments (e.g. Zang et al., 2000; Reches & Lockner, 1994). Regional scale, long-lived fault zones, on the other hand, have a complex displacement history comprising accumulation of many slip events and reactivation of preexistent shears (e.g. Kim et al., 2001; Mitra & Ismat, 2001).

Interestingly, the results of field studies and experimental fracture work imply that fault growth processes might be self-similar or scale-invariant, i.e. that they obey the same laws over a broad range of scales (see Bonnet et al., 2001 for a comprehensive review). Some important scaling laws being investigated are the cumulative fault displacement to fault length ratio, the dependency of fault width to fault length and the fault size to frequency distribution (similar to the Gutenberg-Richter (1954) distribution of earthquake magnitude to occurrence frequency). Understanding these scaling properties is helpful for evaluating seismic hazard, since the earthquake energy release is related to the dimensions of the rupture plane and the slip magnitude (Scholz & Gupta, 2000; Scholz & Cowie, 1990). It further allows to »extrapolate the commonly two-dimensional view of faults into the third dimension«, i.e. to extrapolate the fault appearance on the Earth's surface to the depth (Cowie & Scholz, 1992a). However, predictions obtained from theoretical fault growth models need to be tested against investigated properties of natural fault zones. The record of such natural fault investigations is increasing considerably in the last view years, nevertheless, large-scale fault systems remain underrepresented (Schultz & Fossen, 2002; Schlische et al., 1996).

Structural geology studies of fault zones are usually restricted to the surface signature a fault produces. Little is known about the subsurface continuation of the mapped fault. To overcome this problem we designed this project to include imaging of the subsurface electrical conductivity structure along profiles crossing the fault zone. The conductivity parameter is sensed with the magnetotelluric method (MT), which utilizes naturally occurring electromagnetic fields that induce currents into the Earth. The penetration depth of the currents into the Earth depends on the frequency content of the inducing electromagnetic fields and the electrical conductivity of the subsurface. Sensors installed on the Earth's surface record a superposition of the time varying primary and secondary fields. The ratio of electric to magnetic fields yields the information to derive resistivity<sup>1</sup> versus depth models.

The conductivity of a rock is significantly depending on the percentage, connectivity and contents of the pore volume between the minerals, while the rock matrix is usually very resistive (Haak & Hutton, 1986; Jones et al., 1992). Little amounts of an interconnected fluid phase, for example, can

---

<sup>1</sup>The electrical resistivity  $\rho$  [ $\Omega\text{m}$ ] is the reciprocal of the conductivity  $\sigma$  [ $\text{S/m}$ ]. Using the resistivity notation has the advantage of dealing with smaller numerical values.

Host rock	Resistivity range ( $\Omega\text{m}$ )	
Crystalline Rocks	$\sim 1000 - 10^6$	
Young Sediments (porous, brine saturated)	$\sim 1 - 100$	
Old Sediments (less porous)	$\sim 10 - 1000$	
Limestones	$\sim 100 - 10^7$	
Clays	$\sim 1 - 100$	
Conductive Constituent	Resistivity ( $\Omega\text{m}$ )	Min. Vol. Fraction for $100 \Omega\text{m}$
Silicate Melt ( $\sim 1500^\circ\text{C}$ )	$\sim 100$	$\sim 1$
Seawater	$\sim 0.3$	$\sim 0.003$
Brine	$\sim 0.01$	$\sim 10^{-4}$
Sulfides	$\sim 10^{-3} - 10^{-5}$	$\sim 10^{-5} - 10^{-7}$
Magnetite	$\sim 10^{-4}$	$\sim 10^{-6}$
Carbon	$\sim 10^{-4} - 10^{-5}$	$\sim 10^{-6} - 10^{-7}$

Tab. 1: Compilation of the electrical resistivity of some earth materials and conductive constituents (Haak & Hutton, 1986; Jones, 1992; Telford et al., 1990). Their minimum volume fraction needed to obtain resistivities of  $100 \Omega\text{m}$  is calculated after Archie's law (e.g. Glover et al., 2000) on the assumption of perfect interconnection of the conductive phase in the host rock material (after Duba et al., 2001). Note the log-scale range of resistivity values that can be encountered in a field experiment.

increase the conductivity of a material by several orders of magnitude. Hence, the MT method is sensitive to the structural state of a rock (matrix discontinuities / fractures, porosity / permeability, etc.) compared to the rock mass itself. This makes the method valuable in resolving the structural damage related to a brittle fault zone. To illustrate the broad range of rock resistivities, Tab. 1 gives values for some rocks as well as for conductive constituents that could enhance conductivity.

Thus, faults can alter the subsurface electric conductivity in many different ways: (i) by juxtaposing two geologic units with differing electrical conductivities via lateral or vertical displacement; (ii) by creating permeable pathways for saline fluids within fractured parts of the fault zone; (iii) by developing a clayey fault zone material (e.g. a clay gouge), which itself is conductive; (iv) or by precipitation or concentration of an electronic conductive phase (graphite, sulfides, ores) that forms an interconnected network or film (Elektb Group, 1997; Jones, 1998, gives some examples for these cases). The last three of these scenarios are the most likely to observe.

Several published results demonstrate the successful application of the method for imaging fault related structures and their geometry at depth (e.g. Unsworth et al., 1997, 1999, 2000; Mackie et al., 1997; Hoffmann-Rothe et al., 2001; Eberhart-Phillips et al., 1995). Particularly, the work presented by Martyn Unsworth and colleagues on the conductivity structure of a segment of the San Andreas Fault in California, USA, has had a major impact. In their studies, the fault clearly correlates with a zone of enhanced conductivity.

To sum up, this project is a strong interdisciplinary approach to get a comprehensive view of a segment of the West Fault Zone. The overall aim is to learn how fault zones evolve, especially within the near surface crustal segment. Particularly, the following questions are addressed:

- What is the internal architecture of the West Fault and what are its geometric parameters (width,

depth extent)? How do they compare with the common view of fault zones and the prediction from fault scaling laws?

- How well is the correlation of fault related deformation as observed on the surface with the electrical conductivity structure of the subsurface?
- Are fluids a relevant constituent to enhance conductivity or do we have to account for the effect of mineralized networks? If present, what is the origin of fluids in the fault zone?
- Does fluid mobility along structural elements of the fault (fault planes, damage zone, fault core) reflect in changes of electrical conductivity?
- Is deformation intensity and fluid activity interrelated to the magnitude of a probable conductivity anomaly?
- What can be inferred about the recent fluid activity? Is the fault in a state of healing and cementation, which could be expressed by zones of reduced conductivity?
- How does the investigated segment of the WFZ compare with other segments of the same fault zone?
- How do the findings compare with results of the very well investigated San Andreas Fault (California, USA)?

### **Structure of the thesis**

The following chapters give a brief explanation of the magnetotelluric and geomagnetic depth sounding methods, a geological overview of the northern Central Andes and its large strike-slip systems, followed by the presentation of the study area. The geological investigations and the geophysical experiment will be described independently of each other in self-contained chapters (4 and 5) that comprise discussions of the findings as far as the respective method is concerned. To avoid repetitions, the subsequent chapter (6) combines the correlation of the results of both methods with discussing their implications concerning the questions posed above.

# 1 The magnetotelluric sounding method

The theoretical background of the magnetotelluric (MT) and geomagnetic depth sounding (GDS) methods are briefly presented in this chapter. I will confine myself to describing those aspects that are essential for the understanding of the method and its usefulness and limits in regard to the scientific objective of this work. Detailed descriptions of the MT method are given in Vozoff (1991) or Kaufman & Keller (1981).

The first ideas about a geophysical prospecting method that 'passively' uses natural electromagnetic source fields go back to Tikhonov (1950) and Cagniard (1953). The method is founded on time varying electromagnetic (EM) fields that penetrate into the Earth, where they induce 'telluric' currents. The latter depend on the specific conductivity of the subsurface as well as on the frequency of the EM field. The electric  $\mathbf{E}$  and magnetic  $\mathbf{B}$  field variation of the superimposed primary (external) and secondary (internal) electromagnetic field is measured at the Earth surface. Transfer functions relate the  $\mathbf{E}$  and  $\mathbf{B}$  fields and contain the information about the electrical properties of the Earth's interior. MT uses the horizontal field components of both  $\mathbf{E}$  and  $\mathbf{B}$ , while GDS uses horizontal and vertical magnetic field components. The variations of the electric field are measured in [mV/km], those of the magnetic field in [nT].

Time varying natural electromagnetic fields that are of importance for MT and GDS mostly arise in two source regions (Vozoff, 1991). (1) In the frequency range above a few Hz, lightning discharges associated with thunderstorms emit broad band electromagnetic signals (called 'spherics'). Spherics with great energy can circle around the Earth within the insulating atmosphere for several times. Because lightning discharges occur constantly on Earth they provide a constant source of electromagnetic energy. A recording time of several hours usually ensures good quality data in this frequency range. (2) Electromagnetic fields with frequencies below 1 Hz, on the other hand, originate from time varying current systems in the Earth's magnetosphere. The interaction of the Earth's magnetic field with the plasma flow of the sun (solar wind) is a very important source for micropulsations in the energy spectrum of the magnetic field (Kaufman & Keller, 1981). Ionized gases in the ionosphere that are set in motion by tidal forces and the diurnal periodicity in the degree of ionisation, are further sources for variations of the magnetic field. The recording of a sufficient amount of oscillations for a statistical data analysis in the low frequency range can last from several days to weeks.

Most electrical power consuming devices radiate electromagnetic fields, too. In densely inhabited or industrially utilized areas such artificial, man-made signal can be responsible for noise in the data if the requirements for the application of the MT method (see below) are not met (Junge, 1996). Monochromatic signals, as the common 50 Hz signal caused by electric power lines for instance, can usually be eliminated with notch filters that are part of the recording instruments. In electromagnetic noisy areas a longer time of data registration is necessary to improve the signal to noise ratio.

## 1.1 The skin depth

The propagation of electromagnetic fields in the conductive Earth is governed by the Maxwell equations. Some approximations are made to the set of equations when applying it to the MT/GDS method. The incident electromagnetic field is assumed to be a plane wave that propagates as a function of depth only and penetrates vertically into the subsurface (Kaufman & Keller, 1981). The plane-wave prerequisite of the incident field is met for the ionospheric source region (Cagniard, 1953; Vozoff, 1991), while spherics must have their origin in sufficient distance to the measurement site. A distance of seven skin depths (see below) is usually accepted as a rule of thumb (Telford et al., 1990). Furthermore, free charges in the Earth are neglected, i.e. the Earth's EM field is assumed to be source-free. Formulating the Maxwell equations in quasi-stationary approximation (thus without consideration of displacement currents) and assuming that the time variation of the electromagnetic field is harmonic ( $\mathbf{E}, \mathbf{B} \sim e^{i\omega t}$ ), allows rearrangement into two Helmholtz equations for the electric and magnetic field, of the form

$$\nabla^2 \mathbf{F} = k^2 \mathbf{F} \quad \text{with} \quad k^2 = i\omega\mu_0\sigma. \quad (1.1)$$

$\mathbf{F}$  denotes  $\mathbf{B}$  and  $\mathbf{E}$ , respectively,  $k$  is the complex wave number,  $\mu_0$  is the magnetic permeability of free space,  $\omega$  the angular frequency and  $\sigma$  the conductivity. The equation shows that the electromagnetic fields in the Earth propagate according to the laws of diffusion. A solution of the equation is  $\mathbf{F}(\omega, z) = \mathbf{F}_0 e^{i\omega t - kz}$  with  $z \geq 0$ . The term  $e^{-kz}$  describes the decay of the fields with depth  $z$ . A skin depth  $\lambda$ , that determines the depth at which the field is attenuated to  $1/e$  of the surface value, can be calculated from the real part of  $k$ :

$$\lambda \approx 0.5\sqrt{\rho T} \quad [\text{km}] \quad \text{with} \quad T = \frac{2\pi}{\omega} \text{ [s]}, \quad \rho = \frac{1}{\sigma} \text{ [\Omega m]}. \quad (1.2)$$

The skin depth  $\lambda$  allows to estimate the penetration depth of the electromagnetic wave as a function of its period  $T$  and the specific resistivity  $\rho$  of a homogeneous subsurface. The penetration depth and consequently the sounding depth<sup>1</sup> of the MT/GDS method is thus greatest for low periods and low conductivities. Penetration depth of  $> 100$  km can be easily reached with long period measurements. In order to resolve upper crustal structures at a depth of several kilometers, as sought in this work, one has to use the higher frequency range. Investigations using frequencies  $> 1$  Hz are also referred to as audio-magnetotellurics (AMT).

## 1.2 The MT impedance tensor

The ratio of the components of the measured horizontal  $\mathbf{E}$  and  $\mathbf{B}$  fields defines an impedance tensor  $\hat{\mathbf{Z}}$ , which does not depend on the intensity of the primary field (Cagniard, 1953; Kaufman & Keller, 1981):

$$\mathbf{E}(\omega) = \hat{\mathbf{Z}}(\omega) \cdot \mathbf{B}(\omega) \quad \iff \quad \begin{bmatrix} E_x(\omega) \\ E_y(\omega) \end{bmatrix} = \begin{bmatrix} Z_{xx}(\omega) & Z_{xy}(\omega) \\ Z_{yx}(\omega) & Z_{yy}(\omega) \end{bmatrix} \begin{bmatrix} B_x(\omega) \\ B_y(\omega) \end{bmatrix}. \quad (1.3)$$

<sup>1</sup>It is more accurate to say 'sounding hemisphere' because the EM field propagates in form of a half sphere into the subsurface.

This equation is based on a cartesian coordinate system with  $x$  denoting magnetic north,  $y$  magnetic east and  $z$  being positive downwards. The complex transfer function  $\hat{\mathbf{Z}}$  has the unit [m/s]<sup>1</sup>.

The form of the impedance  $\hat{\mathbf{Z}}$  reflects the dimensionality of the subsurface conductivity structure:

- In the simple case of a **homogeneous half space** with uniform conductivity  $\sigma$ , only  $\mathbf{B}$  and  $\mathbf{E}$  fields, that are perpendicular to each other, are correlated. This means that the diagonal elements  $Z_{xx}$  and  $Z_{yy}$  of  $\hat{\mathbf{Z}}$  are zero and the off-diagonal elements  $Z_{xy}$  and  $Z_{yx}$  differ only in sign and are independent of frequency.
- In the case of a **one dimensional** layered half space the conductivity depends on depth  $z$  and thus on frequency due to the skin effect. The off-diagonal elements again differ in sign, so that  $Z_{xy} = -Z_{yx}$ .
- In the **two dimensional** case the conductivity  $\sigma$  varies with depth and one horizontal direction. The diagonal elements still remain zero but the transfer functions relating  $E_x$  to  $B_y$  and  $E_y$  to  $B_x$ , respectively, now have different values:  $Z_{xy} \neq -Z_{yx}$ .
- In the **three dimensional** case all elements of  $\hat{\mathbf{Z}}$  are non-zero. The exclusive dependency of mutually perpendicular oriented  $\mathbf{E}$  and  $\mathbf{B}$  fields does not hold anymore.

The impedance tensor  $\hat{\mathbf{Z}}$  is commonly represented as sounding curves of apparent resistivity  $\rho_a(\omega)$  and phase  $\phi(\omega)$  against a logarithmic  $x$ -axis of frequency  $f$  or period  $T(=1/f)$ . The phase  $\phi$  is the phase difference of  $\mathbf{E}$  and  $\mathbf{B}$ .

$$\rho_{a,ij}(\omega) = \frac{\mu_0}{\omega} |Z_{ij}(\omega)|^2 \quad (1.4)$$

$$\phi_{ij}(\omega) = \arctan \left( \frac{\text{Im } Z_{ij}(\omega)}{\text{Re } Z_{ij}(\omega)} \right) \quad (1.5)$$

The suffixes  $ij$  denote the respective tensor elements of the impedance tensor. For a homogeneous half space,  $\rho_a$  is equal to the absolute specific resistivity  $\rho$  of the subsurface and the phase  $\phi$  is 45°. In settings that are predominantly one or two dimensional commonly only the sounding curves of the off-diagonal elements  $Z_{xy}$  and  $Z_{yx}$  are shown. In these cases the phase  $\phi(\omega)$  varies between  $0^\circ \leq \phi(\omega) \leq 90^\circ$ <sup>2</sup>. A decrease in the resistivity values over period correlates with phases greater 45° and vice versa (Fischer et al., 1992).

Ideally, MT measurements should always be subjected to three dimensional interpretation. However, three dimensional modelling is very demanding on computing resources and present-day software does not allow to investigate conductivity structures of great complexity. The huge amount of free parameters makes it difficult to distinguish important from subordinate features. Proper 3D modelling of the data requires a data set that is measured accordingly, i.e. along several parallel and perpendicular profiles. Many MT surveys show that the measured conductivity anomaly is dominated by two dimensional structures, in which case it is attempted to approximate the fit to the data with

<sup>1</sup>More correctly, the impedance should be formulated as the ratio of  $\mathbf{E}$  and the magnetic field vector  $\mathbf{H}$ , instead of the magnetic induction vector  $\mathbf{B}$  (Hobbs, 1992).  $\hat{\mathbf{Z}}$  would then have the unit [ $\Omega$ ] as expected for an impedance value. However,  $\mathbf{B}$  is the quantity actually measured in the field.

<sup>2</sup>Strictly speaking the phase of  $Z_{yx}$  varies between  $-180^\circ \leq \phi(\omega) \leq -90^\circ$  but for better comparison of the components the phases will all be represented within the first quadrant.



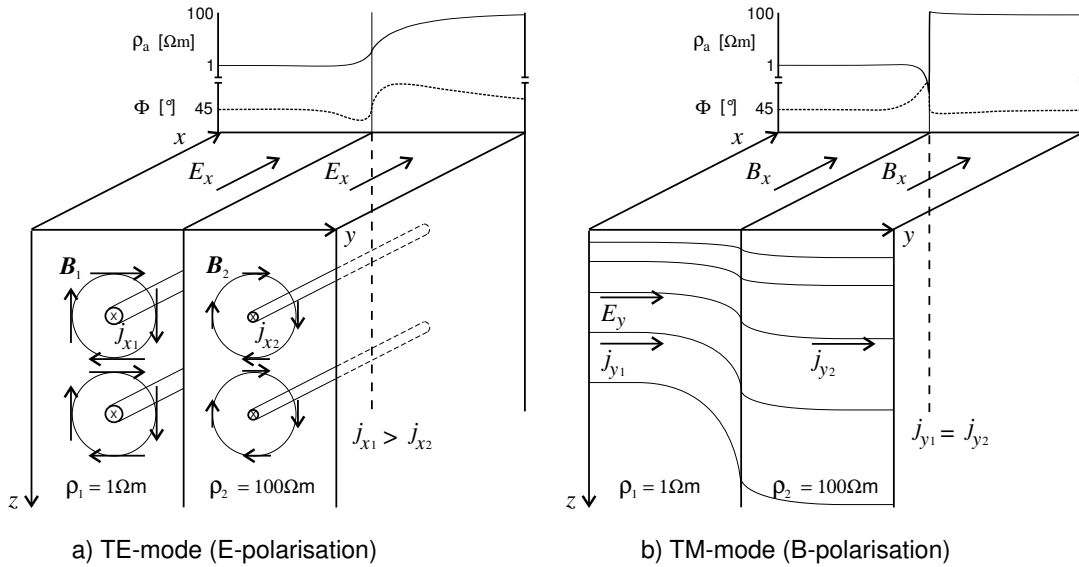


Fig. 1.1: TE- and TM-mode polarisation of  $\mathbf{E}$  and  $\mathbf{B}$  fields for a two dimensional conductivity structure. Apparent resistivity  $\rho_a$  and phase  $\phi$  sounding curves for virtual profiles along the  $y$ -axis, crossing the lateral conductivity contrast, are also shown.  $\rho_{1,2}$  are the resistivities of the half-blocks,  $\mathbf{j}$  denotes current density,  $\mathbf{E}$  and  $\mathbf{B}$  are electric and magnetic fields, respectively.

a two dimensional model (e.g. Brasse et al., 2002; Hoffmann-Rothe et al., 2001; Unsworth et al., 2000). It has to be carefully investigated that this is allowed for the recorded data or a subgroup of the data (chapter 5.4). For this work it is reasonable to assume the predominance of a 2D structure, since the examined fault represents a more or less uniform shear plane cutting through the area of investigation.

The behaviour of electric and magnetic fields in the 2D case is demonstrated in Fig. 1.1. A lateral conductivity contrast separates two materials of different resistivity  $\rho_1$  and  $\rho_2$  and strikes parallel to the  $x$ -axis, i.e.  $\sigma$  is a function of  $y$ . As stated above, the Maxwell equations in the 2D case decouple in two polarisation modes with  $\mathbf{E}$  and  $\mathbf{B}$  fields in the ground oriented parallel and perpendicular to the strike of the conductivity anomaly. In the TE-mode (tangential electric mode or E-polarisation; Fig. 1.1a) the electric current flow is oriented parallel to the strike. According to Ohm's law the current densities  $\mathbf{j}$  ( $= \sigma \mathbf{E}$ ) in the two materials are different, illustrated by the different diameter of the current lines in Fig. 1.1a. The closer a measurement site is positioned to the conductivity interface, the greater is the influence of the conductivity value on the other side on the recorded data. Because of that, impedances ( $\rho_a$  and  $\phi$ ) measured along a profile across the interface will vary as a continuous curve, as shown in the diagrams of Fig. 1.1a.

In the TM-mode (tangential magnetic or B-polarisation), the magnetic field  $\mathbf{B}$  is polarized tangential to the conductivity contrast (Fig. 1.1b). Currents resulting from the  $y$ -component of the  $\mathbf{E}$ -field at a given frequency are bound closer to the surface on the side of higher conductivity as a consequence of the skin effect. This is depicted in Fig. 1.1b with the help of electric field-lines. Since the field has to be continuous across the interface the field lines are deflected in its vicinity. This deflection of the electric field causes the behaviour of the impedance values in the vicinity of the conductivity

contrast as shown in the diagram of Fig. 1.1b. The curves do not vary smoothly across the contrast but abruptly change their values.

From all this, it follows that both polarisations image the lateral conductivity contrast although the behaviour and the actual values of  $\rho_a$  and  $\phi$  differ close to the contrast. Berdichevsky et al. (1998) reason, that deep structures are better resolved by the TE mode, while the TM mode is more sensitive to near surface structures. The resolution of deep sub-vertical fault structures might be better resolved in the TM mode. However, all available information are only taken into account if both polarisations are interpreted. If the subsurface complies with a predominantly 2D situation, both, TE and TM mode data have to be satisfyingly approximated by the 2D model.

### 1.3 Magnetic transfer functions (GDS)

The complex magnetic transfer functions  $T_x$  and  $T_y$  relate the vertical magnetic field  $B_z$ -component with the two horizontal components  $B_x, B_y$ :

$$B_z(\omega) = T_x(\omega)B_x(\omega) + T_y(\omega)B_y(\omega). \quad (1.6)$$

A vertical magnetic component does only exist in the presence of a lateral conductivity contrast. As shown in Fig. 1.1a the tangential polarised  $\mathbf{E}$ -field causes currents with different magnitude in the two media. Across the conductivity contrast the accompanying magnetic fields of two adjacent conductors do not cancel out each other and it remains a vertical ( $B_z$ ) component. In the pure 2D case and if the correct coordinate system is chosen, one magnetic transfer function is zero (e.g.  $T_x = 0$  in Fig. 1.1 a).

An illustrative way to present the information about the conductivity structure of the subsurface contained in  $T_x$  and  $T_y$  is to use induction arrows. The real and imaginary induction vectors are defined as (Schmucker, 1970):

$$\begin{aligned} \mathbf{IP}_{\text{Re}} &= \text{Re}(T_x)\underline{x} + \text{Re}(T_y)\underline{y} \\ \mathbf{IP}_{\text{Im}} &= \text{Im}(T_x)\underline{x} + \text{Im}(T_y)\underline{y}, \end{aligned} \quad (1.7)$$

with  $\underline{x}$  and  $\underline{y}$  denoting unit vectors in the respective coordinate direction. Real part induction arrows are oriented perpendicular to the conductivity contrast and point towards the direction of greatest resistivity increase (or away from the good conductor) according to the Wiese (1962) convention. The length of the arrow is a measure of the gradient of the resistivity contrast. In the two dimensional case the induction arrows of the real and imaginary parts are parallel or anti-parallel to each other. They can enclose any angle in 3D-cases.

## 2 Geological overview

The Andes are an outstanding example of an ocean-continent collision zone: Convergence of the oceanic plate system of the Pacific and the South American continental lithosphere formed a cordilleran-type mountain belt that stretches for more than 6000 km along the west coast of South America. It reaches a maximum width of about 800 km in its central part. This section gives a short characterisation of the North Chilean Central Andes and the Precordilleran Fault System (PFS), the northern segment of which, the West Fault Zone (WFZ), is the actual study object of this work.

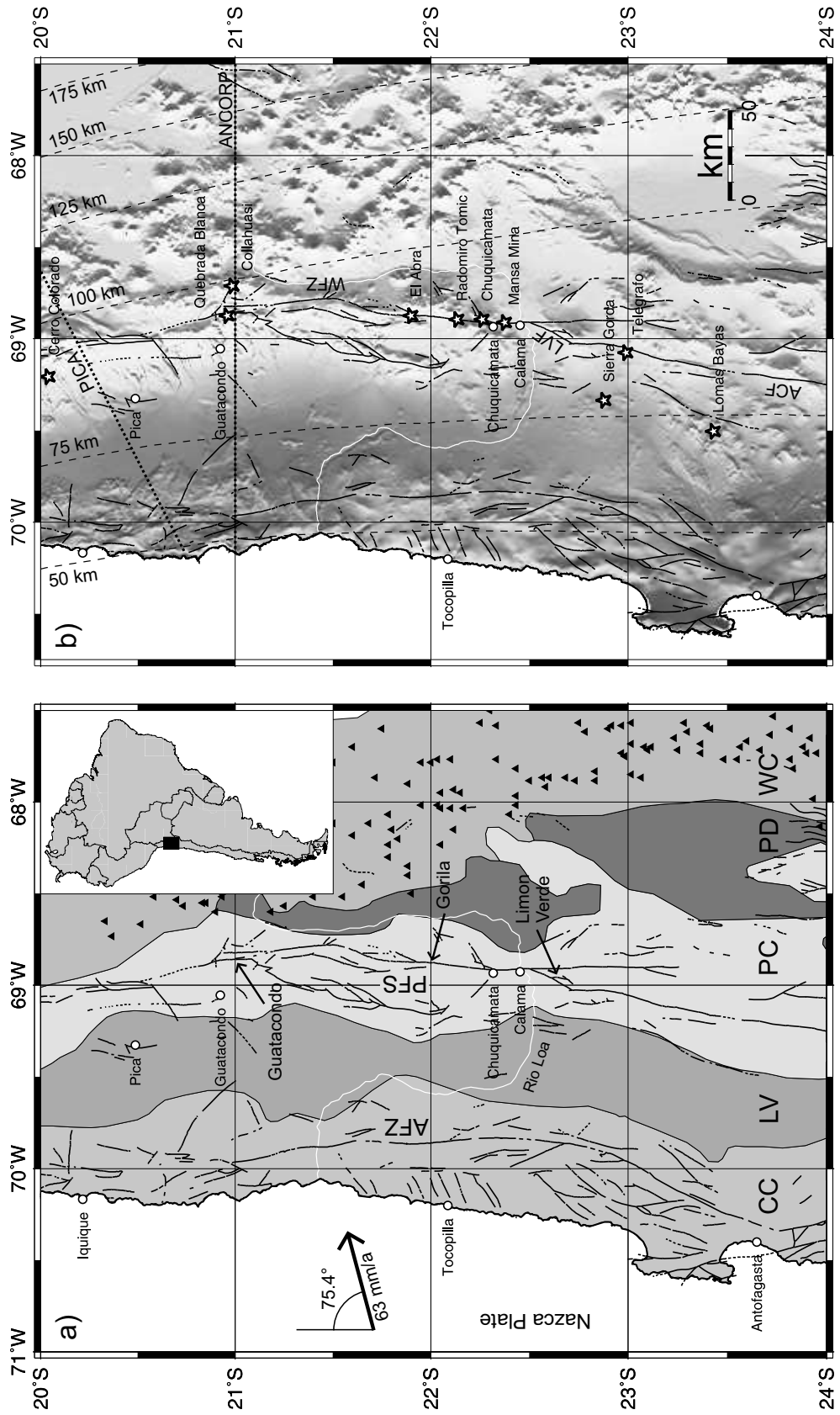
### 2.1 The Central Andes of northern Chile

The modern central Andean orogen is the result of mountain building due to eastward subduction of the oceanic Nazca (Farallon) plate beneath the South American continental margin since late Paleogene / early Neogene times (eg.: Scheuber et al., 1994; Sempere et al., 1990; Isacks, 1988; Jordan & Alonso, 1987). The orogen exhibits a characteristic tectonic subdivision into forearc, magmatic arc and backarc. Being exposed to continual compression the forearc region segmented into several differentially uplifted morphostructural units (Hartley et al., 2000) which are well recognisable on a topographic representation of the area (Fig. 2.1 a and b). These units are from west to east: the extensional Coastal Cordillera, the Longitudinal Valley (an extensional / transtensional forearc basin), the morphological high of the transpressional to compressional Precordillera and the Pre-Andine depression as a further forearc basin adjacent to the present magmatic arc.

---

Fig. 2.1: On following page. a) Morphostructural units of northern Chile (Scheuber et al., 1994; Hartley et al., 2000) and faults/lineaments according to Reutter et al. (1994). CC: Coastal Cordillera (Jurassic-early Cretaceous arc: 200-120 Ma), LV: Longitudinal Valley (Mid Cretaceous arc: 110-80 Ma), PC: Precordillera (late Cretaceous-Paleogene arc: 72-35 Ma), PD: Pre-Andine depression, WC: Western Cordillera (Miocene-present magmatic arc: <23 Ma). Triangles indicate recent volcanoes (DeSilva & Francis, 1991). Convergence vector calculated from Angermann et al. (1999). AFZ: Atacama Fault Zone, PFS: Precordilleran Fault System. The study area of this work is indicated (Gorila region). The locations of the Guatacondo and Limon Verde studies of the WFZ, published in Janssen et al. (2002), are shown, too.

b) Shaded relief map of 30-arc-seconds topography (<http://edcedac/usgs.gov/gtopo30/gtopo30.html>). Dashed lines denote depth of Wadati-Benioff zone (Cahill & Isacks, 1992). The transects of two large scale magnetotelluric studies by Brasse et al. (2002) are indicated with the dotted lines. Asterisks give the positions of major copper mines. ACF: Argomeda Calama Fault, LVF: Limon Verde Fault, WFZ: West Fault Zone.



Since the beginning of the Andean Cycle in the late Jurassic (Coira et al., 1982) continuous convergence led to the formation of four distinguishable magmatic arcs along the Chilean continental margin (Scheuber et al., 1994). The magmatic arcs correspond in position with the morpho-tectonic units (see Fig. 2.1 a) with the oldest arc located in the Coastal Cordillera. Subduction erosion processes, as indicated by the absence of a marked accretionary prism, shifted the magmatic arc consecutively towards the east into its present position in the Western Cordillera (von Huene et al., 1999). The active magmatic arc, with its volcanic peaks reaching heights of almost 7000 m, is now situated in a distance of  $\sim 200$  km from the trench and  $\sim 100$  km above the Wadati-Benioff zone (ANCORP Working Group, 1999; Cahill & Isacks, 1992). A recent space-geodetic estimation of plate convergence yields an orientation of N75°E with rate of 63 mm/a for 22°S latitude (Angermann et al., 1999).<sup>1</sup>

The parameters of plate convergence, i.e. obliqueness, rate and dip of the subducting slab, varied throughout the Andean Cycle (Somoza, 1998; Pardo-Casas & Molnar, 1987; Fig. 2.2). This gave rise to different deformation phases and associated stress regimes within the continental margin. In particular, phases of pronounced oblique convergence can lead to deformation partitioning and varying trench normal and trench parallel components of slip (Beck, 1983; Beck Jr., 1991). Scheuber et al. (1994) argue that this may have caused the formation of two large trench parallel strike-slip fault systems of the fore-arc region, namely the Atacama Fault Zone (AFZ) in the Coastal Cordillera and the Precordilleran Fault System (PFS) of the Precordillera (Fig. 2.1a).

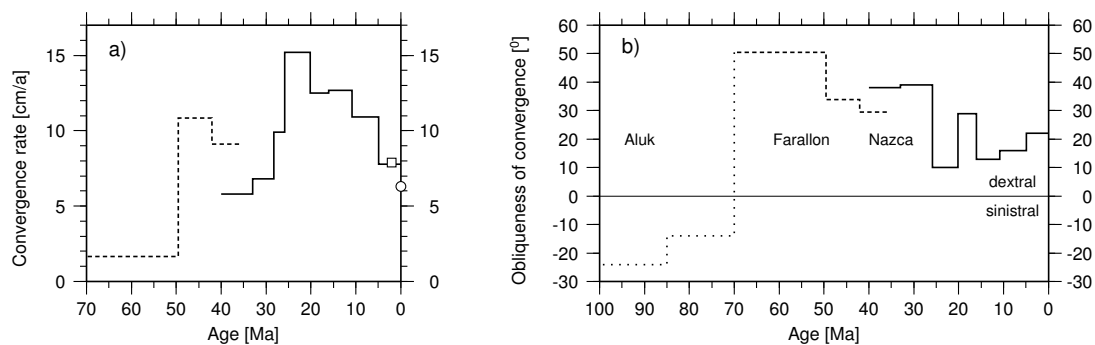


Fig. 2.2: Compilation of convergence rate (a) and obliqueness of convergence (b) for the Pacific plate system (Nazca/Farallon/Aluk) and South America. The square marker in a) gives NUVEL-1A convergence rate (DeMets et al., 1994), the circle a recent GPS determined estimate calculated from Angermann et al. (1999). Obliqueness of convergence (b) is the angle between the trench normal and the convergence vector (here: counter-clockwise positive). The solid lines refer to data from Somoza (1998), calculated for 22°S. The dashed lines are based on Scheuber et al. (1994) and Pardo-Casas & Molnar (1987) and estimate values at 25°S. The obliqueness of the Aluk-South America convergence for ages > 70 Ma (dotted) is schematically represented after Zonenshayn et al. (1984).

The more than 1000 km long AFZ developed in the early Cretaceous ( $\sim 126$  Ma) as a sinistral strike-slip fault in the course of oblique subduction of Aluk (Phoenix) oceanic plate in SE direction (Scheuber & Andriessen, 1990; Scheuber et al., 1995; Scheuber & Giese, 1999, Fig. 2.2 b). The deformation was focused in the Jurassic - early Cretaceous magmatic arc, where heating and fluid

<sup>1</sup>The global plate motion model NUVEL-1A gives a convergence rate of 79 mm/a (DeMets et al., 1994). This might indicate a significant decrease in convergence rate over the last 3 million years (Norabuena et al., 1999).

infiltration reduced crustal strength. In the late Cretaceous the sense of relative motion along the AFZ has changed to dextral according to the reorganisation of the subduction system. Throughout the Neogene, the AFZ was reactivated several times with a decreasingly less significant lateral (strike-slip) component compared to the mostly eastward directed dip-slip component. The sense of younger movements is not uniform along the AFZ as indications for dextral (e.g. Pelz, 2000) and sinistral (e.g. Delouis, 1998) displacement can be found.

The Precordilleran Fault system was initiated, similarly to the AFZ, within in the Eocene-Oligocene magmatic arc (Reutter et al., 1996). According to Scheuber et al. (1994) the increase of convergence rate in the Eocene led to enhanced coupling of the two plates. In conjunction with high convergence obliqueness this caused the formation of a transpressive regime ('Incaic Phase') in the overriding plate (Fig. 2.2 a and b). Arc normal shortening and arc-parallel dextral strike-slip along the forming PFS was the consequence. Mineral enrichment and alteration processes were structurally facilitated along the PFS and led to the formation of the economically important porphyry copper deposits of the Precordillera (Fig. 2.1 b). The complex evolution of the PFS is discussed in more detail in the following section.

It is controversial whether the variations in the parameters of plate convergence since the Oligocene are related to deformational phases and the sense of displacement along the strike-slip systems. Scheuber et al. (1994) and Buddin et al. (1993) argue in favour of a strong correlation of these processes: Episodes of high convergence rate between plates (leading to increased plate coupling) are responsible for tectonic phases of shortening (eg. the late Eocene 'Incaic' and late Miocene 'Quechua' phases) and wrench tectonics. Crustal extension occurs during interphases with reduced convergence rate. On the other hand, Hartley et al. (2000) argue, based on an analysis of a chronostratigraphic cross section across the forearc, that changes in the rate and angle of convergence are not related to the amount and style of deformation. Instead, the authors conclude that extension, strike-slip and compressional tectonics have been synchronous processes in different areas of the forearc, which is subject to continuous compression since the Oligocene.

The main phase of Andean orogen growth is commonly attributed to the significant increase in plate convergence since around 25 Ma (Fig. 2.2 a). The Andean crust is exceptionally thick, reaching up to 70 km beneath the Precordillera as deduced from seismic and gravimetric experiments (AN-CORP Working Group, 1999; Giese et al., 1999; Beck, 1996). In the backarc, a plateau formed with an average height of 4000 m. The processes leading to these conditions are not fully understood. Tectonic shortening of the crust due to the convergence of the forearc and the South American foreland is of great importance (Kley & Monaldi, 1998; Isacks, 1988) but contributions from other processes like magmatic addition (Lamb & Hoke, 1997), underplating of tectonically eroded material of the forearc (Schmitz, 1994; Pelz, 2000; Victor, 2000) or hydration of the mantle wedge (Giese et al., 1999) must be taken into account to explain the full extent of crustal thickening and plateau uplift. However, contraction is focused on the backarc regions, while the forearc was only very little shortened in Neogene time (Kley & Monaldi, 1998).

Age	Regional deformation	Dextral strike-slip	Sinistral strike-slip	Plutonism Mineralisation	Deformation phase <sup>13)</sup>
Quat					
Plio					
4	E-W shortening? <sup>1)</sup>	minor movements, ~ 1 m thrust displacement <sup>1,2)</sup>			Diaguita
6					
8	Precordilleran Uplift <sup>2,11)</sup>	~0.5 ± 0.5 km dextral displacement, normal (> 100 m) and reverse faulting <sup>1,2)</sup>			
10	E-W extension? <sup>1)</sup>				Quechua
12					
Miocene					
14					
16					
18					
20	E-W shortening <sup>2)</sup>		Upper limit Huasco Ignimbrite 16.6 Ma <sup>2)</sup> , possibly < 14 Ma <sup>12)</sup> .	Supergene <sup>9,10)</sup> Mineralisation	
22			35-37 km sinistral displacement since 37 Ma. <sup>1,2)</sup>		
24	29-5 Ma <sup>14)</sup>				
26			500-700 m of dip-slip movement on West Fault: down on west <sup>2)</sup> , up on west <sup>3)</sup> .		Pehuenche
Oligocene					
28					
30	E-W extension (sinistral trans-tensive)? <sup>5)</sup>				
32			← lower limit for sinistral slip at Cc and RT <sup>1)</sup>	Hypogene Mineralisation <sup>9,10)</sup>	
34		local evidence for dextral shear (NNE strike) but no throughgoing fault <sup>1)</sup> . Sample displacements: ~ 2 km <sup>4)</sup> , ~ 5 km <sup>5)</sup>			
36			← lower limit for sinistral slip at El Abra <sup>1)</sup>	Shallow silicic plutons <sup>1,9)</sup>	
38					Incaic
Eocene					
40	E-W shortening <sup>4)</sup>		South of 22.5°S (42-36Ma): sinistral transposition on some segments of PFS <sup>4,6,7,8)</sup>	Shallow Middle Eocene plutons <sup>1)</sup>	
42					
44					
46					
48					
50					
52					

Tab. 2.1: Compilation of displacement history of the West Fault Zone (WFZ) in the Precordillera. The last column gives discrete compressional deformation phases identified for the Central Andean arc/backarc. Cu-mines: RT - Radomiro Tomic, Cc - Chuquicamata. Sources: <sup>1)</sup> Dilles et al. (1997), <sup>2)</sup> Tomlinson & Blanco (1997b), <sup>3)</sup> McInnes et al. (1999), <sup>4)</sup> Tomlinson & Blanco (1997a), <sup>5)</sup> Reutter et al. (1996), <sup>6)</sup> Yáñez et al. (1994), <sup>7)</sup> Mpodozis et al. (1993), <sup>8)</sup> Mpodozis & Tomlinson (1998), <sup>9)</sup> Reynolds et al. (1998), <sup>10)</sup> Sillitoe & McKee (1996), <sup>11)</sup> Isacks (1988), <sup>12)</sup> Ossandón et al. (2001), <sup>13)</sup> Hartley et al. (2000), <sup>14)</sup> Victor (2000).

## 2.2 The Precordilleran Fault System and the West Fault Zone

The Precordilleran Fault System (PFS; likewise referred to as Domeyko Fault System) has a length of more than 2000 km (Lindsay et al., 1995). It is a broad shear system that is build up of many, individual branches, which can be recognized for hundreds of kilometers in the field, on aerial photographs or on satellite images (see Fig. 2.1 b). The northern part of the PFS between 23° S and 20° S will be referred to as West Fault Zone (WFZ), adopting the terminology of Tomlinson & Blanco (1997a). Its main branch (master fault) is the West Fault (WF; also: West Fissure/Falla Oeste). It is very well exposed in the Chuquicamata open pit copper mine and can be traced along 170 km almost continuously from Calama to Quebrada Blanca (Dilles et al., 1997; Fig. 2.1). Tab. 2.1 presents a compilation of published work about the fault systems history, which will be chronologically described in the following.

The Precordillera is composed of early Paleozoic rocks overlain by Triassic to Eocene strata of sedimentary and volcanic rocks (Reutter et al., 1996). Volcanism associated with the late Cretaceous-Paleogene magmatic arc ceased within the Incaic deformational phase around 38 Ma ago. Orogen normal shortening segmented the Precordillera into roughly N-S oriented anticlinal structures (base-

ment ridges), accompanied by reverse faulting and folding of the cover rocks (Reutter et al., 1996; Hartley et al., 2000). Reutter et al. (1991, 1996) ascribe the onset of dextral strike-slip faulting to this episode of transpressive tectonic setting. A through-going main fault was most certainly not developed in late Eocene/early Oligocene time (Tomlinson & Blanco, 1997a; Dilles et al., 1997) but dextral displacements on individual branches ranging between < 2 km and 5 km can be derived from aerial photography analysis (Reutter et al., 1996), en echelon fault arrays, vertical folding (Reutter et al., 1991) and stratigraphic discontinuities (Tomlinson & Blanco, 1997a).

Several studies demonstrated sinistral movements along the early PFS south of 22.5° S (Tomlinson & Blanco, 1997a; Yáñez et al., 1994; Mpodozis et al., 1993). This contradicts with the expected displacement direction in a setting of dextrally convergent plate margins. Tomlinson & Blanco (1997a) attribute contemporaneous dextral and sinistral movements on N-S directed faults to dextral transpressional forces working against a rigid buttress caused by the oroclinal Arica bend (cf. Fig. 2.3) and thickened crust. This hinders northward translation of the forearc sliver south of 22°S. The authors therefore suggest that sinistral transpression is the result of basal shear driven by asthenospheric corner flow with a NW-ward directed return flow at the base of the lithosphere. The north component of the corner flow results from the convergence obliquity.

The emplacement of shallow silicic plutons, to which the porphyry copper deposits are genetically related, took place in late Eocene/early Oligocene time. Several of these plutons are N-S elongated and aligned along the present trace of the West Fault (Tomlinson & Blanco, 1997a), especially in the Chuquicamata-El Abra region. This suggests that the fault controlled at least locally the emplacement of intrusives as demonstrated by Ossandón et al. (2001) for the Chuquicamata porphyry complex.

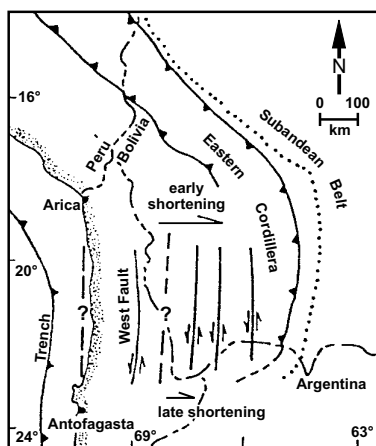


Fig. 2.3: Structural model of the central Andes for the late Oligocene to early Miocene sinistral strike-slip episode on the West Fault (slightly mod. from Tomlinson & Blanco, 1997b). A N-S shortening gradient leads to clockwise rotation accommodated on crustal blocks that are separated by sinistral strike-slip faults. The known length of the faults in southern Bolivia (solid lines) are less than depicted in the figure.

The major movements along the WFZ in Oligocene to early Miocene time have been sinistral with a displacement between 35 to 37 km. These values result from the reconstruction of matching geologic units east and west of the fault (see Tomlinson & Blanco, 1997b; Dilles et al., 1997). In this time span, rapid ascent and exhumation of the plutons and the formation of sedimentary basins hint to arc-normal extension, probably caused by the collapse of the previously thickened crust (Reutter et al., 1996). Several authors explain the sinistral strike-slip movements with a model of 'domino-style' rotation of large, N-S elongated crustal blocks as a consequence to differential shortening of the central Andes (Fig. 2.3; Tomlinson & Blanco, 1997b; Somoza, 1998; Mpodozis & Tomlinson, 1998). An important phase of shortening in the Eastern Cordillera of the Bolivian bend area started



~27 Ma (Sempere et al., 1990), about 10 Ma earlier than at 23° S latitude, where the onset of shortening is dated between 20 to 16 Ma. The resulting shortening gradient produced an E-W directed dextral shear couple with N-S trending sinistral faults accomodating slip between crustal blocks of the clockwise rotating bend area (Fig. 2.3). The beginning of shortening at the southern end of the bend area correlates with the upper limit of sinistral movement on the West Fissure (Tab. 2.1). There is no unequivocal correlation to either reduced plate convergence velocity or obliquity for this period of sinistral shear along the WFZ (cf. Fig. 2.2).

Hypogene enrichment processes (i.e. mineralisation due to ascending hydrothermal solutions), which led to the formation of porphyry copper deposits, succeeded the plutonic intrusions (Reynolds et al., 1998; Sillitoe & McKee, 1996) and were largely controlled by the PFS/WFZ. The fracture permeability of the WFZ also imposed a structural control on the mineralisation and alteration of the deposits in the important supergene stage (oxidation and enrichment due to descending ground water after exhumation of the deposit; Lindsay et al., 1996, 1995). Supergene alteration took place in the early to middle Miocene until ~14 Ma (Sillitoe & McKee, 1996), when accelerated Andean uplift caused desertification in northern Chile.

The vertical component of movement along the WF seems to be subordinate to the strike-slip component (see Tab. 2.1). Tomlinson & Blanco (1997b) suggest, based on structural indications, about 500 m of down on the west dip-slip between the Chuquicamata and El Abra copper mines and 600+ m between Chuquicamata and Limon Verde with the same sense. This contradicts findings from the comparison of isotopic markers in the Chuquicamata mine, which imply a maximum of 700 m down on the east dip-slip movement (McInnes et al., 1999). Only minor vertical movements are reported for the late Miocene dextral strike-slip episode of the WF (Dilles et al., 1997; Tomlinson & Blanco, 1997b).

### 2.2.1 The PFS as seen with large scale magnetotelluric surveys

Two large scale magnetotelluric profiles run across the north Chilean Andes from the coast into the Western Cordillera: The PICA<sup>1</sup> profile crosses the PFS at a latitude of 20.5° S, while the ANCORP<sup>2</sup> profile is located along 21° S (Fig. 2.4, cf. Fig. 2.1b for location of profiles). Inversion results of both profiles image a highly conductive region beneath the surface expression of the PFS at a depth of approximately 15 km (Brasse et al., 2002). An anomaly related to the West Fault Zone in the Precordillera was already proposed for the PICA profile on the basis of forward modelling results (Echternacht et al., 1997; Echternacht, 1998). Although the conductive structure imaged along these profiles is a robust feature, its position in depth is insecure. Echternacht et al. (1997) model the conductive zone almost from the surface to a depth of > 120 km with a region of reduced conductivity between 35 and 100 km. Interpretation of magnetic transfer function data of the ANCORP profile, shifts the anomaly closer to the surface in a depth range of 10 to 5 km (Soyer & Brasse, 2001; Soyer, 2002).

In order to explain the strong electric current channeling effects that partly distorted the MT and GDS data of both profiles, Lezaeta (2001) derived a three dimensional model. A main structure of

---

<sup>1</sup>Named after the village Pica in the Atacama desert.

<sup>2</sup>Andean Continental Research Program.

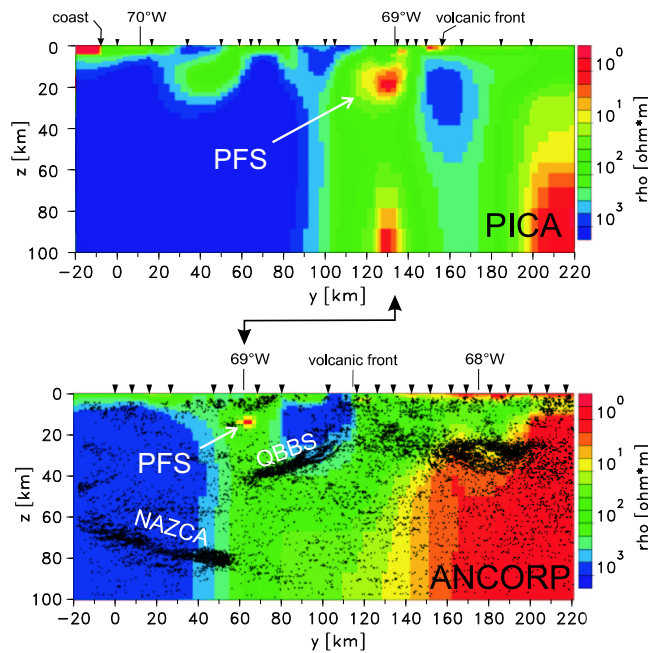


Fig. 2.4: Inversion models of two magnetotelluric profiles crossing the Andes from the coast to the Western Cordillera (modified from Brasse et al., 2002). The PICA profile is located at about  $20.5^{\circ}$  S, the ANCORP profile trends along  $21^{\circ}$  S (cf. Fig. 2.1b). Both models image a highly conductive region (red) at a depth of about 15 km beneath the approximate position of the PFS/WFZ. Reflection seismic results are included as line drawings (ANCORP Working Group, 1999). NAZCA denotes the reflector of the subducting slab, QBBS (Quebrada Blanca Bright Spot) marks a highly reflective mid-crustal structure.

this model are approximately N-S striking, highly conductive ( $< 5 \Omega\text{m}$ ), vertical dike-like structures that extend from 2 km to a depth of  $\sim 10$  km in position of the PFS. The upper crustal conductive zones beneath the Precordillera are generally attributed to saline fluids circulating in the PFS/WFZ fault-fracture system at relatively low temperatures below  $300^{\circ}\text{C}$ . According to thermal modelling by Springer (1999) the  $300^{\circ}\text{C}$  isotherm is located in a depth between 20-30 km beneath the Precordillera, which might imply a relatively deep brittle-ductile transition.

Lezaeta's (2001) 3D model requires a further conductive block at a depth between 10 and 35 km, that's conductivity decreases from north ( $20^{\circ}\text{S}$ :  $\sim < 5 \Omega\text{m}$ ) to south ( $21^{\circ}\text{S}$ :  $15\text{-}10 \Omega\text{m}$ ). Fluids liberated in mid-crustal metamorphic reactions and accumulating in the fractures of the PFS are suggested to cause the enhanced conductivity. Dehydration reactions in the subducted oceanic plate (at a depth of 70-80 km) may be a further source of conductive fluids, provided a pathway exists to feed the fault system and fluids do not induce partial melting. The N-S decrease of conductivity is assumed to be related to the different times of volcanic activity in the north ( $> 25$  Ma) compared to the south ( $< 10$  Ma). This may have led to higher production of fluids in the north or alternatively to more intensely fractured crust, due to a cooler and more brittle regime (Lezaeta, 2001).

## 3 The study area

A suitable location along the West Fault for a joint investigation of fault-related surface deformation and electrical conductivity structure of the subsurface has to satisfy certain requirements:

1. Outcrops with more or less continuous exposure of rock surfaces for several 100 meters perpendicular to the fault strike are needed to map variations of deformation style versus distance from the fault.
2. A flat morphology is sought to avoid topographic effects that might influence the magnetotelluric measurements.
3. The area should be remote from sources of artificial electromagnetic signals which do not carry information of the subsurface.

The morphology and geology of the chosen study area is shown in Fig. 3.1 (an enlarged map is enclosed in Appx. A.4). Situated north of Chuquicamata, in an unpopulated area between the copper districts of Radomiro Tomic ( $22^{\circ}8' S$ ) and El Abra ( $21^{\circ}54' S$ ), the region represents a west-ward inclined plain of Quaternary alluvial deposits at an average altitude of 3600 m above sea level. The underlying rock sequence crops out in the hills to the south (Cerros Guachos) and east (Cerros de Paqui) and in E-W trending drainage valleys, which are less than 30 m deep. Topography, thus, does not constitute a problem for the MT measurements. The valleys enable detailed investigation of fault-related deformation in an area of  $2.5 \times 2$  km (outlined in Fig. 3.1; Appx. A.4). The study area will subsequently be called 'Gorila region' in reference to the Cerro Gorila (Gorila hill) as the regions highest rise. A service road to the El Abra mine facilitates access to the area.

### 3.1 Local geology

The Precordillera in the area under investigation is composed of a Paleozoic basement consisting of early Paleozoic crystalline / metamorphic rocks and upper Carboniferous to lower Triassic volcanics (Collahuasi Formation), as shown on Fig. 3.1 (cf. Appx. A.4). The basement is overlain by a thin sequence of Triassic / Jurassic mainly marine sediments (Quehuira Fm.), Cretaceous andesitic volcanics (Empexa Fm.) and a thick continental succession of conglomerates and sandstones (Tolar Fm.). The middle Eocene saw eruptions of intermediate volcanic rocks including lavas, lahars and tuffs (Icanche Fm.). Plutons intruded into shallow crustal levels in middle to late Eocene times (46-37 Ma; Dilles et al., 1997; Reutter et al., 1996). In the Gorila region, the WF separates a quartziferous monzodiorite of the Eocene from Triassic andesites and dacites of the Collahuasi Formation. Rocks adjacent to the fault show intense alteration classified to the quartz-sericite suite of nearby porphyry copper de-

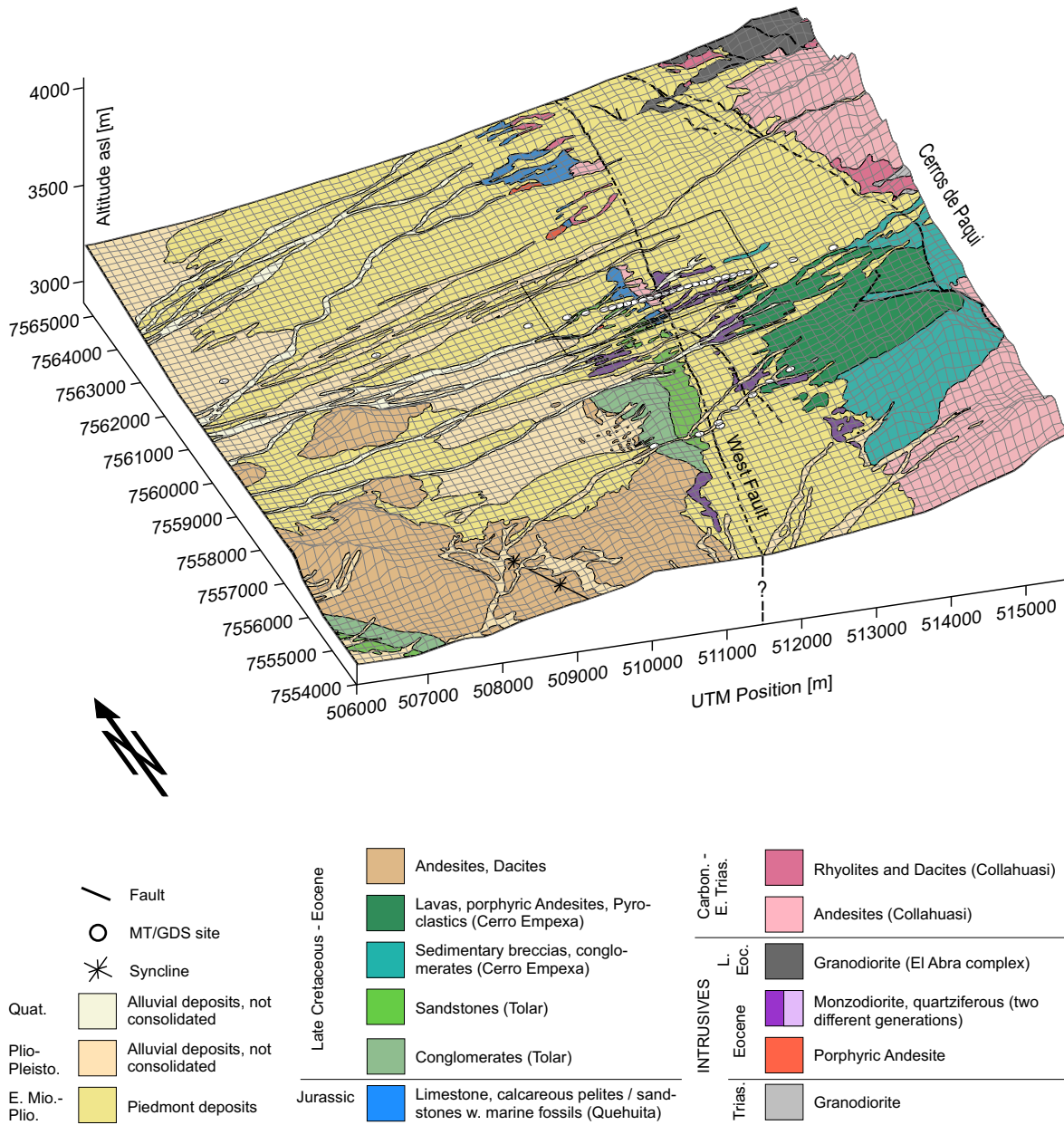


Fig. 3.1: Geology and morphology of the study area (Vertical exaggeration: 4). The geology is simplified from Maksaev et al. (1999). White dots indicate magnetotelluric sites, the rectangle outlines the region of the structural geology investigations, subsequently called 'Gorila region'. An enlarged map of the Gorila region as well as an overview map is enclosed in Appx. A.4.

posits (but they do not necessarily exhibit the associated mineralisation; A. Tomlinson, 2001, written com.). The alteration is ascribed to the hypogene and/or supergene mineralisation processes reported for the adjacent copper deposits (Ossandón et al., 2001). The monzodiorites on the western side of the fault differ in composition from those on the eastern side and are attributed to different plutonic events (Pardo, 1995; Makshev et al., 1999). The Mesozoic to late Eocene sedimentary succession to the west of the fault trace is steeply inclined; the bedding planes of the Jurassic marine sequence dip towards WSW. Structurally, the rocks are part of the eastern limb of a syncline with a northwest-ward trending axis (see Fig. 3.1). This syncline is flanking the great anticline of the Sierra de Lorenzo in the SW. On approach to the West Fault, this NW trending anticline bends into a N-S direction, which is interpreted by Reutter et al. (1996) in the context of the early dextral drag along the WFZ.

Laminated terraces of calcareous sinter deposits (travertine) of 10-20 m thickness crop out just north of the shown map. That might imply hydrothermal spring activity on fracture and fault zones in late Miocene to Pliocene time (Pardo, 1995; Makshev et al., 1999). Hot springs are not existent in the surroundings today, but a cold spring is located almost in the center of the Gorila region and directly on the trace of the WF (see Appx. A.4).

The youngest deposits are three distinguishable generations of mostly unconsolidated, polymict, alluvial sediments. Middle Miocene to Pliocene proximal piedmont deposits that are partly cemented by salts (gypsum) are dominating. Intercalated ash layers have been dated to 8-3 Ma (Makshev et al., 1999). No unequivocal indication of fault displacement of the gravels have been found in the investigated region, except for those in the El Abra region described by Tomlinson & Blanco, 1997b and Dilles et al., 1997.

### **Structural geology and magnetotelluric measurements**

The Gorila region, marked in Fig. 3.1 and shown in detail in Appx. A.4, was studied for fault related deformation structures. The investigation and its implications are described in the following chapter. Two magnetotelluric (and GDS) profiles have been measured as shown in Fig. 3.1. The Main profile trends perpendicular to the fault within the Gorila region, the second (South) profile lies several kilometers further to the south. Chapter 5 deals with the magnetotelluric experiment and its implications.

## 4 Structural geology

This chapter comprises the characterisation of fault related damage in the Gorila region as it was observed on mesoscopic, i.e. outcrop scale. The underlying kinematics/dynamics of the investigated structures are analysed, both as composite data set for the whole study area and outcrop by outcrop. The results of geochemical analysis of rock samples are briefly summarized as far as they are relevant for this work. A map is included in appendix A.4 which records outcrop locations, rock (and water) sampling sites, the locations of MT stations and results of the structural investigation among other details.

### 4.1 Mesoscopic structural inventory

Outcrops in the study area are concentrated in little canyons that are cut into the gravels by drainage from the Cerros de Paqui mountains to the east (cf. Fig. 3.1). Some of the E-W trending drainage valleys close to the WF trace exhibit bending into the strike direction of the fault (locations are marked with little arrows on the map in Appx. A.4). Recent displacement of the WF was neither proofed in the field nor is mentioned in the literature, so these drainage orientations are believed to result from erosional exploit of zones of less cohesive material related to the fault.

Outcrop faces of the sporadically exposed bed rock sequence are rough and differently oriented. This provides good coverage of the variety of orientation of damage elements but makes a quantitative investigation of their density distribution difficult. Furthermore, projection of outcrop data from the whole Gorila region is necessary to fill gaps where no data could be obtained, which results in a form of spatial averaging. The most continuous exposures are immediately to the west of the WF trace. The following describes the fault related damage elements, that were mapped in the Gorila region.

#### **Slip surfaces**

The greatest part of the data set are orientation data of fault related rock surfaces (Photos 1 and 2; all photographs in Appx. A.3). Mapping of planes on the outcrop wall faces was limited to an approximately two meter vertical range to allow a qualitative comparison of the amount of damage elements with position to the surface fault trace. Planes considered have an exposed surface of at least din A5 size (the size of the field book) except for surfaces having a very clear striation on it. Slicken lines were identified on most of the surfaces indicating that slip occurred on them (Photo 1). However, most surfaces were barren of mineral coatings, which would have simplified the identification of slip sense. In the following, the information on the orientation of the slip surface and the striation plus the sense of slip is collectively called a 'fault slip datum' (Marrett & Allmendinger, 1990). Rock surfaces showing no indication of slip on them are addressed as extensional fractures. Overall, mineral filled

veins are not abundant in the Gorila region. For the kinematic interpretation, the larger exposures have been subdivided into approximately 5-10 m wide segments (as exposures permitted).

### **Minor faults**

Minor (subsidiary) faults cut the entire face of an exposure and mostly exhibit subvertical dip (Photos 3, 4). Some of these faults formed up to approximately 1 cm wide white gouges, implying significant slip localisation. The gouge material is composed of quartz and feldspar as main constituents (x-ray diffraction analysis by G. Nover, Bonn, pers. comm). Two gouges are dominated by calcite and laumontite (a zeolithic material), respectively. The latter may be indicative for low temperature and pressure fault-fluid conditions (Parry, 1998). Erosion processes often widen minor faults to little gullies in which sense of slip indicators are not preserved (Photo 4).

### **Fault core and alteration zone**

A fault core of the type visible in the copper pit mine of Chuquicamata, with a black argillitic fault gouge up to 2.5 m thick (Reutter et al., 1996), is not exposed (or preserved) in the Gorila region<sup>1</sup>. Such a fault core might be superposed or destroyed by the processes forming the colored alteration zone to the east of the WF trace (see map in appendix A.4; Photos 5, 6). The alteration zone is visually discernible for ~400 m with granular and unconsolidated material, at least at the surface (Photo 8). The rock material progressively consolidates towards the eastern edge of the alteration zone. In contrast to that, the western margin of the alteration zone is marked by an abrupt change in cohesiveness of the rocks (Photo 5). This is very likely influenced by the lithological transition from volcanic (andesites) to plutonic rocks (monzodiorites). Some less altered blocks of rock within the alteration zone show brittle deformation with brecciated to cataclastic fabric. Within the cataclasite, mimicked 'ductile' features such as boudinages bounded by SC-like shears can be observed and hint towards cataclastic flow<sup>2</sup>. Mylonitic features have been described by Reutter et al. (1996) for fault rocks of the Chuquicamata mine, that generally are of 'low-T cataclastic nature' (Tomlinson & Blanco, 1997b). This may suggest some fault activity in the semi-brittle regime.

The alteration zone material exhibits subvertical bands of red, yellow or brownish color (photos 6, 7). Some of these are narrow (~10-20 cm), consolidated but irregularly bounded ribs or sheets that parallel the WF trace for several meters. Such 'ribs' show strong enrichment in iron oxides (hematite; G. Nover, Bonn, pers. comm). Enrichment processes along faults or fault/fracture systems during active stages of faulting and mineralization are hold liable for the formation of this banding.

## **4.2 Damage element characteristics**

### **4.2.1 Fault type**

Ideal strike slip faulting results in fault planes dipping vertically and their associated slicken-lines trending horizontally. The WF segment in the Gorila region predominantly exhibits this characteristic, as summarized in Fig. 4.1, which underlines the subordinate involvement of vertical displacement on the WF system (see sect. 2.2). The poles (normals) to slip surfaces are plotted in a lower hemi-

<sup>1</sup>The width of the fault gouge in the Chuquicamata mine changes drastically over very short distance and can reach a width of 5 m (Ossandón et al., 2001) and even up to 8 m (D. Lindsay, CODELCO, pers. comm.).

<sup>2</sup>'Cataclastic flow' in the sense of brittle-frictional deformation of a granular aggregate (Scholz, 1990).

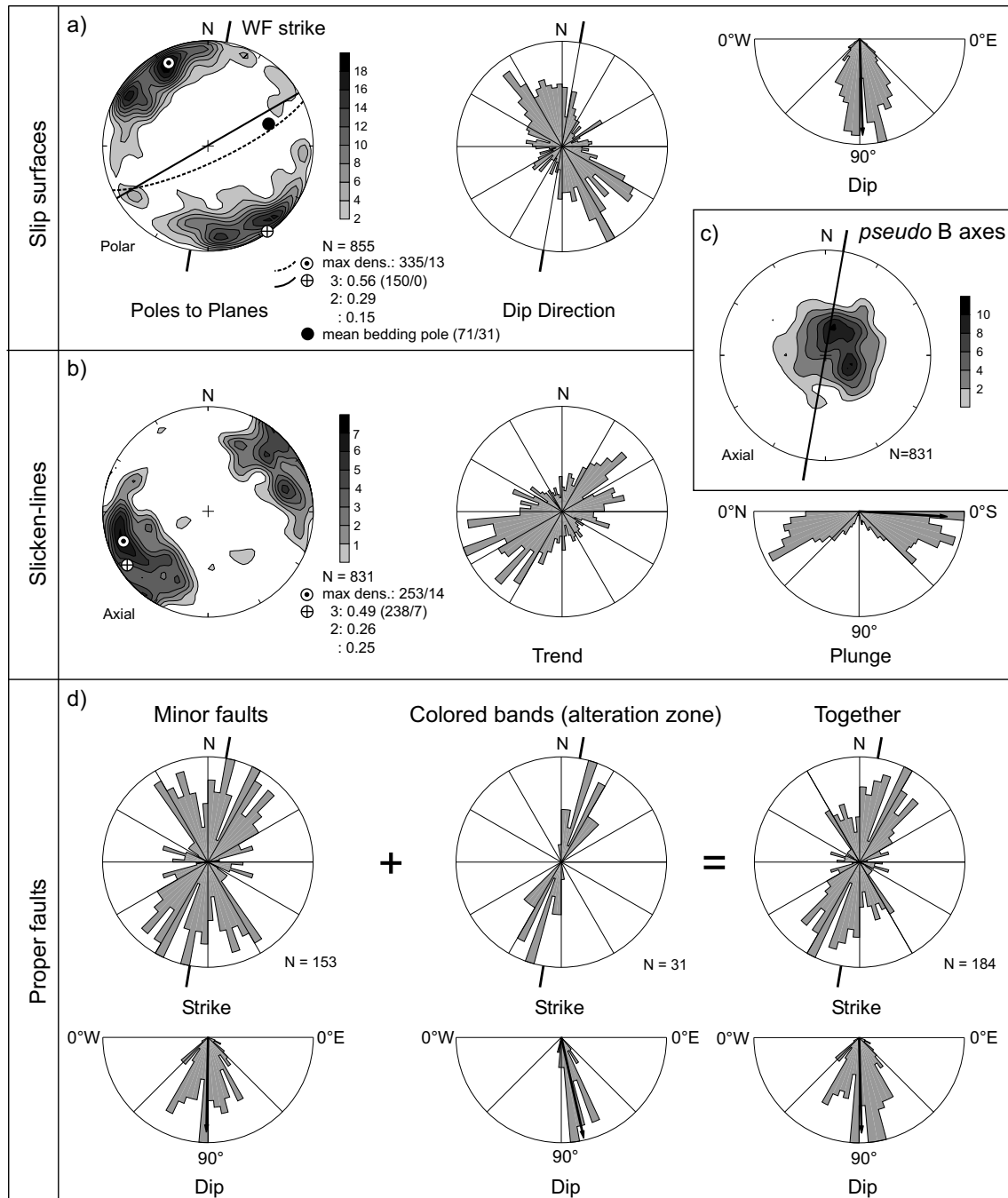


Fig. 4.1: Overview of deformation characteristics in the Gorila region. Contoured plots are equal area, lower hemisphere projections. Density contours are based on smoothed 1%-area counting on a sphere; the contour intervals are in multiples of standard deviation ( $\sigma$ ) relative to the uniform population. Points of maximum density and the eigenvalue distribution of the data (clustering characteristics,  $\lambda_3$  denotes the directional maximum) are specified. Arrows in half-circular histograms (showing dip or plunge) denote orientation means with arrow length indicating mean resultant length (radius=1). a) Orientation of slip surfaces: poles (normals) to planes (mean values included as great circles), dip direction histogram and W-E component of dip. The mean pole to bedding planes from the sedimentary succession is included; note that bedding planes are sub-parallel, i.e. poles define a clear unimodal cluster. b) Orientation of associated slicken-lines. c) Orientation of *pseudo-B* axes, i.e. lines that are orthogonal to the slip direction and lie within the shear plane. The preferred verticality indicates dominance of strike-slip kinematics. d) Orientation of minor faults and colored bands (alteration zone). See text for details.



sphere, equal area projection<sup>1</sup> (Fig. 4.1a) and show a concentration close to the circumference, thus indicating steeply dipping planes. The planes are not collectively dipping towards one direction but exhibit almost even distribution if, for example, the west- and east-components of dip are considered (Fig. 4.1a, right). Bedding plane normals mapped in the tilted Jurassic formation, form a very distinct cluster (black dot gives mean pole, Fig. 4.1a) and have apparently not functioned as preferential orientation for the formation of slip surfaces. Most of the subvertical slip surfaces are striated, with the majority of slicken-lines plunging sub-horizontally (Fig. 4.1b), as expected for strike-slip faulting. The prevalence of strike-slip displacement is emphasised by the preferential vertical orientation of *pseudo*-B-axes (Fig. 4.1c). *Pseudo*-B-axes are normals to the slicken-lines that lie within the shear plane and give an estimate of the orientation of the intermediate axes of a synoptic kinematic tensor. Their location approximately within the principal fault plane suggests further that the multitude of slip surfaces is related to slip on the WF system (Chester & Logan, 1987).

The above described fault characteristics are as well evident for the larger scale deformation elements: Figure 4.1d shows the orientation of minor faults and colored bands, the latter of which are interpreted as 'lithified' minor faults or fracture systems within the alteration zone, as reasoned in section 4.1. Most faults dip steeply and strike within an angular range of 90°, which is bisected by the orientation of the West Fault (master fault or principle fault). The colored bands are oriented very similar to the WF and their mean dip is about 75° almost exclusively towards the east. As minor faults and enrichment sheets are believed to belong to the same deformational regime, they are shown together in Fig. 4.1d. In view of the totality of data, the investigated WF segment is best described as an oblique slip fault with a predominating strike-slip component.

#### 4.2.2 Density profile of damage elements

A means to define the width of a fault zone and to differentiate between the damage zone and the fault core proper is to regard the distribution of damage elements (Caine et al., 1996). According to Chester & Logan (1986) the fault zone is marked by an increased deformation intensity compared to the surrounding host rock. Figure 4.2a shows a histogram of damage element frequency with 50 m classes for the Gorila region. The relatively large class-width is necessary to average across areas without outcrops. The data are projected onto a scan-line perpendicular to the West Fault trace (and thus parallel to the main MT-profile), as shown in Fig. 4.2b. Following the profile in the diagram from west to east, an increase of damage elements with approach to the WF trace is evident and the maximum damage element density is reached within 100 m of the fault trace. After crossing the WF trace, almost no damage elements can be identified within the alteration zone due to the intense material comminution. Only few patches, where larger blocks are less affected by alteration, contribute to the data. East of the alteration zone, the amount of damage elements increases again. Their frequency distribution between 500-800 m east of the fault trace in Fig. 4.2a may on the one hand belong to a decrease of damage element density belonging to the West Fault proper (schematically outlined with the dashed curve). In this case, deformation either culminated in the central part and led to exhaustive comminution of rocks or brittle structures are simply destroyed by later stage alteration processes.

<sup>1</sup>The stereographic equal area *Schmidt*-projection in a lower hemisphere representation is used for all stereonet figures in this work.

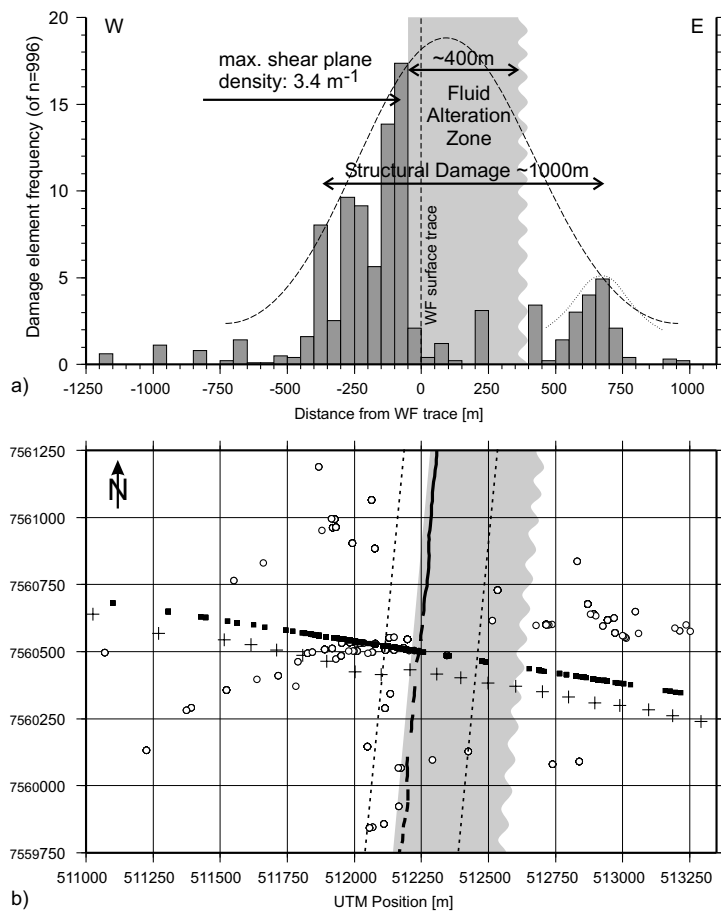


Fig. 4.2: Qualitative damage element density profile (a) of all slip surfaces and minor faults projected on a scanline perpendicular to the West Fault and parallel to the MT Main profile (b). The map gives the distribution of outcrop data (open circles) and their projection on the scanline (black squares). Crosses denote MT sites, the dashed lines mark the area around the fault relevant for Fig. 4.3. Deformation increases sharply with approach to the WF from the west. Although the outcrop situation is good, only few shear planes are identified in the fluid alteration zone (grey). Deformation elements become fewer at the eastern edge of the profile and outside the alteration zone. See text for details.

On the other hand the pattern may indicate an individual damage element distribution belonging to a further fault branch (denoted with dotted curve). We could not identify a distinct larger fault in this position, which makes the previous interpretation more likely.

Pursuing this interpretation, the West Fault is characterised by an approximately 1000 m wide structural damage zone (Fig. 4.2a), for which the deformation element intensity is increased. The fluid alteration zone is about 400 m wide. Its position is certainly influenced to a great part by the lithological contrast between andesites (west) to granodiorites (east). However, the constituents driving alteration need pathways and surfaces to react on, so it can be concluded that the altered part was most likely intensely fractured, too. The Gorila region (and surrounding area) does not exhibit a distinct fault core that is composed of a wide clay-gouge like that exposed in the Chuquicamata copper mine, so such a gouge was either not developed or is not preserved in the alteration zone.

Figure 4.2a resembles studies of other fault systems on different scales, which emphasises the scale independence of such fault related deformational patterns. Cello et al. (2001), for example, mapped a sharp increase of fractures along a 5 m scanline with approach to a cataclastic fault zone, which is bounded by a gouge with a marked decrease in deformation elements (his fig. 4). Schulz & Evans (1998) show how microscopic fracturing on a mm-scale increases in the vicinity of the fault core for a branch of the San Andreas Fault.

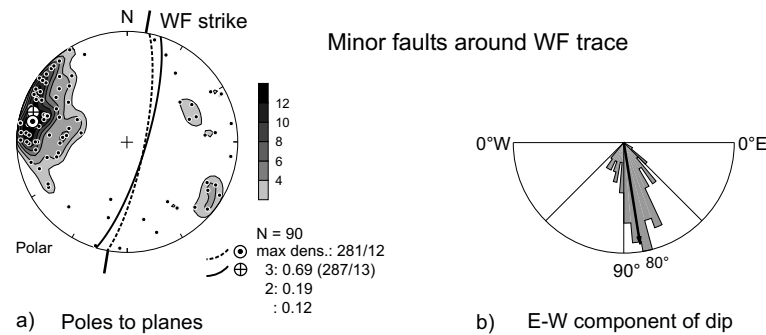


Fig. 4.3: a) Orientation of minor faults and colored bands (‘ribs’) in the immediate vicinity of the WF trace (within 400 m around the trace; see indicated corridor in Fig. 4.2b). Cluster and eigenvalue distribution, with corresponding great circles of mean planes are shown. b) W-E component of dip (arrow: mean dip and mean resultant length). Minor faults almost uniformly dip to the east with  $\sim 75^\circ$  from the horizontal.

In the previous section I stated, that slip surfaces and minor faults of the entire study area dip sub-vertical while west- and eastward dip is almost evenly distributed (Figs. 4.1a, d). In contrast to that the dip of minor faults in close vicinity to the WF trace defines a clear cluster and is very uniformly oriented towards the east. This is shown in Fig. 4.3a and b for all data within a strip reaching from 150 m west of the WF trace (so that data defining the two bars of maximum density element frequencies in Fig. 4.2a are considered) to 250 m to the east of the WF trace and well into the alteration zone (the considered area is indicated in Fig. 4.2b). The corresponding great circles that show the resulting mean fault plane orientation, fit perfectly to the strike of the WF trace and indicate a steeply dipping ( $\sim 75^\circ$ ) central part of the West Fault.

Several arguments presented so far suggest that the deformation elements mapped in the Gorila region are related to slip on the West Fault: (i) The predominance of sub-vertical *pseudo-B* axes that cluster within the WF plane (Fig. 4.1c), especially if the above inferred dip of the fault is considered. (ii) The orientations of minor (subsidiary) faults that lies within  $45^\circ$  to the west or east from the principle fault. (iii) The deformation elements themselves that occur within and define the damage zone (Chester & Logan, 1987).

### 4.3 Kinematic interpretation

Having shown that the majority of data fits into a deformational pattern controlled by approximately N-S oriented displacement, it is now attempted to relate deformation to distinct episodes. Firstly, a synoptic interpretation of the data is presented and the limitations of this approach are demonstrated. Secondly, a kinematic analysis of fault slip data outcrop by outcrop is carried out to investigate possible spatial reorganisation of the strain (rate) field in the vicinity of the West Fault.

#### 4.3.1 Synoptic analysis - multiple deformation events

The ‘dynamic’ history of the PFS and the West Fault segment, with its reversals of the sense of displacement, was described in section 2.2 and Tab. 2.1. This complex history leaves the geologist with a record of faulting and kinematic markers, representing the multitude of accumulated defor-

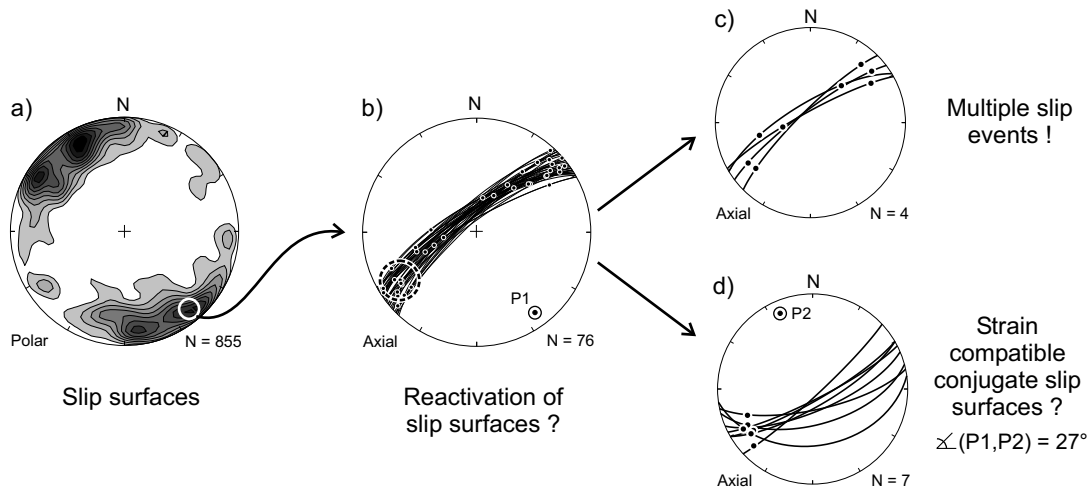


Fig. 4.4: Example for the kinematic heterogeneity within the Gorila region. The encircled cluster of slip surfaces in a) is shown as great circles with associated slicken-lines in b). The variable orientation of striae (dots on the great circles) on similarly oriented slip surfaces is a sign for reactivation of existing shear planes. This is corroborated by slip surfaces exhibiting several slip events (i.e. sets of slicken-lines) as in c). Conjugate sets of shear planes theoretically have slip orientation in common. Candidates that may be conjugate planes to the set of slip surfaces having striae within the encircled cluster in b) are separated from all data and shown in d). The mean poles P1 and P2 of the slip surfaces in b) and d) only span an angle of  $27^\circ$ , which deviates strongly from the theoretically expected value of  $60^\circ$  for conjugate fault sets in pure or simple shear (Scholz, 1990). Likewise, strain compatibility could not be proofed for most sets of slip surfaces that have similar slip orientations.

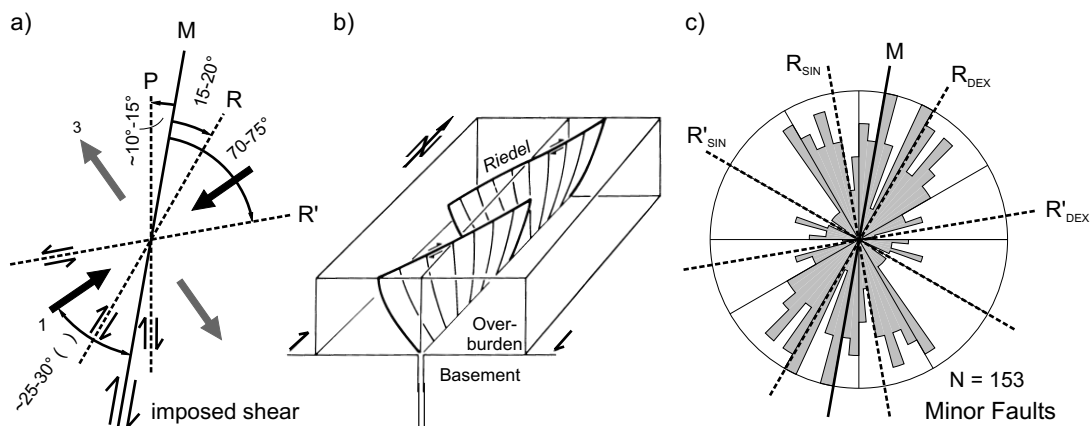


Fig. 4.5: Theoretical simple shear fracture geometry in a dextral system (mod. from Petit, 1987).  $\Theta$  is the angle between maximum horizontal stress  $\sigma_1$  and the master fault. Angles commonly observed range between  $15-40^\circ$  (Logan et al., 1992; Sperner, 1996) but can have great variability in natural rocks. R, R': synthetic, antithetic *Riedel* shears; M: master fault. b) Sketch of *Riedel*-shear development in the overburden above a simple sheared basement (based on sandbox experiments, see Sylvester, 1988 and Mandl, 1993 for references). c) Superposition of minor fault strikes and the simple shear fracture geometry of a). DEX refers to dextral, SIN to sinistral shear systems. The preferred subsidiary fault orientations fit to *Riedel*-shear geometry of a fault zone on which displacement reversals have occurred.

mation episodes. Figure 4.4 exemplifies the resulting kinematic heterogeneity in the Gorila region. Similarly oriented slip surfaces exhibit a wide variety of associated slip orientations (Fig. 4.4b) and even multiple slip events on single shear planes (Fig. 4.4c). Both indicates that reactivation of pre-existing damage elements must have played a significant role in the deformation history of the WF (Marrett & Allmendinger, 1990).<sup>1</sup> Strain compatible sets of conjugate faults are not prevailing the data (Fig. 4.4d). This may be expected because conjugate faults are typically neofomed, i.e. develop where fault surfaces did not exist prior to the tectonic event (Angelier, 1989).

Major orogen-parallel strike-slip faults develop in domains of simple shear (non-coaxial deformation; Sylvester, 1988). Natural fault studies as well as laboratory experiments show that simple shearing leaves a characteristic assemblage of subsidiary faults and fractures in the vicinity of the fault (e.g. Riedel, 1929), which maintains self-similarity from the microscopic to outcrop and probably greater scales (e.g. Tchalenko, 1970; Logan et al., 1992; Twiss & Unruh, 1998). The theoretical geometry of such fault sets is presented for dextral shear in Fig. 4.5a. The coalescence of *Riedel*-shears (R) plays a major role in the development of a through-going strike-slip fault, as illustrated by the sketch in Fig. 4.5b. Such sets of *Riedels* are often recognized in field surveys (e.g. Reutter et al., 1991 for the PFS; Cello et al., 2001; Wojtal, 2001). The mean NE-strike of slip surfaces in the Gorila region (great circles in Fig. 4.1a) may suggest a predominance of dextral simple shear in analogy to the R-shear orientation in Fig. 4.5b. This, of course, would imply that all NE-SW striking shear surfaces have right-lateral slip direction. In contrast to that, the slip direction of many shear planes was identified to be left-lateral. The data can thus not be explained with dextral simple shear alone.

In Fig. 4.5c the orientations of minor faults is compared to the theoretical assemblage of faults for simple shear (Fig. 4.5a). The master fault's strike (M) can be identified as a preferred orientation. Two further strike concentrations are symmetrically oriented to M, forming acute angles with the latter. These preferred strikes may be attributed to *Riedel*-shears (R) of a dextral respectively sinistral simple shear domain, again suggesting slip reversals along the WF. Antithetic *Riedel*-shears (R') seem to be less frequently developed. This lack of antithetic *Riedel*-shears (R') in dextral shear systems has also been observed by Reutter et al. (1991, 1996) in the PFS structural pattern of the Sierra San Moreno (west to the WF) and the WF segment in the Chuquicamata copper mine.

Reactivation of shear planes and simple shear fracture geometry with two opposing senses of displacement are in agreement with other studies on the PFS and the West Fault (e.g. Günther, 2001, Reutter et al., 1996, Dilles et al., 1997). For example, Günther (2001) defines a ~ 20 km wide 'central structural domain' north of Calama, bounded to the east by the WF system. The author points out that the kinematic data collected in this domain show conspicuous signs of fault slip reversals both in a synoptic as well as local interpretation of the data. An outcrop scale interpretation of the kinematic data of the Gorila region follows in the next section.

### 4.3.2 Outcrop by outcrop analysis - paleo-strain / stress reconstruction

The above described heterogeneity of the structural data makes it necessary to deduce the kinematic properties, i.e. the principal strain (-rate) axes – or stress axes – from a smaller scale analysis. A

<sup>1</sup>In this context, the oblique slip component of the damage element characteristics in Fig. 4.1 (sect. 4.2.1) may be regarded as resulting from fault reactivation (e.g. Angelier, 1984).

*regional* kinematic solution could only be obtained if the prerequisites of a homogeneous (isotropic) rock mass, coaxial deformation and no mechanical interference of adjacent slip surfaces are matched (Twiss & Unruh, 1998; Marrett & Allmendinger, 1990). Since this is certainly not the case in a fault zone with overall non-coaxial deformation, the following analysis concentrates on incremental deformation on the local outcrop scale and consequently deduces *local* strain/stress orientations. It was therefore attempted to separate the data into homogeneous populations for which a strain tensor with principal extension (T) and shortening (P) axes can be identified<sup>1</sup>. The main assumption that governs the kinematic interpretation is that the slip direction on a shear surface is parallel to the maximum resolved shear rate on this surface. A step further, the kinematic tensor can be regarded as stress tensor with P corresponding to  $\sigma_1$  and T to  $\sigma_3$  (coaxiality of principal stress and strain axes) if Bott's (1959) assumption is followed that the fault's slip also records the direction of maximum shear stress on its surface.

We attempted to identify the slip sense for each slip surface / striation data pair (fault slip datum) by looking for slip indicators where displaced markers were not obvious (according to methods described in e.g. Doblas, 1998 or Petit, 1987). However, the sense of slip, especially in a multiply deformed region, is seldomly unambiguous and its definition is often based on the clarity or dominance of indicators in favour of one direction. The slip-sense determination is thus a potential source of error, which contrasts its importance as constraint for the kinematic interpretation. Unfortunately, the time sequence of different deformation episodes remains vague due to the lack of clear cross cutting relations of differently oriented striae on a single plane. The reconstruction of paleo-kinematics must therefore be regarded with much care and treated as a qualitative description of the deformation within the study area. Quantitative estimates of strain based on fault slip data are not obtained since the amount of slip on shear surfaces is unknown. Consequently, the fault-slip data were treated with identical weights.

### Separation of data

The separation of data of an outcrop into several  $\pm$  homogeneous populations is an iterative process involving three main steps. This procedure is demonstrated below with the help of Fig. 4.6 for a rather complex data set (outcrop A19, cf. Appx. A.4). The stereoplot of the data in step 1 facilitates the recognition of fault geometries, such as conjugate *Riedel*-shears, for example. For outcrop A19 it is evident, that faults are not homogeneously distributed, but that NE- and NW-ward striking faults dominate. With the aid of several plotting methods (step 2, Fig. 4.6) it is now attempted to recognise fault-slip data, that may belong to common kinematic systems. In the tangent-lineation plot the slicken-line orientation is projected onto the fault's pole (Hoeppener, 1955). Arrows belonging to the same deformation event point towards a common shortening axes or away from a common extension axis. Additionally, kinematic shortening (P) and extension (T) axes are plotted for each fault-slip datum, according to (Marrett & Allmendinger, 1990). By assigning the angle  $\Theta$  between the shortening

<sup>1</sup>P and T are terms often used in kinematic analysis, although they abbreviate 'pressure' and 'tension', which are strictly speaking describing stresses. Throughout this work P, B (as intermediate) and T will be used, according to common practice, for strain field description and  $\sigma_1$ ,  $\sigma_2$  and  $\sigma_3$  for principal stresses. The terminology and the interplay of kinematics (deformation) and dynamics (stresses) is a matter of much discussion (see Tikoff & Wojtal, 1999; Pollard, 2000; Peacock & Marrett, 2000; Gapais et al., 2000; and references therein).

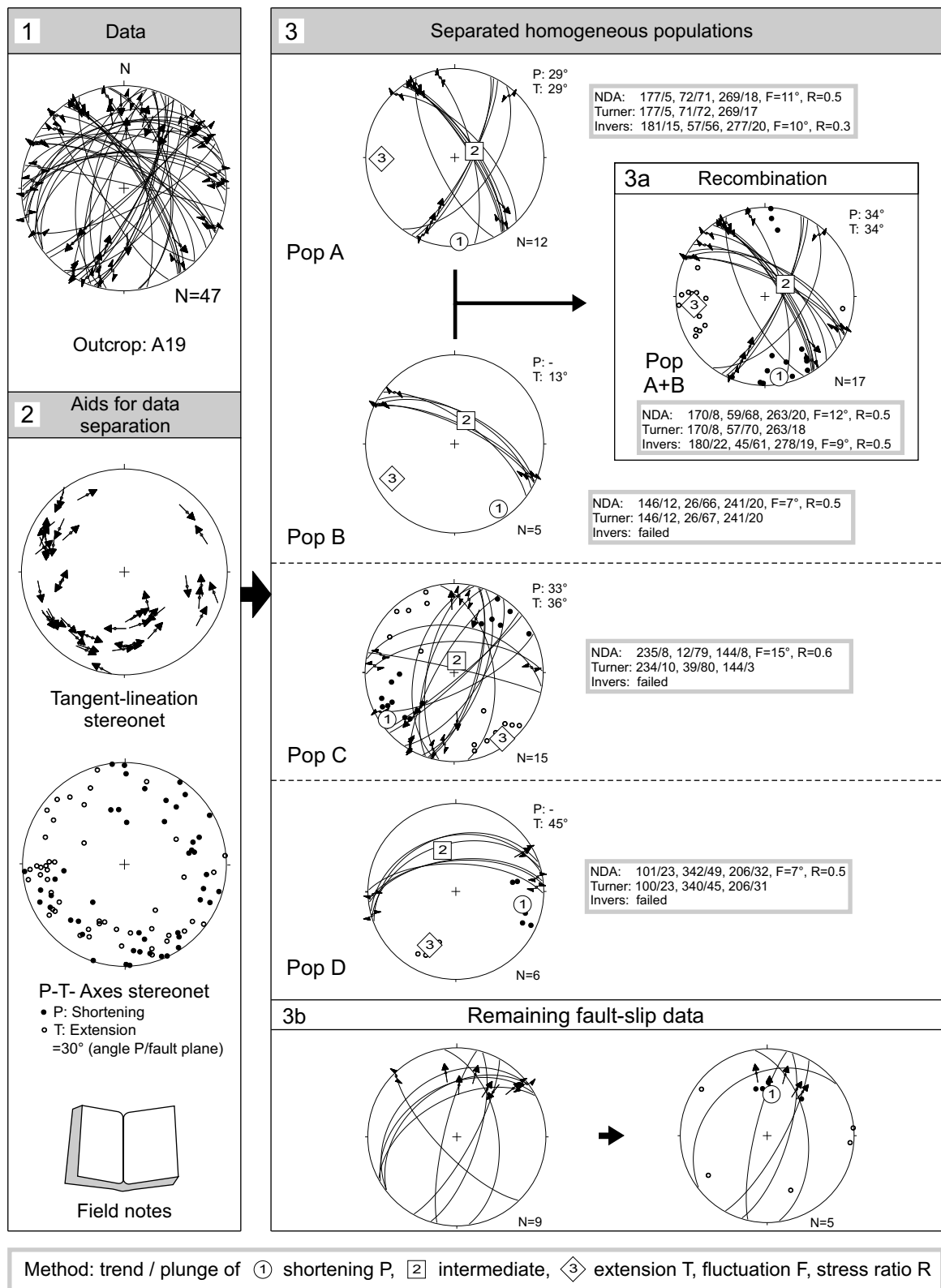


Fig. 4.6: Demonstration of data separation into  $\pm$  homogeneous populations for outcrop A19 (cf. Appx. A.4). The separation is mainly a three step, iterative process: 1) Fault-slip data. 2) Preliminary grouping of compatible fault populations with the help of different data plots and the incorporation of field notes. 3) Calculation of reduced stress tensors with several methods and verification of kinematic consistency, followed by regrouping of fault-slip data if necessary. The text will guide through this example in detail. Appx. A.1 outlines the applied stress analysis methods.

(P) axes and the fault plane, interpretation enters the data separation procedure. It is nonetheless a valuable aid to identify faults belonging to the same kinematic system, because their respective P and T-axes poles plot close to each other. A  $\Theta$ -angle of  $30^\circ$  is as a realistic estimate based on experience from laboratory and field studies on faulting (Sperner, 1996). The separation of data is further supported by incorporating information gathered in the field. It needs to be considered whether data are from a single rock mass compared to homogeneous distribution across the outcrop, whether several lineations are observed on a single surface or how the quality of the slip-sense indicators is rated.

Having achieved a preliminary grouping of the data into populations, the orientations of the kinematic axes and their relative magnitudes are calculated in step 3 (Fig. 4.6). Different methods from the fault-striae analysis program package by Sperner (1996) are applied. The principles and assumptions behind the respective methods (P-B-axes method or TURNER, numerical dynamic analysis (NDA) and a direct inversion method) are described in more detail in Appx. A.1. The results of these methods show, whether the grouped data can be interpreted as belonging to a single kinematic system. The angular deviation of measured orientation of the striation and predicted slip orientation corresponding to the derived bulk stress tensor can be checked for each fault-slip datum individually (the mean value is called fluctuation  $F$ ). In this way inconsistent fault-slip data can be removed from respective populations and reassigned to a different population. This process is aided by the program KINEMAT, which evaluates the clustering characteristics of shortening and extension axes on the basis of an eigenvalue analysis (Michel, 1993, 1994, see Appx. A.1). For a homogeneous population a value of  $\Theta$  (angle between P-axis and fault plane) should exist, which most tightly clusters the individual shortening (or extension) axes. Fault-slip data that strongly deviate from a common shortening (or extension) axes are not consistent with a homogeneous population. In the whole procedure it is attempted to assign as many fault slip data as possible to different homogeneous populations.

Finally, we result with several separated populations, all defining a different kinematic system: For outcrop A19, these are populations A-D in Fig. 4.6. It should be noted, however, that data separation never results in a unique, *final* solution. The principal stress axes orientations, that are obtained for the shown populations from the different methods are listed in Fig. 4.6 (grey boxes); the NDA result is plotted in the stereonets. NDA- and TURNER methods require the angle of  $\Theta$  as input parameter. Where it could be obtained, the angle that produces the most dense P-axes cluster, as calculated with KINEMAT, is used. Otherwise  $\Theta$  is set to  $35^\circ$ , taking into account that angles are greater in domains of slip surface reactivation. The angles that result in best clustered P- (or T-) axes distribution, are stated for each population in Fig. 4.6 (upper right corner of stereonets).

Separated populations are recombined if their kinematic axes are similar. This is the case for populations A and B in Fig. 4.6 (step 3a). The population A+B describes a strike-slip kinematic system with subhorizontal shortening and extension axes and a subvertical intermediate principal axes. For such solutions, both shortening *and* extension axes define a dense cluster (here  $34^\circ$ ). This is in accordance with a stress ratio  $R$  close to 0.5 (ratio of magnitudes of the principle stress axes; cf. Appx. A.1). On the N10°E striking West Fault the stress field resolved with population A+B causes sinistral slip.

Population C as well resolves a strike-slip kinematic system. Here, the stress orientation would cause dextral slip on the West Fault. Population D describes an oblique-slip system with a predominating strike-slip component. The slip surfaces of this population are confined to a distinct block in



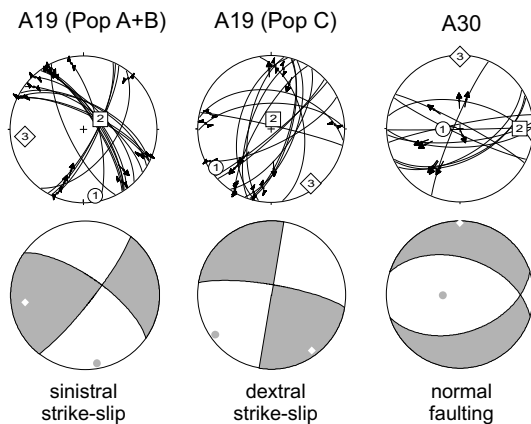


Fig. 4.7: Representation of kinematic analysis results as pseudo-focal mechanisms for some examples. The orientation of shortening (1, black dots) and elongation (3, white squares) are used to construct two mutually perpendicular nodal planes that delimit quadrants of compression (white) and dilation (black). The intersection of the nodal planes is equivalent to the intermediate kinematic axes (B or  $\sigma_2$ ).

the outcrop and record a deformation event which is different from populations A+B and C. Finally, there remains a number of nine fault-slip data (Fig. 4.6 step 3b), that do not fit in any of the above populations. The P-T-axes distribution of five of these data (for one datum the slip sense has been reversed) indicate a P-axes cluster with a mean plunge of  $50^\circ$  and distributed extension axes that are close to the circumference of the stereoplot. This records extensional deformation.

### Paleo-kinematic results

The incremental kinematic tensors are visualised with the help of (pseudo-) focal mechanisms (or 'beachballs') in which the shortening and extension axes define compressional and extensional quadrants<sup>1</sup> (see Fig. 4.7). The entire set of results is shown on the map in appendix A.4. A beachball representation facilitates discrimination between different types of deformation (Fig. 4.7). For example, strike-slip kinematics with subhorizontal shortening ( $\sigma_1$ ) and extension ( $\sigma_3$ ) axes and an almost vertical intermediate axis clearly predominate the Gorila region (first two rows and most of third row beachballs on map A.4). A second set of normal faulting kinematics with subvertical  $\sigma_1$  and more or less horizontal extension  $\sigma_3$  is evenly distributed throughout the study area (fourth row on map A.4). Below, the resulting paleo-kinematics will be first described. Interpretation and comparison of the results with published data of regional studies along the PFS north of Calama follows in the next section.

The distribution of shortening axes  $\sigma_1$  for the strike slip systems is shown in a composite stereogram in Fig. 4.8. Quadrants in which  $\sigma_1$  axes result in right-lateral (dex) or left-lateral (sin) displacement on a vertically dipping master fault (WF) are labelled accordingly. Note that the identified clusters of shortening axes must be regarded as a spatial and temporal average for the Gorila region. The enumeration with roman digits helps to discriminate the various deformation regimes.

- I. **SW-NE shortening:** The clearest cluster in Fig. 4.8 forms for  $\sigma_1$  axes having approximately SW-NE horizontal orientation. This indicates right lateral displacement on the WF System, either belonging to the Late Eocene or the Miocene-Pliocene episode of dextral shear (see Tab. 2.1). The corresponding  $\Theta$ -angle between the fault plane and the horizontal principal shortening axes  $\sigma_{1h,dex}$  spans  $49^\circ$ .  $\Theta$  is often used to judge a fault's resistance to shearing (see sect. 4.3.3).

<sup>1</sup>The results will be treated as local palaeo-stress indicators, keeping in mind that the analysis itself actually deals with strain.

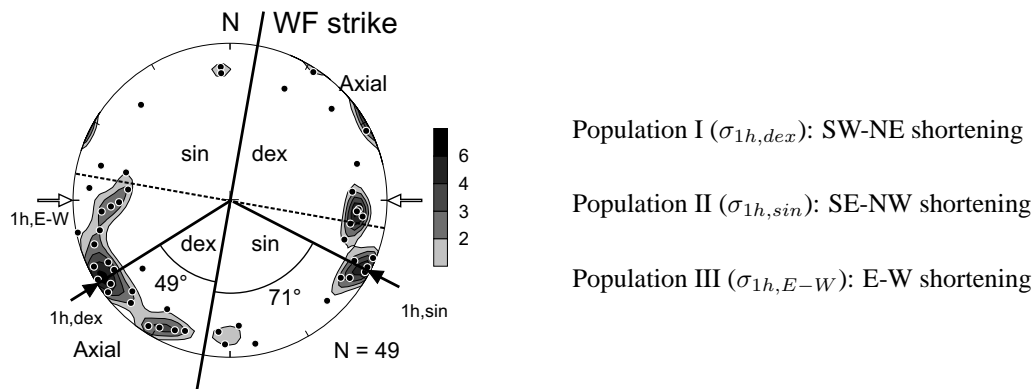


Fig. 4.8: Orientational distribution of all shortening (compression,  $\sigma_1$ ) axes of strike-slip kinematic results in an equal area, lower hemisphere stereogram with density contours (see Fig. 4.1). The quadrants for which *dextral* or *sinistral* slip would result on faults striking parallel to the West Fault are indicated. A reasonable angle  $\Theta$  of  $49^\circ$  between averaged  $\sigma_1$  and the fault results for the dextral solution, suggesting slight weakness of the fault. The angle of  $71^\circ$  for the sinistral solutions would signify considerable fault zone weakening. Arrows on the circumference denote maximum horizontal shortening orientation ( $\sigma_{1h}$ ) for the respective deformation regimes (often abbreviated with  $S_h$  in the literature).

- II. **SE-NW shortening:** A second set of shortening axes in Fig. 4.8 falls into sinistral quadrants and exhibits approximately SE-NW horizontal orientation (with emphasised E-W component;  $\sigma_{1h,sin}$ ). The timing of left-lateral displacement is constrained to Late-Eocene to Oligocene (Miocene?) time (see Tab. 2.1). A  $\Theta$ -angle of  $71^\circ$  for  $\sigma_{1h,sin}$  results.
- III. **E-W shortening:** A fair amount of  $\sigma_1$ -axes in Fig. 4.8 has an E-W oriented horizontal component, indicated by blank arrows in Fig. 4.8 ( $\sigma_{1h,E-W}$ ). This orientation of  $\sigma_1$  is mechanically unsuitable to produce slip in either direction on the principle fault since it results in very low amplitude shear-components on the fault plane.
- IV. **Normal faulting:** The remaining kinematic systems of the Gorila region all exhibit extensional deformation. Figure 4.9b shows the spatial distribution of normal faulting tensors in the Gorila region (see as well Appx. A.4). Normal faulting is evenly distributed throughout the study area and certainly represents the youngest deformation event according to the good quality and state of preservation of the slicken-lines. Interestingly, the prevailing orientation of the horizontal component of extension axes ( $\sigma_3$ ) changes across the fault: E-W to NW-SE extension predominates west of the WF and N-S extension east of the fault.

### 4.3.3 Discussion of results with reference to published studies

- I. **SW-NE shortening:** Several regional studies of the PFS and the WF system have identified kinematic tensors with SW-NE shortening axes, too, and attributed these to the dextral deformation events of the WF system (Günther, 2001; Reutter et al., 1996; Tomlinson & Blanco, 1997a,b; Dilles et al., 1997). Reutter et al. (1996), for example, report dextral displacement on the WF several kilometers north of Chuquicamata and suggest that it is connected to the younger slip

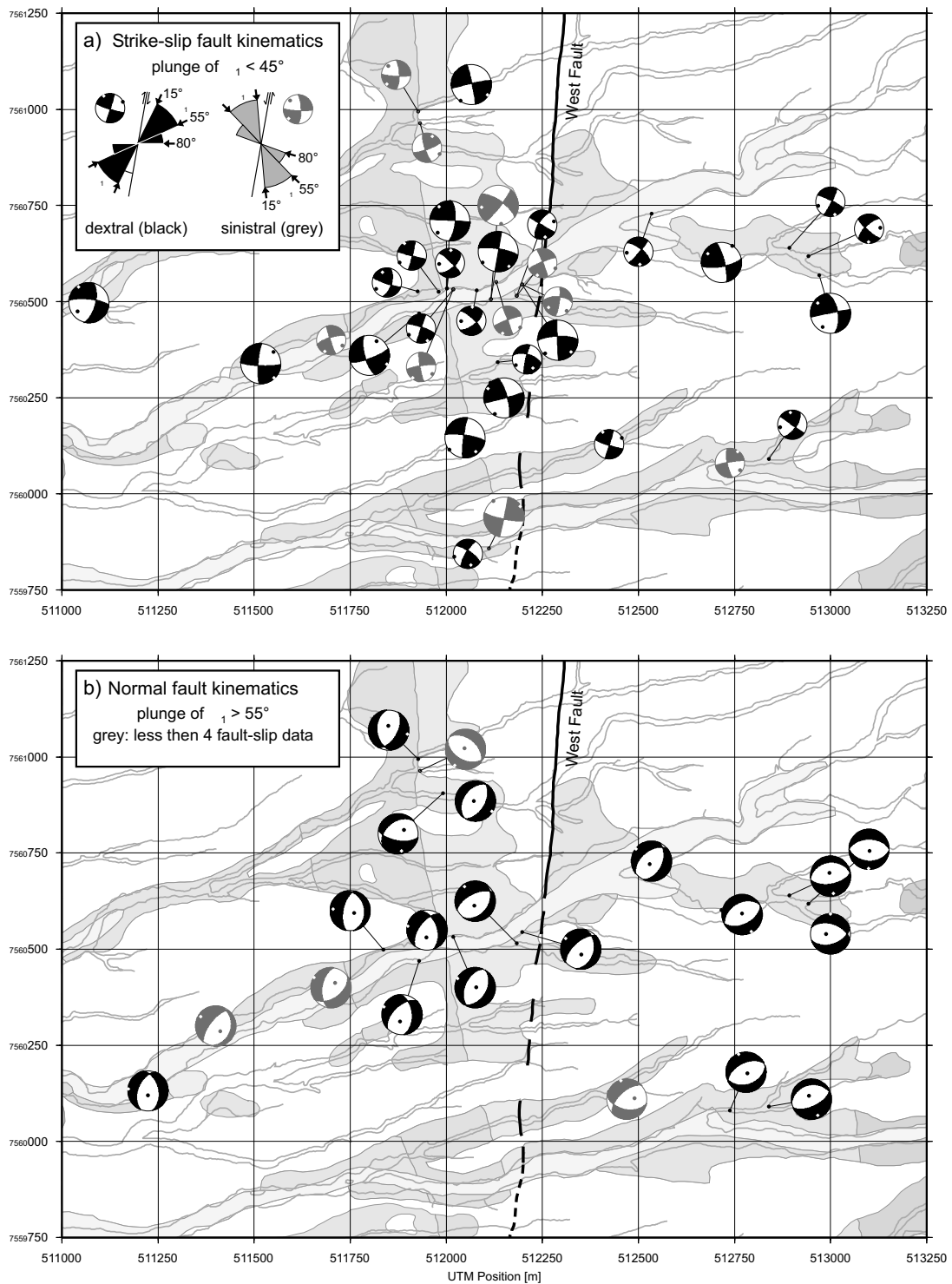


Fig. 4.9: Results of the kinematic analysis shown as pseudo focal mechanisms with white quadrants containing the  $\sigma_1$ -axis (compression). a) Strike-slip solutions with  $\sigma_1$  plunging less than  $45^\circ$ , grouped into dextral (black) and sinistral (grey) systems in relation to the strike of the West Fault. Two different ranges of  $\Theta$  ( $\angle$  between  $\sigma_{1,hor}$  and fault plane) are encoded with size of focal mechanism (see text). Dextral systems outnumber sinistral sense of shear. b) Normal fault solutions for  $\sigma_1$  plunging steeper than  $55^\circ$ . N-S extension is predominantly recorded east of the fault trace.

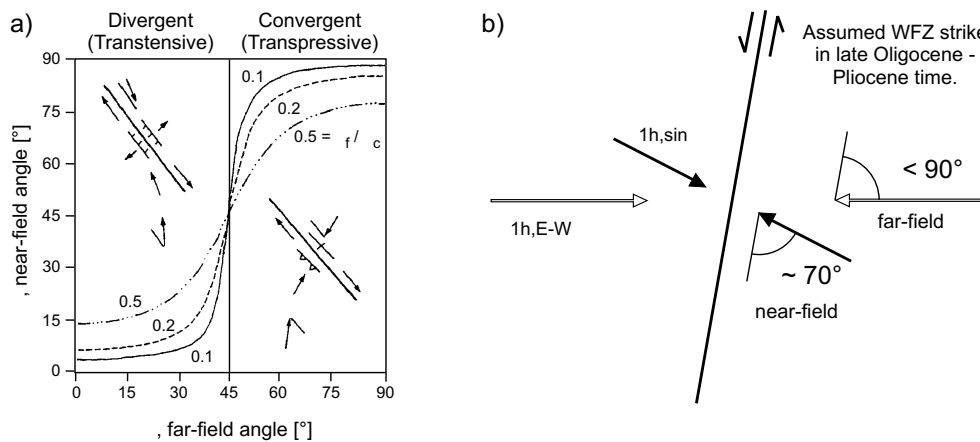


Fig. 4.10: Possible relation between far-field and near-field horizontal direction of maximum shortening for the late Oligocene-Pliocene sinistral deformation regime at the WFZ. a) Model of horizontal maximum stress rotation in vicinity of a large fault, assuming that fault strength is weaker than surrounding crustal strength (reproduced from Ben-Avraham & Zoback, 1992). Curves depict different ratios of frictional strength of the fault  $\tau_f$  and max. shear stress in adjacent crust  $\tau_c$ . b) Application to the West Fault Zone under the assumption that it had approximately the same orientation in the past as today. Assigning the orientations of  $\sigma_{1h,E-W}$  and  $\sigma_{1h,sin}$  to the far- and near-field, respectively, would make a high angle between the fault and  $\sigma_{1h,sin}$  possible, if compared with the model prediction for a convergent system in a).

reversal from sinistral to dextral in analogy to the crosscutting relations they observed in the Chuquicamata copper mine.

The  $\Theta$ -angle often  $49^\circ$  between the fault plane and the horizontal principal shortening axes  $\sigma_{1h,dex}$  does not indicate marked fault weakening averaged over time<sup>1</sup>.

II. **SE-NW shortening:** This approximate orientation of shortening is as well resolved in the above cited studies. Yet, the horizontal  $\sigma_1$ -component can exhibit quite some orientational variability among different investigated areas (cf. Günther, 2001).

A  $\Theta$ -angle of  $71^\circ$  for  $\sigma_{1h,sin}$  would indicate substantial fault zone weakening. However, under the assumption that the resolved dextral system is younger, this high angle can as well result from rotation of the older slip surfaces.

III. **E-W shortening:** In larger scale regional studies, E-W shortening is often observed. Günther (2001) attributes this regime to be the 'regional kinematic field' at distance from the West Fault, due to its consistency with large scale NW and NE trending lineaments in the central Andean forearc. Victor (2000) limits E-W oriented horizontal shortening along the western flank of the

<sup>1</sup>The laboratory determined coefficient of friction  $\mu_f$  ranges from 0.5 to 1 with hydrostatic pore pressure and frictional strength of the crust assumed to be isotropic (Byerlee, 1978). These values have been observed in nature for a wide variety of rocks (Byerlee's law). According to classical faulting theory this implies that the angle  $\Theta$  between the maximum compressive stress direction and the fault strike should be inclined at an angle of  $25-30^\circ$  ( $\Theta = 45^\circ - 0.5 \arctan \mu_f$ ). Higher angles are attributed to low frictional strength in the fault zone, for example resulting from reduced strength of the fault material or from elevated pore pressures (e.g. Rice, 1992). Accordingly, where slip is induced on active (preexisting) faults,  $\Theta$  may have higher values of  $30-45^\circ$  (Rutter et al., 2001). The classic example for a potentially weak fault is the San Andreas Fault, where  $\Theta$  spatially exceeds  $80^\circ$  (Hickman, 1991).

Altiplano plateau to the time period of plateau uplift from late Oligocene ( $\sim 30$  Ma) until Pliocene ( $\sim 5$  Ma)<sup>1</sup>. Within this time span left-lateral slip prevailed on the West Fault System (cf. Tab. 2.1), which is resolved by population II. The  $\sigma_{1h, sin}$ -axes of population II exhibit a relatively obtuse angle to the fault strike (see above). This may be explained with an E-W oriented transpressive far-field, assuming that the West Fault system was trending similarly at the time of sinistral displacement and that it was weak compared to the surrounding crust (Fig. 4.10; Ben-Avraham & Zoback, 1992). On the other hand, a reorientation of a transpressive stress field in the vicinity of a fault is mostly accompanied by thrust faulting with subparallel strike to the principle fault (e.g. along the San Andreas Fault (Miller, 1998); Fig. 4.10a). Thrust faulting, however, was not evident in the Gorila region and was not reported by Günther (2001) either. Victor (2000) reports E-W shortening with orogen parallel thrusts, which in conjunction with the N-S trending PFS, may hint towards this type of strain partitioning on a much larger scale. However, the interpretation of E-W shortening in the direct vicinity of the WF in the Gorila region remains speculative due to insufficient constraints on the timing of deformational events.

The spatial distribution of strike-slip kinematic systems, which are in accordance with displacement on the West Fault in either direction, is summarised in Fig. 4.9a. Black pseudo focal mechanisms signify dextral slip, grey solutions sinistral slip. The two sizes of the mechanisms denote in which angular range  $\sigma_1$  falls with respect to the WF plane (and parallel systems). Large beachballs have  $\Theta$ -angles, which are common for fault studies (e.g. Sperner, 1996). The small beachballs have  $\Theta$  ranging between  $55^\circ$  and  $80^\circ$ , that indicate substantial fault weakening, as it is, for example, postulated for the the San Andreas Fault (Rice, 1992). Reasonable right-lateral solutions (large beachballs) are five times more often than left-lateral beachballs. Most of the small beachballs have to be attributed to the almost fault normal regional deformation field (population III). It is impossible to infer a systematic reorientation of strain/stress tensor with proximity to the West Fault trace, which would certainly overrate the kinematic interpretation, too. Consequently, a strain partitioning between simple shear in the fault core and fault normal contraction (pure shear) in the damage zone and surrounding host rock as suggested by Chester et al. (1993) and Schulz & Evans (2000) for branches of the San Andreas fault, is not resolved.

It is widely believed that reactivation of faults in the brittle regime is controlled by the relative contrast of fracture strength of the fault zone material and the wall rock. Reactivation of fault movement along the same strand may thus classify the West Fault as a 'type-2 fault' in the sense of Mitra & Ismat (2001). Type-2 faults are softened due to progressive deformation and alteration. Succeeding deformation episodes use this weakness and form parallel or obliquely oriented fault zones which ultimately enlargens the fault damage zone.

**IV. Normal faulting:** Victor (2000) shows that the entire western edge of the Altiplano plateau is governed by NW-SE oriented transtension since the beginning of the Quaternary and probably lasting until today. The extension direction results from a superposition of the convergence vector and the westward oriented gravitational collapse of the plateau (see fig. 6.2 in Victor, 2000). Günther (2001) has as well reported NW-SE orientation of  $\sigma_{3, hor}$  within the Precordillera north of Calama. In summary the extensional deformation regime west of the WF in the Gorila region

<sup>1</sup>P. Victor's research area lies between  $20^\circ$ S and  $21^\circ$ S (Victor, 2000).

fits well into the regional pattern. NW-SE oriented transtension might as well explain some younger dextral slip on the West Fault (see I. further above).

How to explain the N-S oriented extension that seems to dominate the Gorila region east of the WF trace? According to Tomlinson & Blanco (1997b) and Dilles et al. (1997), the youngest dextral shear movements along the WF, which may coincide with the period of extension, only amount to a displacement of  $0.5 \pm 0.5$  km. It is therefore implausible to assume that the juxtaposition of two domains with differently oriented extension regimes is due to the displacement along the WF.

The only other account of N-S oriented extensional structures in the vicinity of the WFZ is described for the Chuquicamata copper mining area in Reutter et al. (1996): the authors infer »N-S stretching of the eastern block of Chuquicamata because, in the eastern block of Chuquicamata, very late extension is indicated by a few small normal faults roughly dipping towards the south«. These structures are seen in conjunction with gravitational collapse towards the Rio Loa depression to the south (cf. Fig. 2.1). Assuming that such gravitational collapse towards lower altitude regions is responsible for local extensional structures, then the restriction of these movements to the eastern blocks indicates, that the West Fault may still act as a plane of mechanical decoupling.

#### 4.4 The late stage alteration process

The wide alteration zone that accompanies the West Fault over kilometers and locally contains the large copper deposits, is a reminiscent of hypogene hydrothermal alteration and later stage (Miocene) supergene overprinting (Dilles et al., 1997; Ossandón et al., 2001; Cuadra & Rojas, 2001; see sect. 2.2). Geochemical analysis of rock samples collected in the alteration zone of the Gorila region provides constraints on the conditions (temperature, fluid source, fluid migration) under which late-stage alteration was active (see Janssen et al., submitted). A thorough discussion of the analysis of fluid-rock interaction goes beyond the scope of this work. However, some findings that are important in the context of this work are briefly described.

The analysed rock samples are all from the same rock unit (monzodiorites) and provide a half-profile trending perpendicularly from the WF trace towards the undeformed host rock in the east (cf. map in appendix A.4). Comparison of constituent variation is thus possible. Stable isotopes ( $\delta^{18}\text{O}$  and  $\delta\text{D}$ ) most clearly indicate the alteration conditions of the fluid-rock interaction. The isotopic composition of the less altered rocks is close to what is expected for primary magmatic water (Hoefs, 1987). Samples from the alteration zone, in contrast, show enrichment in  $\delta^{18}\text{O}$  and  $\delta\text{D}$  with proximity to the WF trace with values in the range of those typical for kaolinite weathering conditions (Shepard & Gilg, 1995). This indicates terrestrial low-temperature alteration conditions with alteration temperatures in the range of  $35^\circ$  to  $95^\circ\text{C}$ .

Furthermore, the altered rocks are depleted in alkaline earth elements while leaving the  $\text{SiO}_2$  content almost unchanged compared to the undamaged host rock. This is atypical for fault zones that developed in high temperature regimes (Gray et al., 1999, e.g). The less than expected solubility of quartz, while feldspar is dissolved and phyllosilicates precipitate, is again indicative for low temperature conditions (Fournier & Potter, 1982).

Finally, the isotopic composition of water from a cold spring located on the WF trace (see map A.4) was analysed and compared to river (Rio Loa) and rain water composition from the surrounding area (Aravena et al., 1999). River, rain *and* spring water have a  $\delta^{18}\text{O}$  to  $\delta\text{D}$  ratio characteristic for meteoric water, except for a positive  $\delta^{18}\text{O}$  shift of the spring water due to slight water-rock interactions. This implies that the storage period of the 'Gorila water' must have been relatively short and mixing with juvenile magmatic fluids did not occur.

From all this, it follows that the latest alteration processes are governed by low T conditions and that the infiltration of waters is of meteoric origin. Nothing indicates the involvement of brines ascending from greater depth (or generated by metamorphic reactions). However, laminated travertines that are exposed a few kilometers further north of the Gorila region may suggest involvement of brines in late Miocene-Pliocene time (Pardo, 1995; Maksaev et al., 1999).

## 4.5 Summary

The following summarises the observed structural characteristics of the Gorila region:

- The majority of deformation elements (slip surfaces with slicken-lines and minor faults) describe prevalent strike-slip deformation on subvertically oriented shear planes (Fig. 4.1).
  - Increasing deformation intensity with approach to the WF trace is evident from the damage element density profile (Fig. 4.2). Faulting and fracturing is not preserved within the alteration zone. The structural damage zone amounts to  $\sim 1$  km on the outcrop scale of investigation and the alteration zone is  $\sim 400$  m wide.
  - Damage elements of the fault core region dip steeply ( $\sim 75^\circ$ ) towards the east and strike parallel to the WF surface trace (Fig. 4.2 and Photos 2, 7 in Appx. A.3). Pseudo B-axes inferred from fault-slip data are subvertical and lie within the mean West Fault plane (pole: 281/12).
- $\Rightarrow$  The above three points give evidence that the majority of structural damage preserved in the Gorila region is related to deformation along the approximately N10°E striking West Fault.
- The deformation pattern shows slip reversals. Right lateral displacement (SW-NE oriented shortening axes) predominates over left lateral slip ( $\sim$  SE-NW oriented shortening axes; Figs. 4.8 and 4.9a).
  - The change of orientation of the extensional (normal faulting) pattern may suggest that the fault acted or acts as a zone of mechanical decoupling in recent times (Fig. 4.9b).
  - The preserved geochemical signature of rock samples from the alteration zone show that late stage alteration processes were active in a low temperature regime ( $35^\circ$  to  $95^\circ\text{C}$ ) and indicate the involvement of fluids of meteoric origin only.

The overall picture shows that we have here the type-locality for what Mitra & Ismat (2001) describe as: *»Repeated reactivation along the same fault may give rise to a thick zone of cataclastic rock, which is easily weathered and within which it would be difficult to find well-preserved evidence for distinguishing successive generations of structures at outcrop scale.«*

## 5 The magnetotelluric experiment

The previous chapter on the geological investigation showed how damage structures and alteration processes are related to deformation along the West Fault. It may be expected that these features also influence the subsurface electric current flow. This chapter therefore covers aspects of the magnetotelluric (MT) and geomagnetic depth sounding (GDS) experiments: from the actual measurements (sect. 5.1), processing of the data (sect. 5.2), presentation of the GDS results (sect. 5.3) and MT dimensionality analysis (sect. 5.4) to the modelling and discussion of the obtained results (sect. 5.5).

### 5.1 The magnetotelluric profiles

The MT and GDS data were measured in October 2000. The Main profile is 4 km long, consists of 26 recording sites and trends N110°E, hence perpendicular to the strike of the West Fault (refer to Fig. 3.1 and the map in Appx. A.4). The 20 sites at the center of the profile are 100 m apart of each other, while the site spacing of the remaining stations increases towards both ends of the profile. Two additional sites are situated on both sides of an electric power line in westward prolongation of the profile, to test if it has an effect on the experiment. A second profile, subsequently called 'South profile', is located roughly three kilometers further to the south and follows a valley that cuts the Cerros Guachos. The South profile is 2.5 km long with 9 recording sites and a site spacing of 300 m.

The principle site layout is shown in Fig. 5.1. Data were recorded in the frequency range from 1000 Hz to 0.001 Hz (1000 s) with four real time instruments S.P.A.M. MkIII (Ritter, 1995). The time-

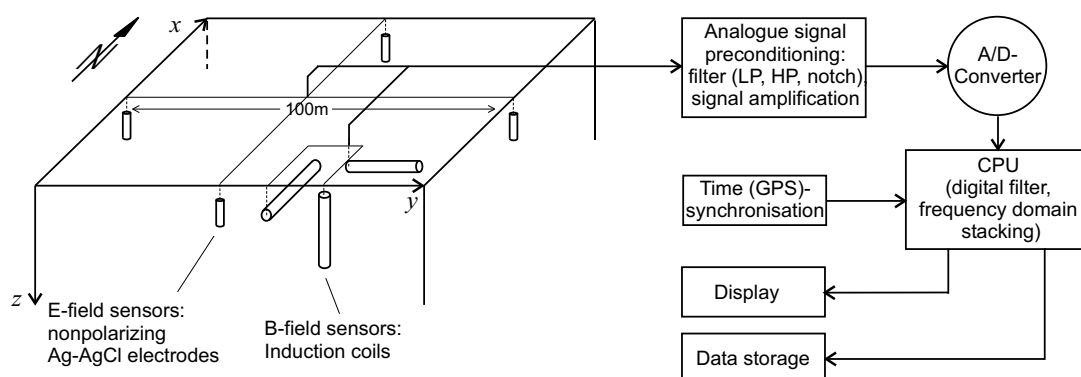


Fig. 5.1: Schematic layout of a MT/GDS measurement site and flow diagram of the data logging and real-time processing equipment. Electric and magnetic field sensors are either oriented parallel/perpendicular to the fault strike (Main profile) or according to magnetic north and east (South profile). LP: low pass, HP: high pass.



variations of the magnetic field are recorded with three induction coil sensors MFS05 (METRONIX), that are buried orthogonal to each other in the soil. Electric field variations are acquired as time-varying potential differences between two non-polarizing Ag-AgCl electrodes. The electrode spreads are oriented in the same way as the horizontal induction coils. To reduce the transition resistance of electrodes with the dry soil, the electrodes were swathed in wet bentonite clay. The instruments were usually left in the field for two days for continuous recording. A recording time of at least 24 hours was sought for every site and at least two sites were recording simultaneously. All systems were synchronised with the time signal from the Global Positioning System (GPS). The preliminary real-time processing of the data allows for immediate control of a sites quality and the functionality of the recording system.

The sensors along the Main profile are oriented parallel and perpendicular to the West Fault strike of N10°E. Thus, with electrode spreads of 100 m, the potential difference perpendicular to the fault trace is recorded for the entire length of the central part of the profile (in segments of 100 m). Such a configuration allows special treatment (spatial filtering) of small scaled near surface anomalies that might distort the electric field and cause frequency independent 'static shift'. Unfortunately, this method could not yet be applied to the data presented here. Along the South profile, with its greater site spacing, the field sensors were oriented with regard to magnetic north and east.

## 5.2 The data processing

The recorded time series were processed with the program collection EMERALD (Ritter et al., 1998). In a first step, noise resulting from the electric power line (the 50 Hz signal and its multiples) is extracted from the time series with digital notch filters. The time series are then segmented and fourier transformed into the frequency domain. Cross- and auto-spectra are calculated for specific target frequencies around which the spectra are averaged and which are chosen to be equidistant on a logarithmic scale. The magnetotelluric and magnetic response functions are calculated subsequent to stacking of the cross- and auto-spectra, using an iterative robust algorithm (Junge, 1994; Ritter et al., 1998).

The processed MT data, as they were used for the subsequent modelling, are presented in the form of apparent resistivity  $\rho_a$ - and phase  $\phi$ - curves in Fig. A1 in Appx. A.2. The overall data quality is high, as shown by smoothly varying curves over period  $T$  and consistent trend of  $\rho_a$  and  $\phi$  curves. Around a period  $T$  of 10 s, however, the data quality decreases owing to the reduced source field energy in the transition range of atmospheric and magnetospheric originated fields (often referred to as 'dead band'; Vozoff, 1991; Campbell et al., 1992). This effect is more pronounced in the XY component (TE-mode) than in the YX component (TM-mode) as shown in Fig. 5.2. Furthermore, the data quality is limited at periods  $T > 100$  s, where the recording time is too short to achieve a high signal to noise ratio. The data have therefore been subjected to a frequency domain editing of noisy frequency ranges / time spans prior to the robust processing, using the code EMSEL/SEL4ROB written by Weckmann (1999). Three criteria for the event selection were found to enhance the data quality and were applied solitary or in combination with each other:

1. Rejection of events that represent outliers with irregularly high or low signal energy.
2. Acceptance of those events only that exceed a fixed threshold value of the bivariate coherency

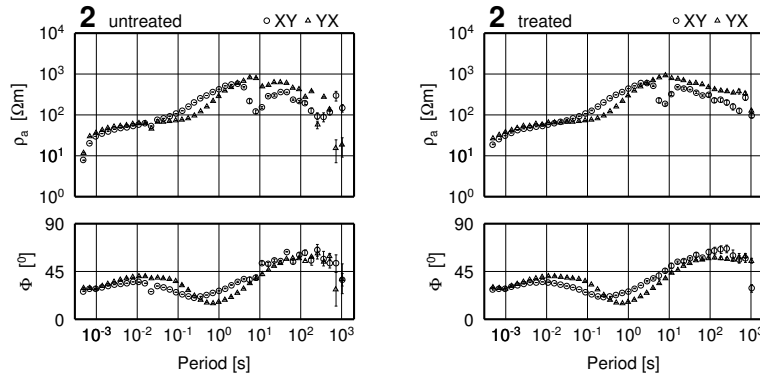


Fig. 5.2: Apparent resistivity  $\rho_a$  and phase  $\phi$  for site 2. The original data (left) are clearly improved (right) after selection of events in 'noisy' frequency bands such as the 'dead band' around  $T=10$  s or the long period data. The YX-component (TM-mode) generally yields better results. The event selection is preferentially aimed at enhancing the quality of the phase data, because subsequent modelling is emphasised on  $\phi$  compared to  $\rho_a$  (sect. 5.5). Note, that notch filters have eliminated the disturbed signal at 50 Hz.

between one horizontal E-field component and the two B-field components<sup>1</sup>.

3. In a predominantly 2D subsurface conductivity structure the phase  $\phi$  between the magnetic and the electric field according to equation 1.5 falls into a specific quadrant<sup>2</sup>. Events with phases outside the target quadrant are rejected ('phase criterion'). To apply this criterion the 2D character of the recorded data has to be verified first (cf. sect. 5.4).

Since two sites are usually recorded simultaneously, the 'remote reference method' could be applied additionally (Vozoff, 1991; Gamble et al., 1979). With this method, downward bias of the transfer functions caused by noise in the magnetic field components is reduced by the inclusion of magnetic fields of a distant reference site for the processing. Noise in the magnetic fields at the measurement and reference sites that is not correlated can thereby be eliminated. Application of this method improved data quality at a few stations where a distant reference site was available.

### 5.3 Geomagnetic depth sounding results

Before continuing with the analysis of the magnetotelluric data, some properties of the measured GDS data are presented. Although their interpretation is not the main target of this work, they provide important information and constraints for the MT interpretation. Maps with induction arrows visualise the distribution of lateral conductivity contrasts that separate regions of enhanced or reduced conductivity. The maps of Fig. 5.3 illustrate the measured GDS data for different frequencies (i.e. different penetration radii). As stated in section 1.3 the real arrows point away from conductive regions, while the length of the arrows is indicative for the magnitude of the conductivity contrast. The observations are now described separately for the high and low frequency range.

<sup>1</sup>For example, the bivariate coherency for the  $E_x$  output signal is  $r_x^2 = \frac{Z_{xx}\langle B_x B_x^* \rangle + Z_{xy}\langle B_y B_y^* \rangle}{\langle E_x E_x^* \rangle}$ , with  $\langle AA^* \rangle$  denoting autospectra. A coherency  $r_x^2$  of 1 signifies that the E-field can be completely explained from the B-fields.

<sup>2</sup>In that case, the  $E_x$  electric field component depends predominantly on the  $B_y$  magnetic field component compared to  $B_x$  and the phase  $\phi$  falls between  $0^\circ \leq \phi \leq 90^\circ$  (1st quadrant). In the case of  $E_y$  depending on  $B_x$  phase  $\phi$  falls between  $-180^\circ \leq \phi \leq -90^\circ$  (3rd quadrant, cf. page 8).

**High frequency range:  $f > 1$  Hz**

In the frequency range above 1 Hz the induction arrows of the Main and South profiles mirror a conductive region that is most likely related to the West Fault. Figures 5.3a and 5.3b give two examples. The subdivision of the maps into zones that trend parallel to the WF helps to explain the induction arrow characteristics.

Figure 5.3a shows induction arrows for a frequency of 64 Hz. According to the skin depth estimation of section 1.1 (eq. 1.2) this frequency corresponds to a penetration radius in the order of 0.6 to 2 km, depending on the bulk subsurface resistivity. The latter can be estimated from the MT apparent resistivity curves that generally trend between 100 and 1000  $\Omega\text{m}$  (cf. appendix A.2 or Fig. 5.13 in section 5.5.2). Looking at zone 2 first, the real arrows do all have a pronounced westward component, i.e. indicate a conductive region located to their east. The largest contrast, denoted by the longest arrow, is imaged at a site just west of the WF trace. In zone 4 the two real arrows closest to the boundary have large amplitudes and an east component. Thus, arrows in zone 2 and zone 4 indicate transitions to a region of higher conductivity that is approximately located in zone 3. These transitions are, of course, gradual and not distinct as implied by the zone boundary lines. In zone 3, the real arrows are very small, indicating a region of relatively homogeneous conductivity. Along the South profile (lower panel of Fig. 5.3a) it is possible to distinguish between three different zones. A region of enhanced conductivity (zone 2) is explicitly imaged by the large westward and eastward pointing real arrows of zones 1 and 3, respectively.

The induction arrows at 11 Hz, equivalent to a approximate penetration radius of 1.5 to 5 km, show a similar result (Fig. 5.3b). In zones 2 and 4 of the Main profile, the arrows indicate the good conducting region of zone 3 more pronounced than in the 64 Hz image. With increasing distance from the conductive zone 3 the real arrows of zone 4 become smaller, as expected. In zone 3 the real arrows change their orientation from pointing to the west to an eastward orientation, while the arrows are small again. The central arrows point towards the south and are almost parallel to each other. This could result from a lamellated conductivity structure oriented parallel to the WF: In synthetic models such real arrow behaviour is observed for a structure consisting of parallel lamellae of alternating good and poor conductivity (U. Weckmann, GFZ, pers. comm.; Pek & Verner, 1997).

The image for the South profile at 11 Hz is most striking. A conductive region (zone 2) can be clearly distinguished. The smallest arrow is located in the center. In addition, the westward and eastward pointing real arrows are oriented almost perfectly perpendicular to the WF trace, as it would be expected for a two dimensional conductive structure that trends along the fault. The almost parallel or anti-parallel alignment of the real arrows to their imaginary parts is as well indicative for a two dimensional geometry (cf. sect. 1.3).

A conductive zone of the type described for the two examples above is observed in the frequency range from about 700 Hz to 4 Hz. The principal part of the region of enhanced conductivity is always located to the east of the WF trace at both profiles.

A conspicuous feature of the Main profile are the three SW oriented real arrows of zone 1 in figures 5.3a and 5.3b. This type of arrows is characteristic over a broad frequency range (500 Hz - 5 Hz). However, the geologic map gives no hint to what may be responsible for this effect. It remains speculative whether a plio-pleistocene to recent drainage system that is located to the north of the three sites could be the cause (cf. map in Appx. A.4).

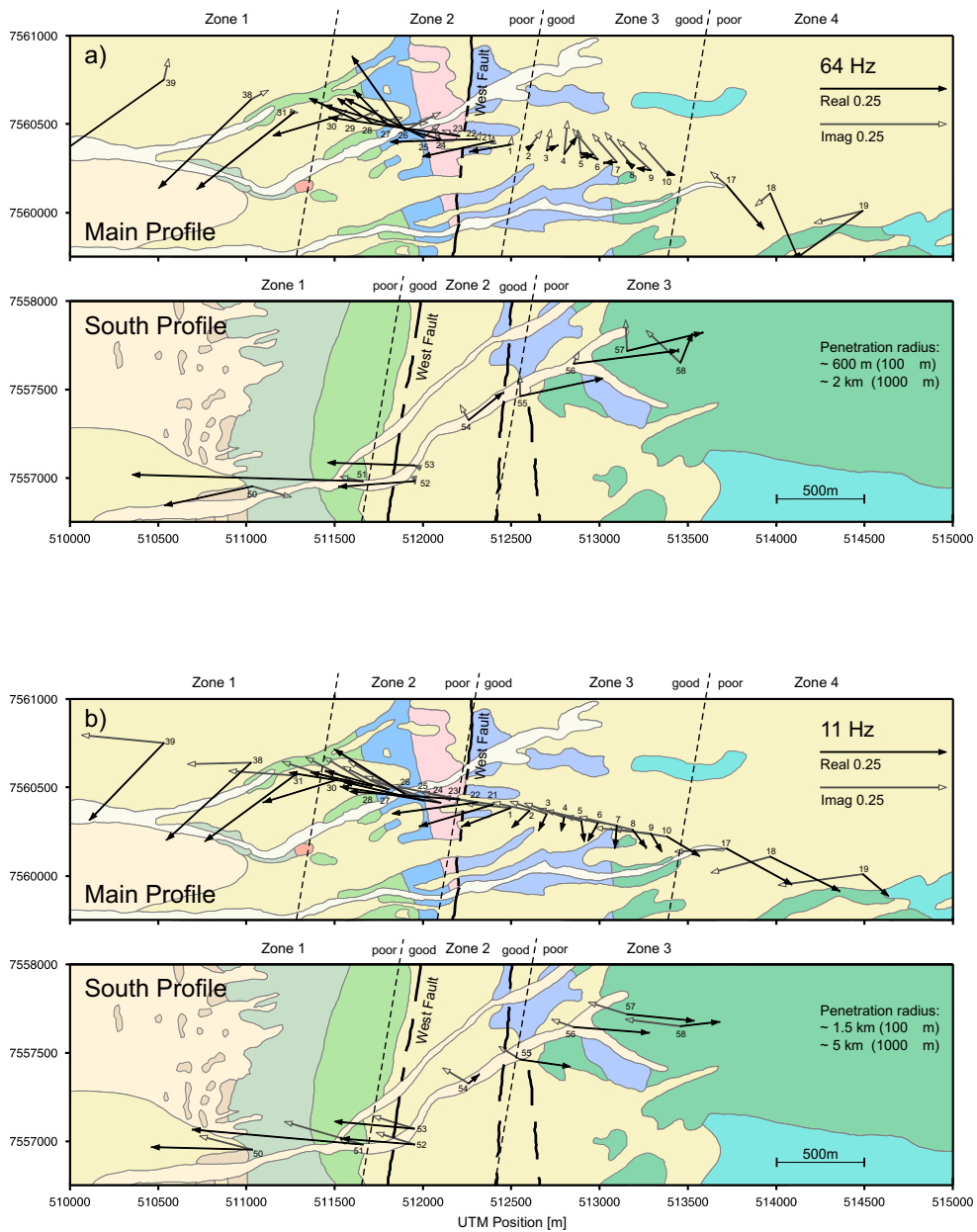


Fig. 5.3: Induction Arrows for the Main and South profiles at four different frequencies (figure continues on the following page). Real arrows point away from conductive regions (convention of Wiese, 1962), the length (amplitude) is a measure of the conductivity contrast. Real parts are marked in black, imaginary parts in grey with empty arrow heads. Error ellipses are drawn on real arrows. The penetration radius of the electromagnetic fields at a specific frequency is estimated from the skin depth equation (eq. 1.2) for two subsurface resistivity values. The subdivision into zones in figures a) and b) is used for explaining the behaviour of the induction arrows in relation to the West Fault Zone. The words 'poor' and 'good' denote the sense of the transition from a relatively poor to a relatively good conducting region. The background shows geologic units (cf. to map A.4). See text for discussion.

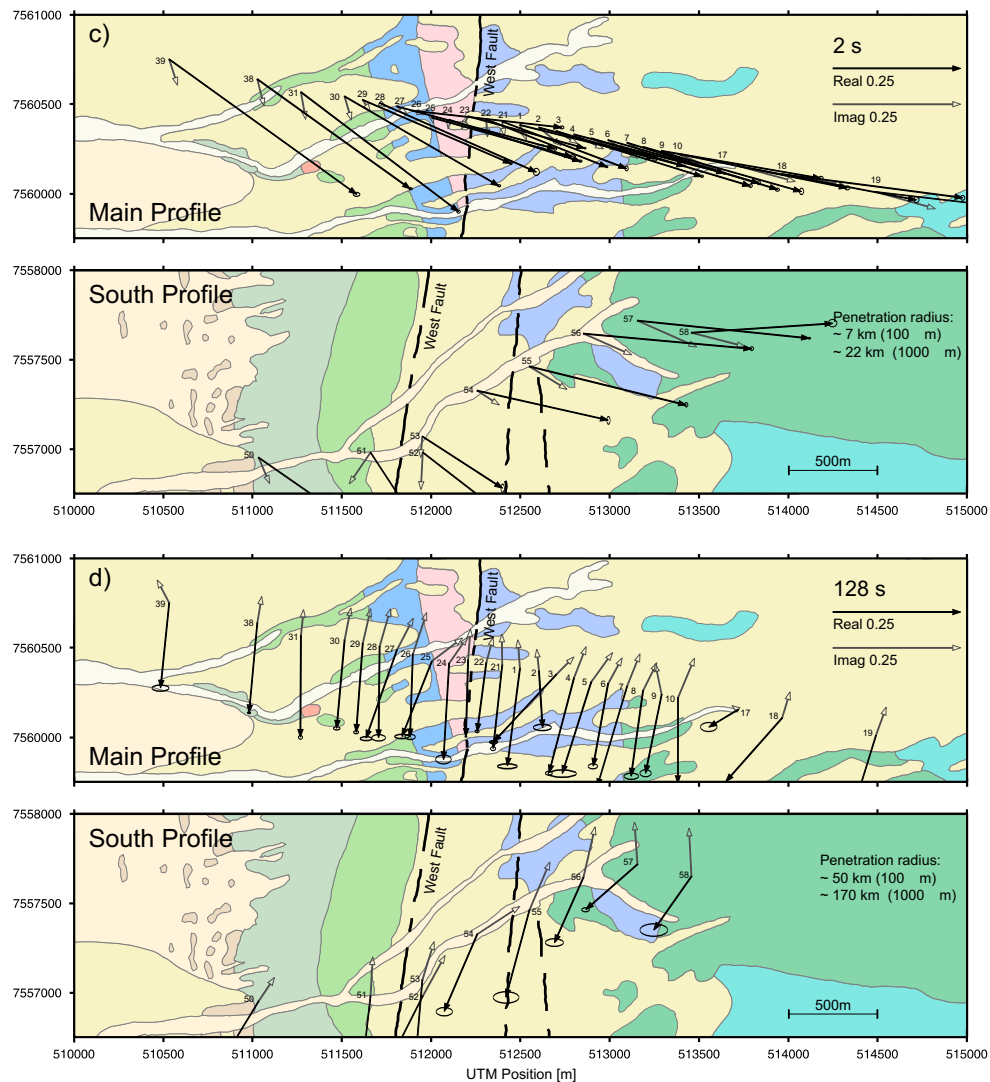


Fig. 5.3: Continued from previous page.

### Long period range: $T > 1$ s

The induction space exceeds the lateral extent of the two profiles in the period range above 1 s. Therefore, the imaged effects can not be (solely) attributed to the local West Fault structure. However, two characteristic induction arrow geometries of the long period range are also shortly presented.

In the range from 0.5 to 6 s the induction arrows uniformly indicate a conductive feature located to the northwest of the profiles. Figure 5.3c gives an example for the period of 2 s (penetration radius in the order of 7 to 22 km). The cause for this effect is not clear. The electric power line, trending N45°E and located around 4.5 km from the western end of the Main profile can not produce the observed effects. It may be possible that this behaviour results from the superposition of local effects seen in the high frequency range and a broad regional anomaly located at great depth ( $> 50$  km). The latter structure may be responsible for the induction arrows presented in Fig. 5.3d. Starting at periods of 32 s the real induction arrows uniformly point southwards on both profiles. Such southward pointing arrows have been systematically observed in other GDS campaigns in the North Chilean Precordillera

(e.g. Schwarz & Krüger, 1997; Echternacht, 1998; Schwalenberg, 2000; Janssen et al., 2002). So far, an explanation for this induction arrow behaviour in the long period range has not been found. It is, however, assumed that a large scale anisotropic structure oriented parallel to the Precordillera may contribute to the observed characteristics.

### Summary

The important result of the GDS data is their sensitivity to a region of enhanced conductivity for frequencies above 1 Hz. The induction arrows indicate a conductive structure with a strike parallel to the West Fault Zone. A two dimensional geometry of this structure is suggested, especially from the properties of the induction arrows along the South profile. The resolved region of enhanced conductivity lies to the east of the WF surface trace and extends over a width of  $> 500$  m.

## 5.4 Dimensionality and directionality of MT data

Under the assumption that deformation processes along the West Fault Zone are responsible for, or have influence on, the subsurface conductivity it is reasonable to expect that a two dimensional subsurface conductivity structure predominates at the relatively small scale of the MT/GDS experiment. In view of the surface expression of the West Fault in the Gorila region, this fault can be thought of as a two dimensional structure trending in N10°E direction. This is furthermore suggested by the induction arrow properties in the frequency range above 1 Hz, as demonstrated in the previous section. Consequently, the impedance tensor properties should as well reflect the fault zone orientation. That means, we ideally expect to find a rotation angle for the impedance tensor for which its elements exhibit 2D case characteristics and decouple into TE- and TM-mode (cf. sect. 1.2). This rotation angle is equivalent to the geoelectric strike of the subsurface current flow. It is therefore necessary to verify the dimensionality of the subsurface conductivity structure and to find the orientation of the electric current system prior to modelling the data. Because of the importance of this analysis for the interpretation of the data, various methods of determining dimensionality and directionality have been applied.

### Dimensionality

A simple analytical measure of the dimensionality of the impedance tensor (eq. 1.3) is the ratio of the diagonal elements  $Z_{xx}, Z_{yy}$  to the off-diagonal elements  $Z_{xy}, Z_{yx}$ . In the pure 2D case, which is in general not realised in nature, the former are zero. Swift (1967) introduced the rotationally invariant tensor skew  $S_{Swift}$ :

$$S_{Swift} = \frac{|Z_{xx} + Z_{yy}|}{|Z_{xy} - Z_{yx}|}. \quad (5.1)$$

$S_{Swift}$  equals zero in a 1D and 2D case, while non-zero values generally indicate the presence of 3D structures. Experience has shown that subsurface structures can be well approximated with a 2D interpretation if the skew has a low value. According to Swift (1967) this holds for values of  $S_{Swift} < 0.3$ . Fig. 5.4a shows a plot of the Swift skew values for each frequency of all measured sites (Main and South profile). The skew values are well below 0.3 for  $T \leq 10$  s and rise to higher values with increasing period. This suggests that a more complex conductivity structure is imaged with increasing penetration depth of the EM signal.

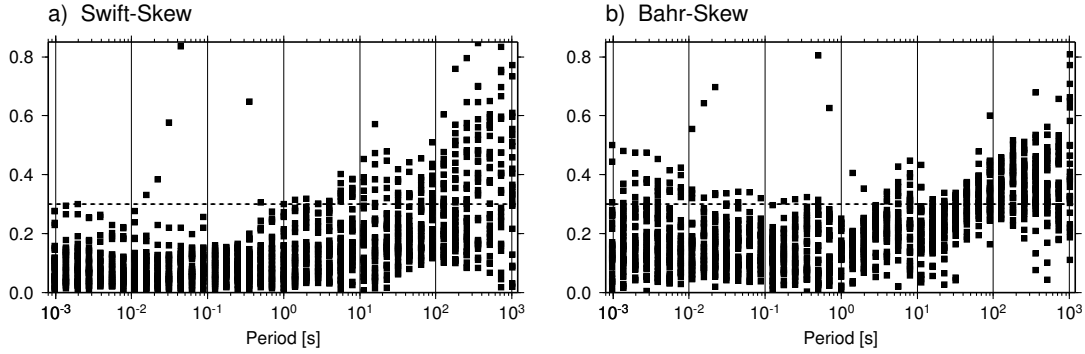


Fig. 5.4: Swift (a) and Bahr (b) skew values for all sites. The Swift skew values are well below 0.3 for  $10^{-3} \leq T \leq 10$  s. They systematically rise to higher values for  $T > 10$  s. Bahr skew values behave similar, although on a little higher level up to  $T = 10$  s.

More modern methods analyse dimensionality and directionality of the impedance tensor by assuming that it results from a superposition of regional and local conductivity anomalies (e.g. Bahr, 1988). Local structures are defined as being much smaller compared to the penetration depth of the EM signal for a specific frequency. The conventional Swift skew- (and electric strike-) determination is sensitive to the local or a combination of local and regional structures. Several decomposition methods have been developed to separate local, near-surface inhomogeneities from the underlying regional conductivity structure, which is normally the target of a MT study (see Smith (1995) for a comprehensive review). The Bahr skew value  $S_{Bahr}$ , shown in Fig. 5.4b, is based on a phase-sensitive formulation to evaluate the three-dimensionality of the regional conductivity distribution (Bahr, 1988). Again, values of  $S_{Bahr}$  above 0.3 cannot be explained by 2D or 1D models (Bahr, 1991). The behaviour of  $S_{Bahr}$  resembles the  $S_{Swift}$  value distribution, although the values are a little larger. Increasing Swift and Bahr skew values for  $T > 10$  s, however, indicate a complex 3D regional conductivity structure that is sensed with longer period EM signals. We therefore restrict the two dimensional interpretation of the data to the period range of  $10^{-3} \leq T \leq 10$  s.

### Directionality

We now have to check, whether we can assign a geoelectric strike to the subsurface current flow (i.e. to allocate TE- and TM-modes) for the above derived period range in which the subsurface conductivity structure may be approximated with a two dimensional geometry. This geoelectric strike is equivalent to the angle  $\theta$  about which the impedance tensor  $\hat{\mathbf{Z}}$  has to be rotated to minimise the sum of its diagonal elements (Swift, 1967; cf. sect. 1.2, page 8):

$$|Z_{xx}(\theta)|^2 + |Z_{yy}(\theta)|^2 = \min. \quad (5.2)$$

Again, local distortions produced by small scale inhomogeneities can be taken into account by fitting a decomposition model (Bahr, 1988). In all methods, the resulting strike angle  $\theta$  has a  $90^\circ$  ambiguity. To constitute the correct strike value additional information is needed that can be obtained from the geology or from the induction arrow constraints on the spatial distribution of lateral conductivity contrasts (cf. sect. 5.3).

Fig. 5.5 presents results of the geoelectric strike determination. The magnetic declination of approximately  $-2.3^\circ$  at the time of the experiment is taken into account in all calculations. Each of the

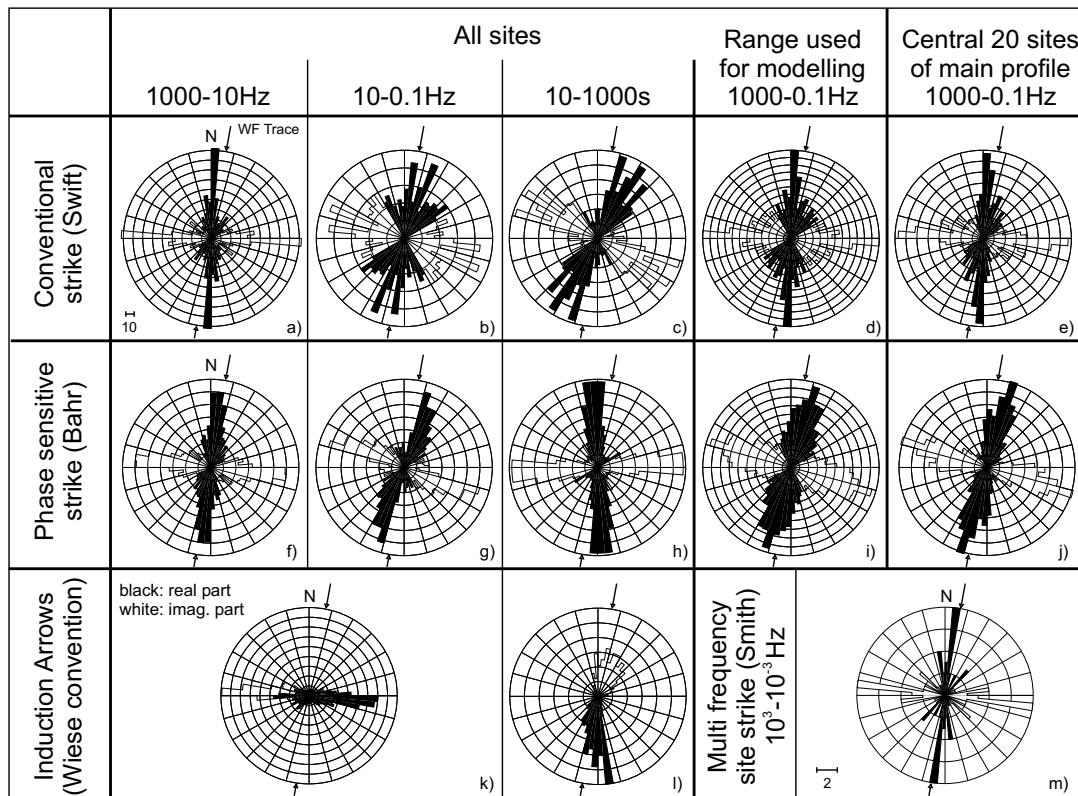


Fig. 5.5: Circular histograms of conventional strike (a-e; Swift, 1967) and phase sensitive Bahr strike (f-j; Bahr, 1988) for various frequency ranges. m) shows the multi frequency strikes of complete sites according to (Smith, 1995). In all histograms, except for m), a circle represents 10 data points. The black bars plot in the azimuth range between  $N30^\circ W$  and  $N60^\circ E$  which is the quadrant containing the West Fault's strike (indicated by black arrows). The white bars represents the  $90^\circ$  ambiguity of the strike angle. The directional information of the induction arrows (in the convention of Wiese, 1962) is shown in k) and l). Here, black bars denote the real induction arrows and white bars the imaginary parts. Note that induction arrows are oriented perpendicular to the conductivity contrast. See text for discussion.

circular histograms in the upper two rows of the figure gives the distribution of the strike angles for all frequencies within the respective band at all sites. The  $90^\circ$ -ambiguity is displayed by drawing the two possible orientations in black and white. Black bars plot into the azimuth range between  $N30^\circ W - N60^\circ E$  and  $S60^\circ W - S60^\circ W$ . These are the quadrants centered at the West Fault's strike (marked by little arrows). The first row (Fig. 5.5a, b, c) shows the Swift strike. Although the spectrum of calculated strike exhibits some variation, a great amount of angles is noticeably close to the WF strike. The scattering of the orientations is significantly reduced after applying the Bahr decomposition to the data (second row, Fig. 5.5f, g, h) and the 'regional' strike values are relatively uniform. In the higher frequency bands (f, g) the angles are in good accordance with the WF orientation, while in the band between 10 - 1000 s (h), the geoelectric strike slightly deviates towards the west compared with the WF strike. As an independent check of the underlying regional conductivity geometry Figs. 5.5k and 5.5l show the orientation of the induction arrows (here: black - real part, white - imaginary part). In the frequency range between 1000 - 0.1 Hz the eastward directed real arrows indicate a  $\pm$  NNE oriented



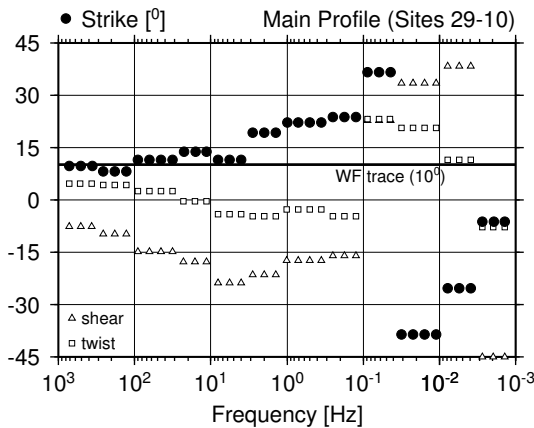


Fig. 5.6: Multisite, multifrequency decomposition of the 20 central sites of the Main profile according to McNeice & Jones (2001). Geoelectric strike and the West Fault orientation match in the frequency range between 1000 Hz and 5 Hz. The values become unstable for  $f > 0.1$  s. The twist and shear parameters are referred to in the text.

conductivity contrast. This is in good agreement with the impedance strike results for this frequency band. Contrary to that, the real part arrows between 10 - 1000 s point to a southerly direction, hinting to a feature with an E-W oriented lateral conductivity contrast. In the long period range, i.e. for great penetration radius of the EM fields, the electric strike as displayed in Fig. 5.5h can thus not be unequivocally attributed to the  $\pm$  NNE trending WF structure. Most likely, a larger scale feature is sensed that causes electric currents to flow in an E-W direction.

Instead of treating every frequency individually, as in the above demonstrated strike angle determination, it is attempted to derive a best fitting 'regional multi-frequency strike' for each site (Smith, 1995). The resultant strike value distribution is shown in Fig. 5.5m. Clearly, a majority of sites display a geoelectric strike equivalent to the WF orientation.

In a final test of directionality inherent in the data, the most appropriate geoelectric strike is calculated for a set of sites within predefined frequency ranges. This multisite, multifrequency approach by McNeice & Jones (2001) is an extension to the Groom & Bailey (1989) decomposition. Figure 5.6 shows the strike determination with a band width of half a decade for the 20 central sites of the Main profile. From 1000 Hz to  $\sim$  5 Hz geoelectric strike again matches the West Fault's strike. For frequencies in the range of 5 to 0.1 Hz, the determined angles range between  $15^\circ$  and  $23^\circ$ , which is consistent with the Bahr-strike in Fig. 5.5g. The low frequency spectrum with  $f < 0.1$  Hz ( $T > 10$  s) does not yield a stable strike. In addition to the determined strike two further parameters are shown in Fig. 5.6. As part of the decomposition of the impedance tensor, the twist and shear parameters can be used to assess the quality of the derived regional strike angle. These values should ideally not vary over frequency if a pure 2D regional structure is inherent in the data (Echternacht et al., 1997; Groom et al., 1993). While the parameters exhibit some smooth trend with frequency for the range between 1000-0.1 Hz, they strongly scatter for lower frequencies. This is in agreement with the scatter of the strike angles and the increase of skew values (Fig. 5.4) and accentuates the above stated insufficiency of a 2D model to explain the complexity of the regional subsurface conductivity structure for the period range greater 10 s.

To summarize the determination of the geoelectric strike angle, the Swift- and Bahr strikes of all sites are collectively plotted for the frequency range from 1000 - 0.1 Hz, for which the various methods exhibit a uniform behaviour (Figs. 5.5d, i). In the same way Figs. 5.5e, j show circular histograms of the central 20 sites of the Main profile. From all four diagrams, the close relation of the geoelectric

strike to the orientation of the West Fault is evident. This implies, together with the constraints from the induction arrows, that electric currents in the subsurface are most likely 'guided' by structures related to the West Fault.

### Conclusion

The dimensionality/directionality analysis results in a relatively uniform pattern for the frequency range between 1000 Hz to 0.1 Hz. Skew values are low ( $< 0.3$ ) and geoelectric strike reflects the West Fault orientation. A two dimensional model approximation of the data is well justified. In the middle frequency band (10-0.1 Hz) the strike values range about  $15^\circ$ - $20^\circ$ , which somewhat deviates from the West Fault strike of  $N10^\circ E$ . Nevertheless, the geoelectric strike is chosen in accordance to the high frequency range, since the main topic of this research is to investigate the fault/damage zone continuation from the surface downward. The most relevant information is resolved by higher frequency data where agreement with the WF strike is very good. Furthermore, rotation of the impedance tensor by  $10^\circ$  or  $20^\circ$  in the middle frequency range does not show a significant difference in the trend of the apparent resistivity and phase curves. Dimensionality and strike for the period range of  $T > 10$  s, however, suggest some 3D influence. Data analysis above periods of 10 s will therefore not be further considered for the 2D modelling.

The coordinate system in which to interpret the impedance data is thus defined by the West Fault strike of  $N10^\circ E$ . In this coordinate system the electric and magnetic fields are polarised either perpendicular or parallel to the West Fault trace. It follows, that the recorded XY-component is equal to the TE mode, i.e. currents are flowing along the  $x$ -coordinate axis (parallel to the faults strike; cf. Fig. 1.1). The YX-component equals the TM mode with the magnetic field being polarised tangential to the fault's strike. Rotation of impedance tensors for the sites of the Main profile is not necessary, since the data were recorded in this coordinate system from the start. The impedance tensors for sites of the South profile are rotated by  $10^\circ$  to be in a coordinate system aligned with the fault trace.

## 5.5 Inversion and forward modelling of MT data

In the previous section we found that the recorded MT data resolve a dominantly two dimensional structure related to the West Fault in the frequency range of 1000 - 0.1 Hz. An electric strike angle of 10° E results from the directionality analysis and TE and TM modes are defined by rotating the data into the respective coordinate system. The TE- and TM-mode data are now subjected to joint inversion modelling using the WinGLink<sup>1</sup> software package. It incorporates a 2D inversion module based on the code of Mackie et al. (1997) and Rodi & Mackie (2001). This finite-difference code starts from an a priori model, commonly chosen as homogeneous half-space, and calculates a forward response, which is 'compared' to the measured data. The algorithm seeks a 'minimum structure' model that minimises the least squares-misfit between observed and modelled data for each iteration. A regularisation parameter  $\tau$  controls the compromise between fitting the data and considering the model constraint, i.e. the model solution of the previous iteration. The larger the values of  $\tau$ , the 'smoother' is the model result at the expense of a worse data fit (Mackie et al., 1997). A thorough discussion of the role of the regularising term in the inversion algorithm is given by Schwalenberg (2000).

The result of an inversion depends on several parameters such as the  $\tau$ -value, the half-space resistivity of the subsurface or the assignment of error bounds to the data to be inverted. These parameters have to be carefully chosen. In the following section the inversion models regarded as best solution are presented, preceded by the determination of the important  $\tau$  value. The data fit and the influence of static-shift effects are evaluated. The model parameter and empirical sensitivity studies follow in section 5.5.2.

### 5.5.1 The inversion result

In order to find a  $\tau$ -value that guarantees a good fit to the data while resulting in a smooth (minimum structure) model, several inversions with different smoothness parameters  $\tau$  were calculated. The data errors are set to 10 % for apparent resistivities ( $\lg \rho_a$ ) and 2° for phases ( $\phi$ ). Thereby  $\rho_a$  is down-weighted with respect to  $\phi$ , which accounts for the proneness of apparent resistivities to static shift effects (see below) and the partly less well determined  $\rho_a$ -values compared to the phases (e.g. within the dead band, cf. Fig. 5.2). A homogeneous half space with a resistivity of 100  $\Omega\text{m}$  forms the starting model. The inversions run for a maximum of 100 iterations (to confine computational time), but in the majority of cases the misfit has converged to a constant level before reaching this iteration limit. Figure 5.7 shows the behaviour of the root mean square (rms) misfit with respect to the variation of  $\tau$  for the Main and South profile. The smallest rms-misfits within the iteration limit result for  $\tau$ -values equal to one or three, respectively. For both profiles the inversion converges with a  $\tau$  equal to three.

Fig. 5.8 shows the resulting models for the Main profile with  $\tau$  set to 1, 10 and 100. The increasing roughness of the models with decreasing  $\tau$  is evident. For  $\tau = 100$  a lot of information inherent in the data, especially at a depth of less than 1000 m (the high frequency range), is lost in favour of a smooth model. The model's fit to the data is expectedly bad (Fig. 5.7a). The  $\tau = 1$  and  $\tau = 10$  models resolve the same bulk features. However, rougher models result in a better fit to the data in the high frequency range (i.e. close to the surface). The best value in terms of rms-misfit, resolution of

<sup>1</sup>WinGLink® Software provided by Geosystem: <http://www.geosystem.net/>.

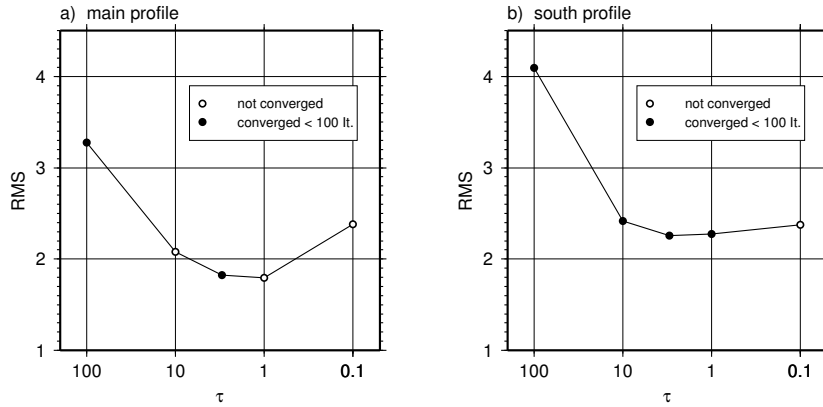


Fig. 5.7: Development of the rms error for inversions with differing smoothness parameter  $\tau$  for the Main profile (a) and the South profile (b). Filled circles denote inversion runs where the rms misfit of the final model converged to a plateau within 100 iterations. Rms errors vary little for  $10 \geq \tau \geq 1$  with smallest values for  $\tau = 1/\tau = 3$  and converging inversions for  $\tau = 3$  at both profiles.

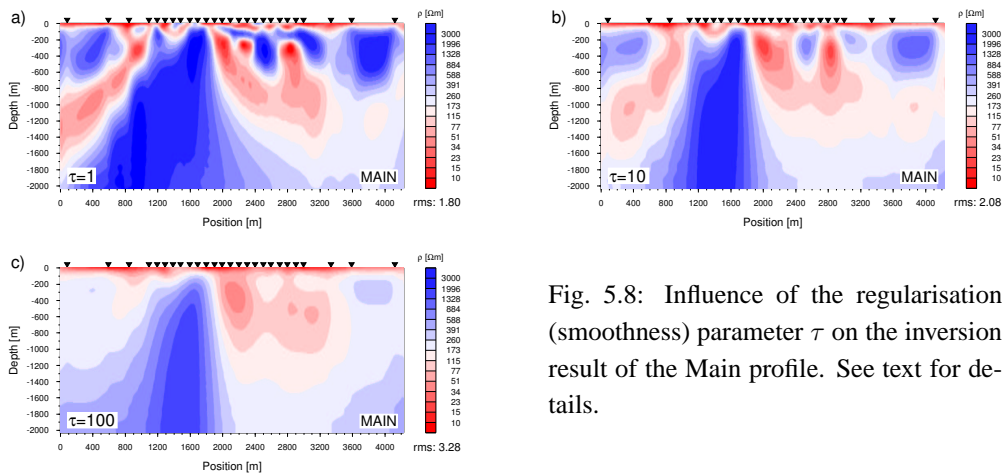


Fig. 5.8: Influence of the regularisation (smoothness) parameter  $\tau$  on the inversion result of the Main profile. See text for details.

shallow structures, smoothness of the model and computational time expense is achieved with  $\tau = 3$ , for which the inversion results are shown in Fig. 5.9.

### Model description

Fig. 5.9 presents the inversion results of the Main and South magnetotelluric profiles. The resistivities encountered range from 0.5 to  $7500 \Omega\text{m}^1$ . We first look at the Main profile, starting from its central part. Directly to the east of the West Fault surface trace (marked by the arrow in Fig. 5.9) lies a conductive structure (①) that extends to about 1300 m and dips steeply towards the east. It is flanked by a small focal point of higher conductivities (②). Separated from the central conductor (①) by resistive structure (⑥) lies a further conductive region (⑦). The geometry of this feature strongly depends on site 8 above it, as will be described later. The eastern edge of the model is composed of a resistive block (⑧) that becomes less resistive at 1000 m depth. To the west of the WF trace and directly bordering the central conductor (①) follows a broad and deeply reaching resistive struc-

<sup>1</sup>The resistivity color scheme is chosen so as to differentiate between structures of increased conductivity (red) and decreased conductivity (blue) compared to the mean apparent resistivity of all recorded sites ( $\sim 170 \Omega\text{m}$ ; cf. Fig. 5.13).

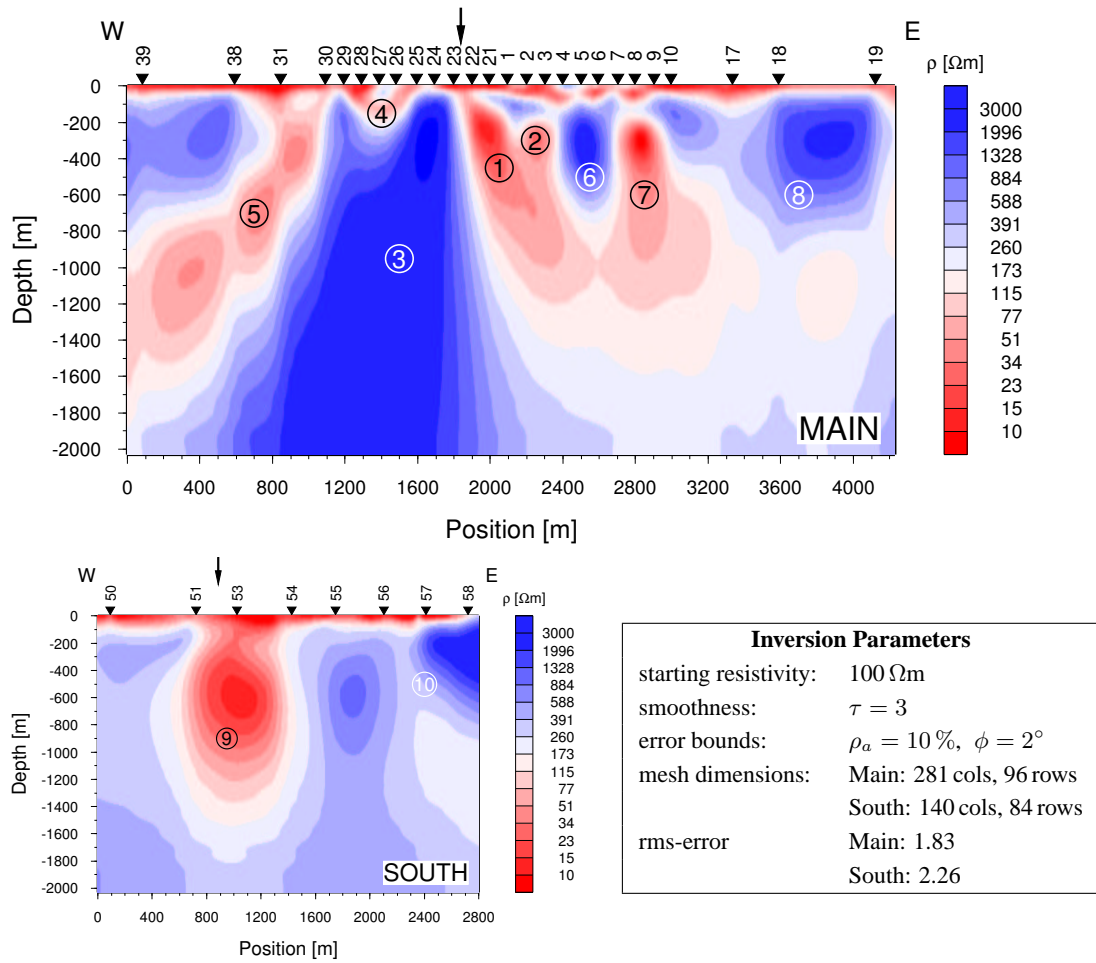


Fig. 5.9: Inversion models of the Main and South profiles. Black arrows mark the position of the West Fault surface trace. Numbers denote features referred to in the text. No vertical exaggeration.

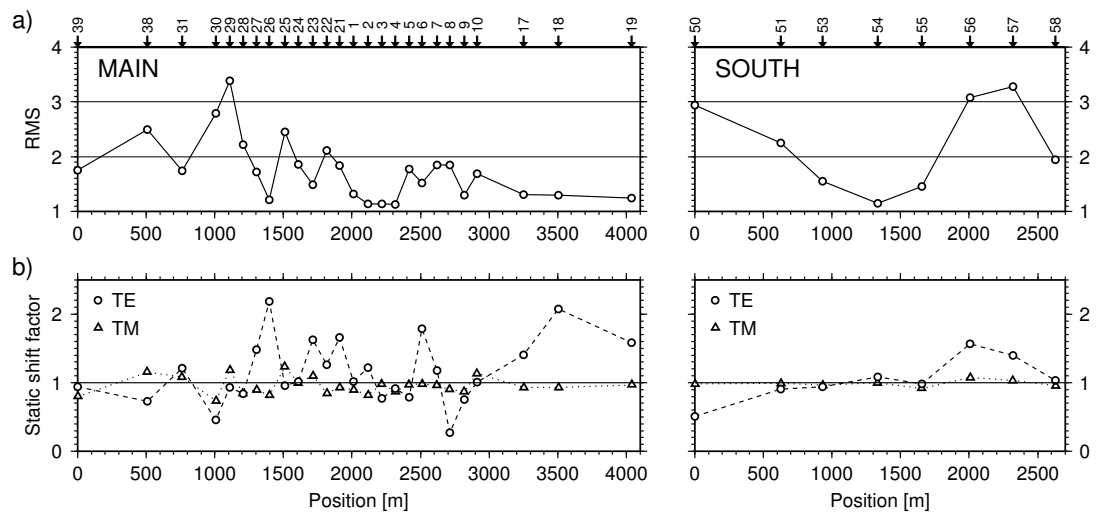


Fig. 5.10: Rms error (a) and static shift factors (b) for each site of the models shown in Fig. 5.9 (error floors:  $\rho = 10\%$ ,  $\phi = 2^\circ$ ). Shift factors greater one denote that the recorded data are linearly shifted to higher resistivities and vice versa. The data to model fit is shown in appendix A.2.

ture ③. In the shallow part this block is disrupted by a U-shaped conductive anomaly ④ that can be attributed to a small canyon (and its sedimentary filling), which the profile crosses in this position. The conductive anomaly ⑤ at the western boundary of the model seems to indicate a westward inclined structure. However, its geometry is less well resolved due to the increased site spacing and the anomaly's position at the edge of the model space.

The South model exhibits less complexity. Again, a conductive anomaly ⑨ is resolved in the immediate vicinity of the WF with highest conductivities encountered east of the surface trace. The anomaly reaches to a depth of approximately 1500 m, but its dip is not resolved due to the increased site spacing. A resistive block, comparable to ③ of the Main profile, is missing, as well as a further conductive structure (comparable to ⑦) in the eastern part of the profile. The resistive block ⑧ of the Main profile can be paralleled to anomaly ⑩.

### Data fit

The model solutions presented in Fig. 5.9 provide a very satisfying fit to the data, given in detail in appendix A.2. Fig. 5.10a shows the rms-errors for each site of the two profiles. What is the reason for the remaining misfit error? Most of the error is due to the reduced fitting quality at very high frequencies between 1000 Hz and 100 Hz, where features within the uppermost tens of meters are imaged (see  $\rho_a$ - and  $\phi$ -curves Fig. A1 in the appendix). The TE modes of sites 30 and 29 show some discrepancy among the phase and apparent resistivity behaviour in the dead band range between 1 and 0.1 Hz (Fig. A1), which could not be eliminated during the data processing. This deviation of the modelled from the measured phases is mainly responsible for the higher misfits in Fig. 5.10a, although the fit quality of TM-mode phases for frequencies  $< 10$  Hz is reduced, too. Increased rms values at sites 56 and 57 seem to result from a TE-mode apparent resistivity curve for frequencies below 10 Hz at site 57, which strongly differs from the curves at neighbouring sites (see Fig. A1 in the appendix). This curve results in a strong constraint for fitting the data at site 56, thus reducing its fit quality. Site 58, on the other hand, is located at the eastern boundary of the model where no further data constraints follow, so that determination of a conductivity structure is possible that very well fits the data of site 58<sup>1</sup>. Site 50, being of bad data quality, is mainly used in the inversion to enlarge the model space to the west and only contains a few data points (cf. Fig. A3 in the appendix).

### Static shift effects

Static shift is the result of electric charges accumulating along boundaries of conductivity anomalies very close to the surface (Vozoff, 1991). These charges can produce a non-inductive galvanic distortion leading to a frequency independent parallel shift of the apparent resistivity curves while leaving the phase data unaffected (Jones, 1988; Vozoff, 1991; Fischer et al., 1992; Spitzer, 2001). Static shift effects commonly pose a problem which is difficult to address quantitatively in MT data interpretation. The decomposition methods used in section 5.4 do not remove these shifts. Inversions are therefore emphasised on the less affected phases by assigning higher error bounds on the  $\rho_a$  data. In addition, the used inversion code allows to automatically compute a constant shift of the  $\rho_a$ -curves between the resulting  $\rho_a$  model response and the previous iteration. Prior to computing the next iteration the obtained shift factor is applied to the data. The shift factors between the initial data and

<sup>1</sup>It is an inherent problem of such 2D inversion studies that they have increased degrees of freedom to fit the model's bounding sites. This reduces the reliability of the obtained conductivity structure at the model's edges.

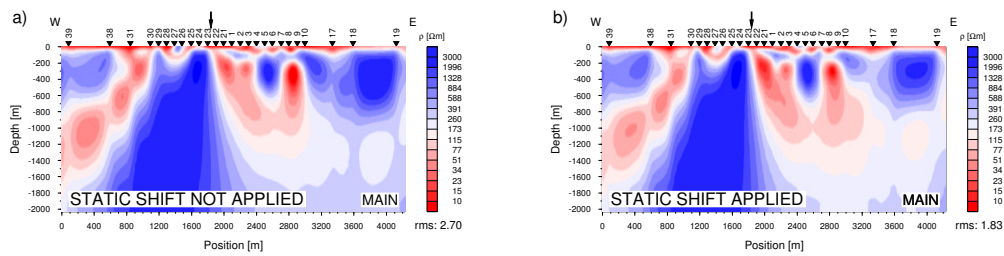


Fig. 5.11: a) Inversion model for the Main profile without consideration of static shift effects. b) Inversion model with automatic computation of static shifts (same as Fig. 5.9).

the model response after completion of the inversion are presented in Fig. 5.10b. Sites without shifts in the  $\rho_a$ -curve have a factor of one. Static shift coefficients are greater one if the original data are shifted to higher resistivities and vice versa.

Static shifting does not cause a severe problem along the investigated profiles. Shifts of  $\rho_a$  are very well handled in the inversion of the Main profile, as can be seen from the low rms errors even at the sites exhibiting larger shifts (e.g. sites 26, 6, 8 and 18). The correspondence of increased shift factors and high rms-misfits at sites 56 and 57 of the South profile in Fig. 5.10b may imply that static shifts are not successfully removed. To test, whether information about the subsurface conductivity structure inherent in the data is wrongly attributed to static shifts during the inversion's automatic shift factor estimation (cf. Brasse et al., 2002), a model without consideration of static shifts was computed. However, there is no substantial difference in the resolution of conductive / non-conductive features and their geometries for the model without automatic consideration of static shifts (Fig. 5.11, left) and the model with their computation (Fig. 5.11, right).

### 5.5.2 Model parameter and sensitivity studies: alternative models

It is important to achieve an understanding of the robustness and resolution of the features described in the previous section. The model results presented in Fig. 5.9 therefore serve as basis for evaluating model parameters (error bounds and starting model) and for empirically testing the sensitivity of the resolved features. The following studies concentrate on the densely surveyed Main profile.

#### Error bounds

The data were given uniform error bounds prior to modelling ( $\rho_a$ : 10% /  $\phi$ : 2°) even though the sounding curves shown in Fig. A1 predominantly exhibit smaller errors. As stated before, assigning error bounds on the one hand serves to down-weight apparent resistivities with respect to phases in order to reduce the influence of possible static shifts and the less well determined  $\rho_a$ -data within the dead band. On the other hand it facilitates assessment of data-to-model misfit because the misfit of sounding curves with increased error level is not governed by irregularities at individual frequencies. To test, whether this assignment of error bounds entails a loss of information, an inversion with the actual data errors has been computed. The result, shown in Fig. 5.12b resolves the same features as the reference model (Fig. 5.12a, identical with Fig. 5.9). The central conductor ① extends to greater depth of  $\sim 1700$  m, while anomaly ⑦ resides closer to the surface.

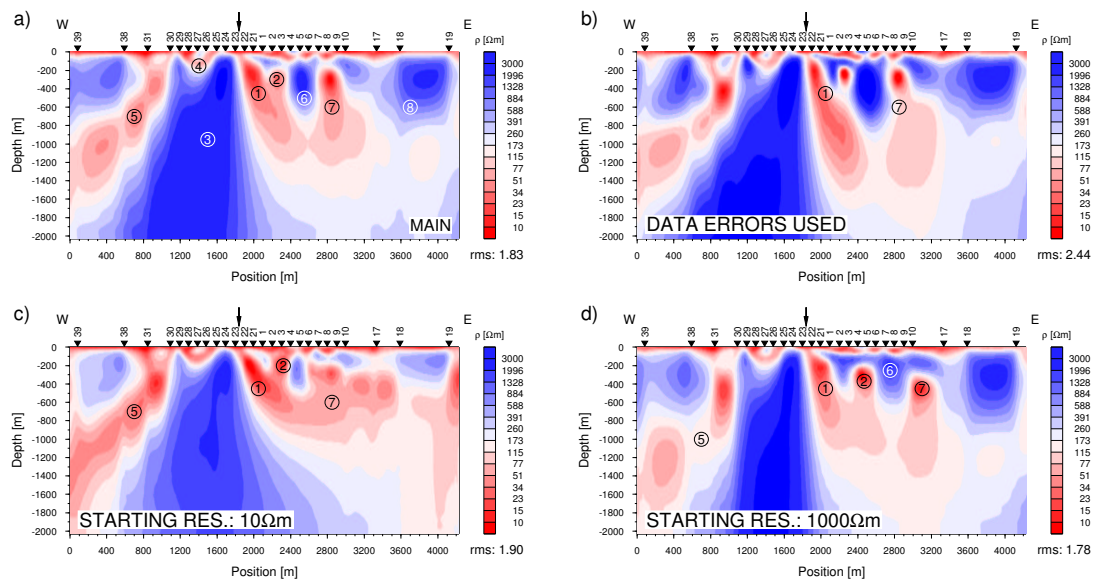


Fig. 5.12: Model parameter and sensitivity studies for the Main profile. Based on the reference model of Fig. 5.9 (reproduced in a) to facilitate comparison) specific parameters are changed (see text for details). The rms misfit for each inversion is given. Models shown without vertical exaggeration.

### Half-space resistivity influence

The resistivity structure of the starting model of an inversion can be freely chosen. Commonly, the starting model is a homogeneous half-space, although more complex structures are possible, too. The effect of varied half-space resistivities of the starting model is inspected in this paragraph.

The inversions presented so far, started with a homogeneous half-space resistivity of  $100 \Omega\text{m}$ . This value is well justified since the bulk apparent resistivity of the sounding curves of all sites averages at  $167 \Omega\text{m}$  within the inverted frequency range, as shown in Fig. 5.13a. Fig. 5.12 shows two inversion results with different half-space resistivities for the starting model, namely  $10 \Omega\text{m}$  (c) and  $1000 \Omega\text{m}$  (d). Usually, a change of the subsurface resistivity implies regridding of the inversion mesh. Here, the mesh of the  $100 \Omega\text{m}$ -model was chosen dense enough, so that regridding for the model variations is not necessary. This allows better comparability of the alternative models. How can the observed differences of models (a), (c) and (d) in Fig. 5.12 be explained? The parameter sensed with electromagnetic sounding is, strictly speaking, the conductance, i.e. the product of conductivity and 'thickness' of a structure. In this context a highly conductive anomaly with small depth extent produces the same signal as a somewhat less conductive anomaly with greater depth extent. Starting the inversion with a conductive environment forces the algorithm to include resistive structures to model the data and the conductive anomalies will remain having smaller dimensions (cf. Fig. 5.12c). In contrast, a resistive starting model where conductive anomalies need to be included, results in deeper reaching conductors (cf. Fig. 5.12d). It is therefore of importance to choose a starting half-space resistivity representing the bulk resistivity of the subsurface. A plot of rms misfit against the half-space resistivities of the different models (Fig. 5.13b) shows better fits for the more resistive variations, although the differences are not distinct.



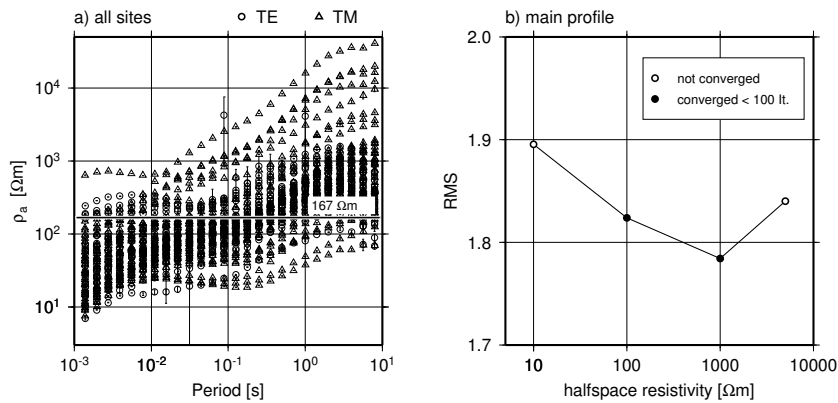


Fig. 5.13: a) Accumulative plot of all recorded  $\rho_a$ -sounding curves of all sites. The mean (bulk) apparent resistivity is  $167 \Omega\text{m}$  (TE-mode:  $144 \Omega\text{m}$ , TM-mode:  $192 \Omega\text{m}$ ; static shifts not taken into account). b) Development of the rms error for inversions with different half-space resistivities of the a priori model.

It is interesting to note that the imaged anomalies east of the central conductor ① are not reproduced as reliable as the other structures. In particular the position of features ②, ⑥ and ⑦ shift to the east in the  $1000 \Omega\text{m}$  model (Fig. 5.12d). The resolution of such individual features will be addressed in the following sections.

### The eastern anomalies (②⑥⑦)

While modelling, it became evident that the geometry of some features, like the conductive anomaly ⑦, is not very well constrained. Feature ⑦ for example shifts to the east between sites 10 and 17 if site 8 is omitted from the inversion (see Fig. 5.14c). The data obviously require a conductive region although its exact position is variable. A possible explanation for this behaviour may be a deviation of the individual electric strike angle of site 8 from the value of  $10^\circ\text{E}$  established for the entire data-set in section 5.4. In particular site 8 causes problems with the electric strike angle determination and yields an angle of about  $35^\circ\text{E}$  when decomposed individually. However, rotating site 8 accordingly causes severe inconsistency of the sounding curves with neighbouring sites, which in turn leads to high rms misfits of the inversion response to the data for the rotated site. Fig. 5.14b shows the inversion result with sites that exhibit strong electric strike deviations being rotated to their respective coordinate system. In comparison to the reference model (Fig. 5.14a) it must be concluded that assigning different electric strike angles for some sites does not alter the inversion response markedly. This can be attributed to the dense site spacing and the associated redundancy of the data.

The  $1000 \Omega\text{m}$ -model of Fig. 5.12d implies that a model solution exists with a resistive structure (⑥) beneath site 8 and the conductor ⑦ shifted further to the east beneath sites 10 and 17. This is similar to the model of Fig. 5.14c where sites 8 and 9 are left out from the inversion. Whereas the number and sequence of resistive (⑥) and conductive (②⑦) anomalies is never changed, their exact localisation remains unclear. Using a starting model with higher conductivity of the subsurface, as for the model in Fig. 5.12c, leads to a conductive block ⑦, that spans the entire range beneath sites 6 to 17. Induction arrows indicate a good conductor located west of site 17 for the high frequency range (see Figs. 5.3a, b), which is consistent with all of the MT model results. A further lateral contrast is

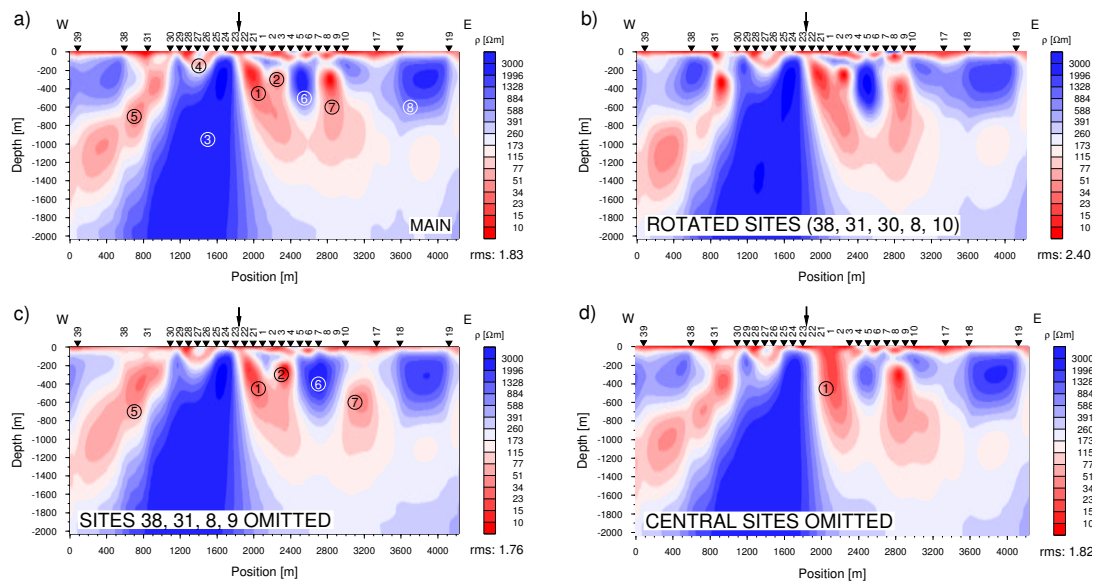


Fig. 5.14: Sensitivity studies for the Main profile. The reference model (Fig. 5.9) is again shown for comparison in a). See Fig. 5.12 for explanations.

not clearly indicated from the GDS data up to site 2, where the westward component and amplitude of the induction arrows increases. That means, that the range from site 2 to site 10 (zone 3 in Fig. 5.3a) exhibits increased conductivity, which is in better agreement with a broad structure ⑦. However, it has to be stated that the position and geometry of conductor ⑦ can not be finally resolved.

The conductive anomaly ② being located beneath sites 2 and 3 may be reflected by the induction arrows in Fig. 5.3a. Its defined position is also supported by the fact, that anomaly ② disappears in a model, in which the central sites are left out from the inversion (Fig. 5.14d).

### The western conductive region ⑤

It was already mentioned in the model description (sect. 5.5.1) that the resolution of the conductive region ⑤, located between sites 39 and 30, is problematic due to the increased site spacing and the anomaly's position at the edge of the model space. Yet it seems to be inclined towards the west. This is still the case, if sites 38 and 31 are not included in the inversion (Fig. 5.14c). The data of site 39 (and 38 if included in the inversion) require a shallow resistive region down to approximately 500 m which is not necessary for site 31. It remains open, whether the conductive regions beneath sites 39 to 30 are really connected to form an inclined conductive zone. However, interpretation of anomaly ⑤ should not be overdone, regarding its position at the model's edge and as well the increased error of misfit of the involved sites (cf. Fig. 5.10a).

### The central conductor ①

The central good conductor ① is a very robust feature in all of the alternative models discussed so far. The necessity of this structure for fitting the data of several central sites of the Main profile is obvious from the ' $\tau = 100$ '-model (Fig. 5.8c). As mentioned above, the high  $\tau$ -value leads to an inversion model which only contains the most dominant structures at the expense of not fitting small-scaled features resolved in the data. In addition, the South profile images a similar structure (Fig. 5.9).

The central conductor extends to a depth greater than one kilometer at both profiles. On this scale the induction-ranges of the closely spaced measurement sites overlap, implying that the central conductor should be imaged by more sites than the ones located directly above it. This is evident from the inversion result shown in Fig. 5.14d that was computed without the central four sites above anomaly ①. The central conductor is nevertheless clearly resolved, but now the information on the dip of the structure is almost lost.

Subsequently, several questions concerning the geometric properties of the central conductor ① of the densely surveyed Main profile will be raised and discussed:

- **Is the eastward dip of the central conductor a robust feature?** None of the shown inversion results, for which a complete set of sites has been used, deviates from a steeply eastward dipping anomaly ①. To test the robustness of this characteristic, the conductivity structure of the reference model (Fig. 5.15a) was modified to represent a vertically trending anomaly with a straight boundary to the resistive block ③ between sites 23 and 22, as shown in Fig. 5.15b. A possibility to evaluate whether such a non-dipping anomaly is consistent with the data (i.e. represents a solution in the model space) is to start an inversion that uses the conductivity structure of Fig. 5.15b as a priori starting model (i.e. instead of a homogeneous half-space). To increase the degrees of freedom in the inversion the western and eastern conductive anomalies have been removed and homogenised with the surrounding resistivity values. The inversion model 1 in Fig. 5.15c shows the result of an unconstrained inversion. This model, as should be expected, is very similar to the reference model in Fig. 5.15a: The central conductor beneath sites 22 and 21 is reduced in its depth extent compared to the a priori model. Beneath sites 1 to 4 a conductive region is added, that extends the shallow conductive part beneath sites 22 and 21 with an eastward dip towards greater depth. In a second inversion run, again starting from the a priori model in Fig. 5.15b, the inversion algorithm is forced to find a smooth solution close to the a priori model that again minimizes the rms error. Fig. 5.15d shows the result after the iterative inversion has converged: The highly conductive ( $\rho < 30 \Omega\text{m}$ ) core beneath sites 22 and 21 is again reduced to shallower depth ( $\sim 500$  m), while the conductivity beneath sites 1 and 2 at a depth between 300-800 m is increased. Although the straight boundaries that limit the conductive center ① are not as clearly removed as in the model of Fig. 5.15c, an eastward inclined highly conductive core is again formed. A dipping characteristic of the central anomaly is thus more in line with the data, than a homogeneously straight anomaly.

Due to the broader site spacing along the South profile a dip of conductive anomaly ⑨ (Fig. 5.9) is not resolved with the used set of inversion parameters. Only if smoothing is almost restricted during the inversion ( $\tau$  set to 0.1) a steep dip to the east vaguely emerges.

- **What minimum depth extent of the central conductor do the data require?** A disadvantage of the magnetotelluric method is that it is not sensitive to resolving the lower boundary of a conductive structure (Jones, 1992; Weidelt, 1985). To achieve an empirical estimate of the minimally required depth extent of the central anomaly ① a series of forward models is calculated. Based on the reference model (Fig. 5.9) the depth extent of the dipping central conductor is modified in each of the forward models, while leaving the surrounding conductivity structures unchanged. Fig. 5.16 plots the resulting rms misfits of each forward solution against the depth in which the central conductor exceeds a resistivity of  $150 \Omega\text{m}$  (i.e. exceeds the bulk apparent resistivity of all measured data; Fig. 5.13). The curve demonstrates that beginning from  $\sim 1100$  m the rms error increases drastically with decreasing

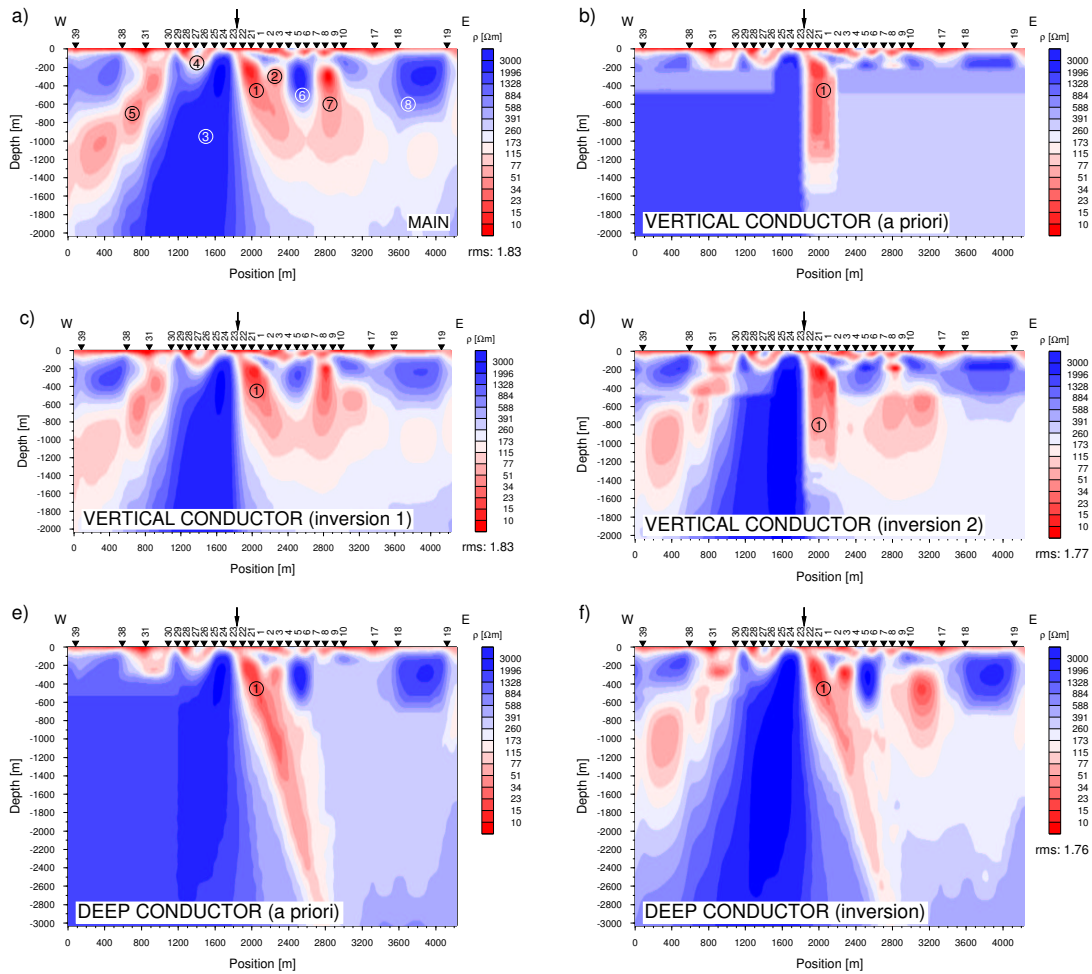


Fig. 5.15: Inversion modelling studies to evaluate the sensitivity of geometrical properties of the central conductive anomaly ① of the Main profile. a) shows the reference model for comparison. b) is the a priori model, which is used as starting model for inversion studies. c) shows the result of an unconstrained inversion, while the inversion result shown in d) is obtained by forcing the inversion algorithm to solve for a smooth variation close to the a priori model in b). e) The depth extent of the inclined conductor is tested using an a priori model with an elongated anomaly ①. Again this model is used as starting model for subsequent inversion shown in f).

depth extent of anomaly ①. This value thus equals the minimal required depth extent of the anomaly in order to satisfyingly fit the data. A deeper reaching central conductor, on the other hand, does not seem to contradict with the measured data. The depth/rms value of the reference inversion result is included in the figure for comparison. Due to the modifications made in the resistivity grid, the rms errors of the forward models are on a higher level than the misfit of the reference inversion model.

Since a deep reaching anomaly can not be excluded from the model solution space, an inversion with a deep anomaly as a priori starting model is computed to check the compatibility of such a model with the data (see above). The starting model is shown in Fig. 5.15e and exhibits a central conductor reaching to a depth of  $\sim 3000$  m. The western and eastern conductive anomalies have again been removed and homogenised with the surrounding resistivity values and the inversion algorithm is set

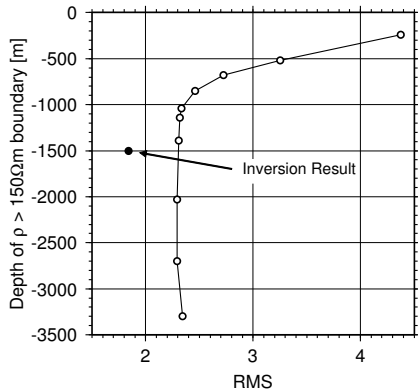


Fig. 5.16: Rms misfit evolution of forward models with modified depth extent of the central main conductor ①. Forward models are based on the reference model. The depth reference is the boundary from which on resistivities exceed  $150 \Omega\text{m}$ .

to solve for a smooth variation away from the a priori model. Figure 5.15f shows the converged inversion result: Anomaly ① remains a conductive feature down to greater depth, but its conductivity is reduced in the lower half of the model. The overall rms misfit is of the order of the reference model misfit. In conclusion, regarding both profiles in Fig. 5.9, a depth extend of about 1500 m remains a satisfying estimate, although the conductor may reach deeper. It should be noted, that in order to resolve structures at depth greater 3 km with similar detail as for the shallow depth range, a much longer profile would be needed with a equally dense site spacing. On a broader scale, however, the individual sounding curves in Fig. A1 of Appx. A.2 do not indicate a change to a layer/zone of increased conductivity down to at least 15 km (i.e. a period  $T$  of 10 s).

• **How wide is the central conductive anomaly?** Finally, the width resolution of anomaly ① shall be discussed. The lateral resolution of the MT survey is limited by the site spacing as well as the electrode spacing perpendicular to the fault trace, which are both 100 m for the central part of the Main profile. Electric fields are deduced from the potential difference between the electrodes, whereas the inversion treats electric fields as point information (see Poll et al., 1989; Jones, 1988). That means, lateral resolution can not be better than the distance between the electrodes. This limitation is acceptable for two reasons: (i) averaging electric fields over that distance also averages small scale inhomogeneities causing static shift; (ii) the regularisation parameter  $\tau$  itself causes a blur on lateral resolution.

Constituting a fixed width is not sensible because the imaged conductivity increase is gradual and not distinct. Using the bulk apparent resistivity of all recorded sites (Fig. 5.13) as a value to bound the anomalies, then the width of the central conductor in the Main profile amounts to around 300 m at a depth of 300 m where the conductivity is highest (cf. Fig. 5.17, the dashed line indicates the bounding value of  $\sim 170 \Omega\text{m}$ ). On the South profile, the central conductor ⑨ exhibits a width of about 800 m. This value most likely overestimates the true width due to the broader site spacing along the South profile. The conductive structure does not necessarily have to be a homogeneous structure of uniform conductivity across its width. For example, a 300 m wide region of densely spaced conductive sheets (lamellae) trending roughly perpendicular to the profile can not be distinguished from a 'solid' conductive block (Pek & Verner, 1997). In section 5.3 it was suggested that such a lamellea-like conductor may be responsible for the fault parallel orientation of induction arrows within the conductive zone 3 of Fig. 5.3b.

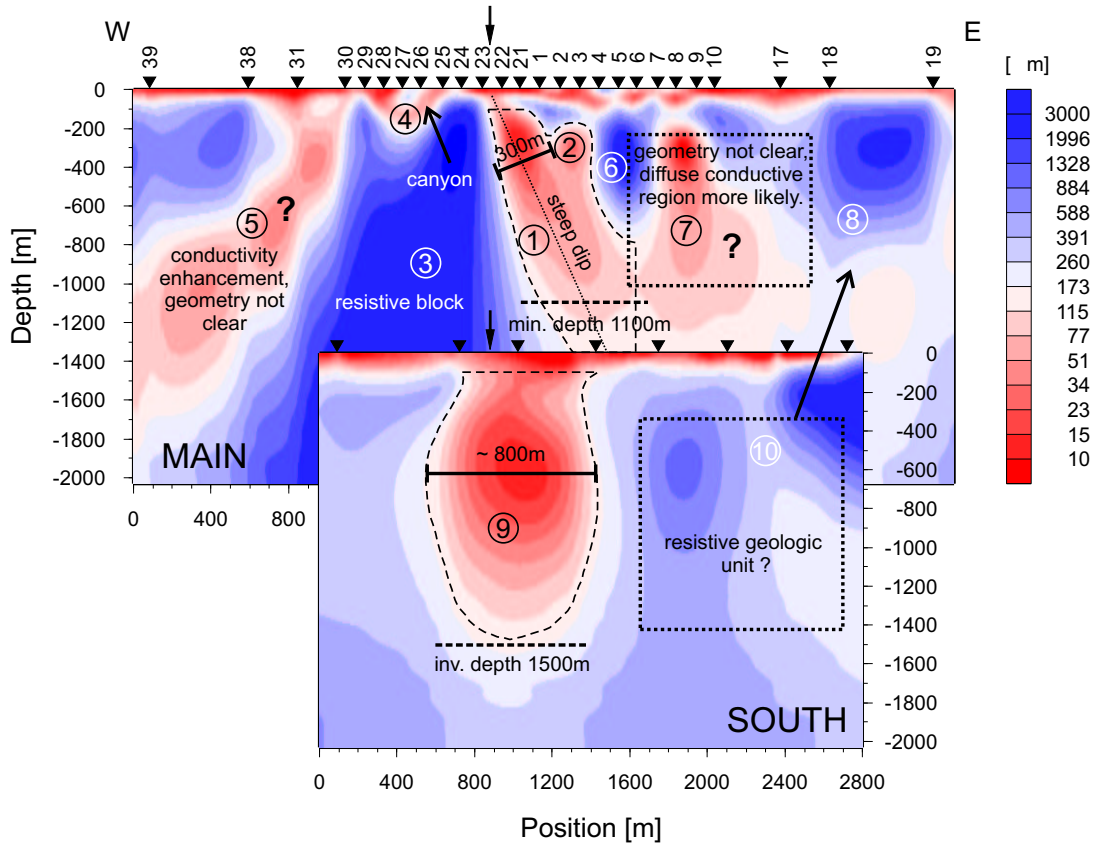


Fig. 5.17: Summary of the magnetotelluric modelling and parameter/sensitivity studies. The models are aligned at the West Fault surface trace (little black arrows) and shown without vertical exaggeration. The long dashed line marks the boundary of the central conductive anomalies (fault zone conductors). The averaged resistivity value for all grid cells ( $10 \times 10$  m) within this region amounts to  $79 \Omega\text{m}$ .

## 5.6 Summary

The main results of the GDS and MT experiments and the modelling of the latter are summarised in the following list (see also Fig. 5.17). In anticipation of the subsequent chapter some correlation with the geological record at the surface is included.

- The dimensionality and directionality analysis justifies an interpretation of the MT data with a two dimensional modelling approximation. Within a frequency range of 1000 Hz to 0.1 Hz the determined electric strike angle is parallel to the strike of deformation structures related to the West Fault. This is supported by the orientation of induction arrows for frequencies below 1 Hz.
- The most robust feature of 2D inversion of the Main and South MT profiles is a conductive structure that lies to the east of the WF surface trace (① and ⑨). A mean resistivity value of  $79 \Omega\text{m}$  results for these structures, calculated within the region marked by the long-dashed lines in Fig. 5.17. This line bounds  $\rho$ -values  $< 167 \Omega\text{m}$  (the average apparent resistivity of all sites; Fig. 5.13). Anomaly ① is  $\sim 300$  m wide and dips steeply ( $\sim 70^\circ$ ) towards the east on the Main profile. Anomaly ⑨ at the South profile is 800 m wide, but note the greater site spacing.

A depth extent of the central conductor of  $\sim 1500$  m is most plausible on both profiles. The conductivity enhancements directly to the east of the WF fault trace are as well resolved with the GDS method. These conductive zones have relatively broad lateral extent (maximum width on the Main profile: 950 m, South profile: 650 m). Due to the close correlation of the central conductors with the fault trace, these anomalies are subsequently called 'fault zone conductor' (FZC).

- The central conductor ① is bounded to the west by a resistive block ③ which can most likely be attributed to lithologically different material west of the WF trace (electrically resistive Jurassic limestones and calcareous pelites / sandstones). This resistive block is interrupted by a shallow U-shaped conductor ④ compatible with a little canyon in this position.
- Further to the west the subsurface conductivity increases again ⑤. The exact geometry is questionable but a westward descending structure may be indicated.
- East of the central conductor follows a series of resistive and conductive blocks. A relatively broad region of enhanced conductivity (broader than structure ⑦) beneath sites 6 to 17 is in agreement with the conductive zones resolved with the high frequency GDS data. Lateral conductivity contrasts are thus probably not as distinct as imaged in the reference MT model, since the GDS result does not exhibit large amplitude geomagnetic effects. A diffuse region of enhanced conductivity is more likely.
- The eastern edges of both profiles exhibit increased resistivities at shallow depth ⑧ and ⑩ and have a very similar appearance. Both profile segments reside in the same geologic unit (Cretaceous andesites and lavas).

## 6 Correlation and discussion

In this chapter, I will pursue the question of whether and to what extent the subsurface electrical conductivity structure obtained from the magnetotelluric experiment (chap.5) is correlated to the fault related structural damage at the surface (chap.4). The correlation and discussion is especially focused on the most robustly imaged electrical conductivity feature, namely the central conductivity anomaly (fault zone conductor: FZC) aligned along the West Fault trace. The cause for this conductor is assessed and implications of the presented studies for the internal architecture of the West Fault segment and the involvement of fluids in the evolution of the fault are presented. The final sections deal with a comparison of the WF studies to similar investigations along the San Andreas Fault system and the predictions on geometric fault properties obtained from fault scaling laws.

### 6.1 Correlation of structural damage and conductivity anomaly

The following sections do not deal with stand-alone topics but are merely intended to subdivide the train of thoughts in the discussion.

#### **Spatial and geometric correspondencies**

The block diagram on the following page (Fig. 6.1) comprises the local geology of the greater Gorila region with the inversion models for the Main and South magnetotelluric profiles together with the results of the structural investigation along the Main profile. The latter are schematically drawn on the front face of the block diagram and represent a downward continuation of the surface deformation (a vertical axes is omitted on purpose).

The central zones of enhanced conductivity on both MT profiles most obviously coincide spatially with the mapped trace of the West Fault<sup>1</sup>. More specifically, the conductive region lies directly to the east of the fault trace and matches the extend of the heavily altered fluid alteration zone, as can be clearly observed for the Main MT profile in Fig. 6.2. Also for the South profile, the highest imaged conductivities result to the east of the WF trace (see Fig. 5.17). Along the Main profile the West Fault surface trace itself seems to correspond to a plane of significant change of conductivity. Highest resistivities are imaged west of the trace beneath the Early Triassic andesitic and Jurassic calcareous series. On the South profile, where the Jurassic and Triassic formations are not exposed, a similarly resistive block is not resolved, accordingly.

---

<sup>1</sup>The West Fault trace is mapped from aerial photographs and is not necessarily always identical with the plane of maximum strike slip displacement. In the Gorila region it is the transition from brittle deformed, though intact andesites to heavily and colorful altered granitoid rocks that produces the most distinct visual contrast across the fault.



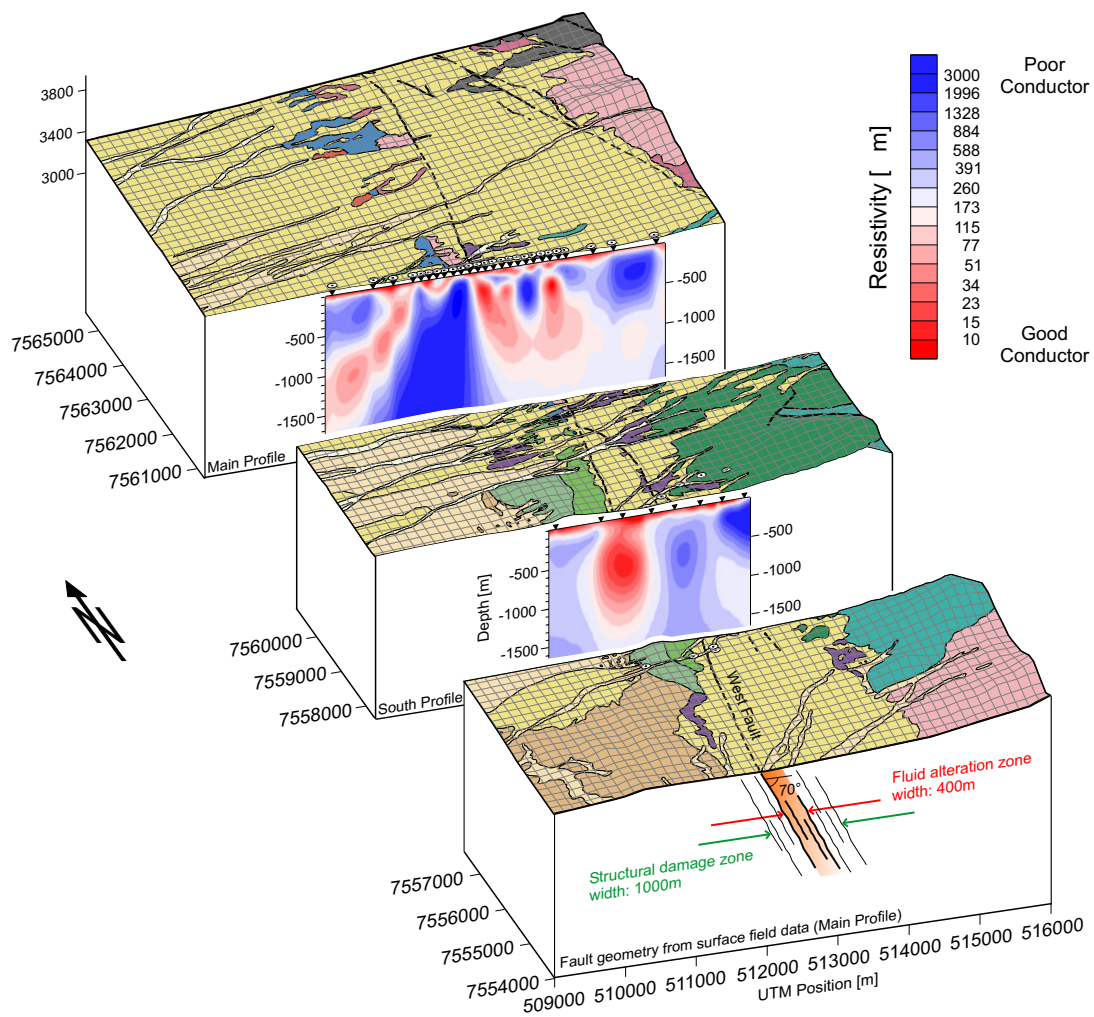


Fig. 6.1: Block diagram with geology (cf. map in Appx. A.4 for legend) summarizing the magnetotelluric inversion models of both profiles and the results of the structural investigation along the Main profile. The latter are schematically drawn on the front panel of the block diagram and extrapolated to greater depth. Magnetotelluric inversion models are not vertically exaggerated. The morphology is exaggerated by factor 2.

The resistive block beneath the Jurassic formation on the Main profile is disrupted by a shallow conductive u-shaped structure (sites 28-25), which is clearly correlated to a little valley and its sediments (see sect. 5.5.1; sites 26 and 27 are located in the valley). Looking at the correlation of deformation element density (cf. sect. 4.1) and conductivity image in Fig. 6.2 it seems as if the eastern rise of densities correlates with a resistive region. It shall be noted, however, that the position of the resistive block beneath sites 4-7 is not as reliably resolved by MT as the fault zone conductor (see sect. 5.5.2).

The dip of minor faults and coloured bands in the alteration zone and its immediate boundaries of the Gorila region is conspicuously similar to the dip of the central conductor at the Main profile, both ranging between  $70^\circ$  and  $80^\circ$  (Figs. 6.1 and 6.2, cf. Photos 7 and 8 in Appx. A.3). This suggests that the electrical conductivity enhancement is causally related to a mesh of faults and fractures. Such a

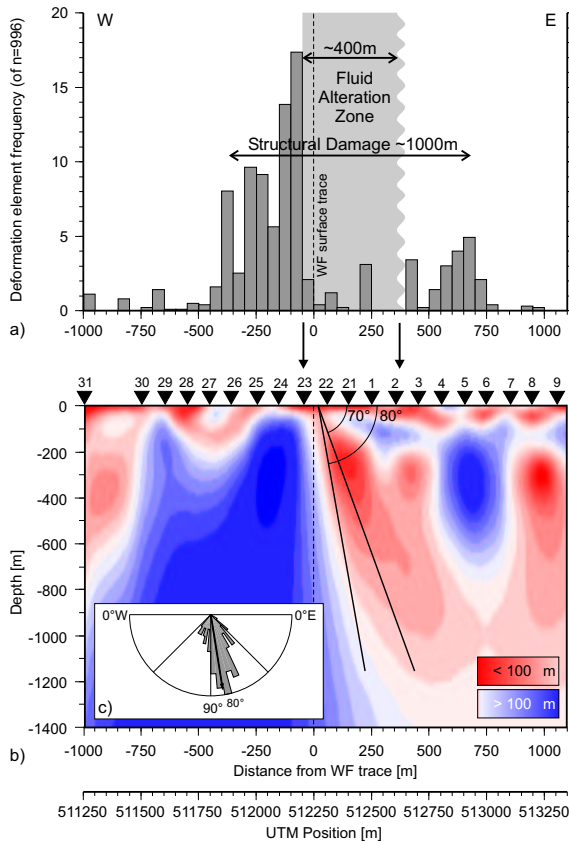


Fig. 6.2: Correlation of fault related damage and subsurface conductivity structure along the Main MT profile. a) Deformation element density profile and alteration zone (see Fig. 4.2a). b) Central part of the inversion result of the Main profile (see Fig. 5.17a). Solid lines mark a dip range from 70° to 80°. c) Dip of minor faults and alteration bands in the vicinity of the WF trace (see Fig. 4.3).

The fluid alteration zone correlates spatially with the dipping zone of enhanced conductivity. The dip of the conductor coincides with the inferred dip of 70-80° towards the east of minor faults surrounding the WF trace (cf. Photo 2 in Appx. A.3). Furthermore, the figures suggest a correlation of brittle deformed (fractured and faulted) rocks outside the intense alteration zone with regions of reduced electrical conductivity.

mesh may serve as pathway for fluid migration (Sibson, 1996). The investigated damage elements in the Gorila region that may contribute to fluid migration are shear fractures and faults, reactivated existing shear planes and to a minor degree pure macroscopic extension fractures (since most of the planes exhibit slicken-lines). In a predominant strike-slip regime, as for the WF (cf. sect. 4.2.1), all of these elements interlink parallel to the subvertically oriented intermediate stress axis  $\sigma_2^1$  and by adding a 'tubular component' this enhances vertical permeability<sup>2</sup> (Sibson, 1996).

In such a fault-fracture mesh a saline fluid may be responsible for elevated electrical conductivity due to electrolytic conduction (and/or surface conduction effects). Fluids may as well transport solutes that precipitate on the mesh surfaces as electronically conductive phase, such as metallic oxide or sulfide ores. Finally, minor (subsidiary) faults often form a gouge as response to shear comminution and geochemical alteration driven by the fluid phase. If such a gouge is composed of or contains clay minerals it may have low electrical resistivity, while generally being impermeable for fluid flow. Is it possible to further delimit the cause for the conductivity enhancement of the West Fault conductor?

<sup>1</sup>The more shear reactivation on existing surfaces governs the deformation, the more  $\sigma_2$  may deviate from strict vertical orientation.

<sup>2</sup>In fact, numerical models of fluid flow in different styles of fault zone architecture by Caine & Forster (1999) have shown that flow in the fault plane and perpendicular to the slip vector (i.e. vertical for strike-slip faults) is slightly higher than flow parallel to the slip vector. However, this anisotropy is relatively small compared to the permeability contrast between undeformed protolith and damage zone.

### The conductive constituent

**Ores:** Metallic mineral oxides or sulfides (all of which are conceivable in copper mining districts) only affect the conductive properties of a rock mass by electronic conduction, if they form an interconnected network or mesh. Dissipated ores are not effective. In that regard, ore coated fracture meshes can very well contribute to increase bulk conductivity. However, ore coatings on slip surfaces were not observed in the Gorila region. Furthermore, XRD analysed samples of fault rocks and alteration zone material did not yield a metallic ore phase in any significant amount (Janssen et al., submitted). This is as well true for the eastward dipping coloured bands in the alteration zone that may represent ancient pathways of fluid flow. A little prospect site for copper ores close to MT station 56 on the South profile (the third from the east in Fig. 6.1) exhibited some accumulation of copper ores. However, except for the usual high conductivity close to the surface, the MT image does not reveal a particular conductivity anomaly in that position. Finally, an interconnected mesh of an electronically conductive phase is difficult to conceive regarding the degree of comminution in the unconsolidated alteration zone, where the most prominent conductivity increase is observed. Electronic conduction is therefore an unlikely candidate for the observed conductivity features.

**Fault gouges:** The resistivity of a clay-rich gouge typically ranges between 3-10  $\Omega\text{m}$  (Palacky, 1987; Eberhart-Phillips et al., 1995). In order to produce the observed fault zone conductor, clayey fault gouges need to be densely distributed within the zone of enhanced conductivity. However, the field record contains no intact gouges within the alteration zone. Minor faults having gouges are very abundant in the Triassic andesites just west of the fault trace (contributing to the high deformation element density in Fig. 6.2) but here, resistivity is high. The fault gouge material that was analysed proved to be dominated by quartz/feldspar or calcite minerals. Although clay-gouge networks can be excluded from causing the observed conductivity structures, even distributed clay can significantly increase the materials conductivity in conjunction with fluids (see below).

**Fluids:** This leaves fluid involvement as the most likely candidate to explain the observed conductivity enhancement. Again a fault and fracture mesh (or the materials pores themselves) needs to be interconnected to allow for electric current flow by ionic conduction. The fluid contained in the rock mass must be sufficiently saline to provide the electrolyte. Besides the fluid-internal conduction, the electrochemical interaction of the fluid with the solid material along surfaces of pores or cracks also contributes to conductivity (Schopper, 1982; Wildenschild et al., 2000). Particularly, water rich alteration products (e.g. clay minerals), which coat deformational surfaces have a significant influence. The involvement of fluids of primary meteoric origin in the alteration zone was outlined in section 4.4 and the spring on the West Fault trace (plus personal experience!) proves that surface water is abundant. In the following, salinity, fluid conductivity and the percentage of permeable (interconnected) porosity shall be estimated to see whether fluids are a reasonable cause for the observed electrical conductivity signature.

### Porosity estimation with Archie's Law

If we know the electrical conductivity of the fluids in the rock material, then the materials porosity can be semi-quantitatively estimated with the help of Archie's empirical law (see below). The primary sampling source for surface water in the Gorila region is the cold spring located on the West Fault

		Sample water source		
		Radomiro Tomic explor. shaft (200 m b.s.l)	Radomiro T. open pit (beneath water table)	Gorila surface spring
Main ions [mg/l]	Cl <sup>-</sup>	7170	1680	60.4
	SO <sub>4</sub> <sup>2-</sup>	<0.5	<0.25	179
	Ca <sup>2+</sup>	647	465	102.2
	Mg <sup>2+</sup>	57.5	42	12.2
	Na <sup>+</sup>	128	69	39.1
	K <sup>+</sup>	4880	1910	10
Equiv. $B$ [mequ/l]		184.83	62.95	6.58
Fluid res. $\rho_f$ [ $\Omega$ m]		0.6 <sup>1</sup>	1.7 <sup>1</sup>	16.7 <sup>2</sup>
With bulk rock resistivity $\rho_r = 79 \Omega$ m and porosity $\Phi^m = \rho_f / \rho_r$ (Archie's law)				
$\Phi$ [%] for $m = 1$		0.8	2.2	21
$\Phi$ [%] for $m = 1.5$		3.9	7.7	35
$\Phi$ [%] for $m = 2$		8.7	14.7	46

<sup>1</sup> for Cl<sup>-</sup> dominated water:  $\rho_f = 1/123 \cdot B^{0.9388}$

<sup>2</sup> for  $1 < B < 10$ :  $\rho_f = 1/B(95.5 - 5.54 \cdot \log B)$

Tab. 6.1: Specific fluid resistivity ( $\rho_f$ ) calculation for several ground water samples from different depth below surface level (b.s.l.). The determinant ion constituents for the physical properties of the water are chosen according to Berkold (1982).  $B$  is the equivalent concentration of electrolyte. Fluid resistivities  $\rho_f$  are calculated from empirical relations described in Berkold (1982). Data for Radomiro Tomic copper mine are taken from Cuadra & Rojas (2001), the spring water was analysed by G. Schettler (GFZ). The average rock resistivity  $\rho_r$  of the central conductors of the Main and South MT profiles is  $79 \Omega$ m (see Fig. 5.17). An interconnected porosity  $\Phi$  – filled with fluids of resistivity  $\rho_f$  – that is minimally needed to explain the bulk resistivity  $\rho_r$  exclusively from the fluid contents can be calculated from Archie's law (e.g. Schopper, 1982).  $m$  is an empirical exponent, which is usually set to one for porosity estimation of fractured rocks. See text for details.

(see map, Appx. A.4). A water sample was analysed for its ionic content (G. Schettler, GFZ), from which the equivalent concentration  $B$  [mequ/l] of the electrolyte<sup>1</sup> and, eventually, the fluid resistivity  $\rho_f$  is calculated (see Tab. 6.1). A resistivity  $\rho_f$  of  $16.7 \Omega$ m results for the spring water.

Cuadra & Rojas (2001) published several water sample analyses from the copper deposit of Radomiro Tomic that lies approximately 15 km to the south of the Gorila region and directly to the east of the West Fault. While prospecting the site, an underground water sample was taken from the ground water level at a depth of 200 m beneath the surface. Further samples were taken, after operation of the open pit mine began, from water draining into the pit. Tab. 6.1 lists the calculated fluid resistivities. Taking these samples to be representative for regional ground waters in the alteration zones, we thus achieve a qualitative salinity-, respectively conductivity - depth profile, with the

<sup>1</sup>Because anion and cation concentrations differ, the average of both has been taken for  $B$  (Berkold, 1982). For comparison: sea water with 30‰ salinity has an equivalent concentration  $B$  of  $\sim 500$  mequ/l and a resistivity of  $0.24 \Omega$ m.

underground water sample representing longest exposure to fluid-rock interactions. Fluid resistivity for this sample is as low as  $0.6 \Omega\text{m}$ . The open pit mine water sample has shorter storage period because the drainage of water into the open pit essentially 'flushes' the groundwater through the rocks. However, the water nevertheless drains from deep subsurface levels (pit depth  $> 200 \text{ m}$ ), causing the high ion content and low fluid resistivity of  $1.7 \Omega\text{m}$ . The spring water is the most juvenile and close to a characteristic meteoric stable isotope signature, as stated in chap. 4.4.

Archie's law, now, relates the measured bulk rock resistivity  $\rho_r$  to the resistivity of the fluid  $\rho_f$  and the porosity  $\Phi$  assuming that only the electrolytic fluid conductivity contributes to the bulk rock conductivity:  $\rho_r = \rho_f \Phi^{-m}$ . This empirically derived law has proved to be extremely useful for rocks at shallow depth and under low temperature conditions (Glover et al., 2000). The exponent  $m$ , typically ranging between  $1 < m < 2.5$ , can not be directly measured in nature.  $m$  is related to electrical tortuosity that represents all »deviations of the true current path from a straight path with constant current density« (Schopper, 1982). In other words,  $m$  is related to the connectivity of the pore space containing the conductive fluid (Glover et al., 2000). A value of  $m = 1$  implies full connectivity, while for  $m > 1$  the connectivity and thus conductivity of the porous medium decreases. Accordingly, experiments show that  $m$  rises with increasing compaction and cementation of the rock mass (Schopper, 1982). Unsworth et al. (1997) suggest that using the lower bound of  $m$  results in more reasonable porosity estimations for fault zones with open crack textures.

Tab. 6.1 summarises the calculated porosity  $\Phi$  needed to explain the averaged bulk rock resistivity  $\rho_r$  of  $79 \Omega\text{m}$  (see sect. 5.6 and Fig. 5.17) for different values of  $m$ ; the lower bound porosities are highlighted. The inferred interconnected porosity is small for the relatively saline waters at depth of the groundwater level. Values range between 0.8 and 7.7 depending on salinity and the  $m$ -exponent. For comparison, a porosity determination on granitic rock samples from the fault core of the Limon Verde branch of the West Fault Zone south of Calama (see Janssen et al., 2002) range between 7-8% compared to the protolith with 0.8-1.5%. For the rather low-saline spring water, with least fluid-rock interaction and direct exposure to precipitation, porosities would need to be high with  $\Phi$  around 21-35%. However, the unconsolidated alteration zone material at the surface certainly exhibits very high porosities. Nevertheless, the porosity estimation has to be interpreted with care, where pore space is not saturated with water<sup>1</sup>. On the other hand, in the above estimations only the fluid intrinsic electrolytic conduction is considered and surface and interface conduction due to electrochemical interaction effects are ignored. Especially the abundance of clay minerals contributes significantly to lowering the bulk resistivity of the material. This is true even for a dispersed clay content of several percent (which might be expected in the alteration zone material), as laboratory experiments of sand-clay mixtures by Wildenschild et al. (2000) have shown. Taking this into consideration, a little amount of clay minerals may decrease the amount of porosity (fluid, salinity) required to explain the observed conductivity structures.

In summary, neither the salinity/conductivity of the waters nor the inferred porosity of the rock mass results in constraints that exclude fluid involvement as candidate for enhancing bulk electrical conductivity. On the contrary, the deeper we probe the more saline the fluid and the less porosity is needed, so inherently compensating for rock compaction due to increasing lithostatic pressure. Fluids

<sup>1</sup>Wetting (not saturating!) the unconsolidated, granular alteration zone material increases its bulk conductivity by up to 4 orders of magnitude (G. Nover, Bonn, pers.comm.).

of meteoric origin that penetrate(d) the intensely damaged and fractured part of the fault zone are sufficient to explain the conductivity enhancement (Fig. 6.3).

### Sealing and cementation of the fault-fracture mesh

A depth extent of the WF's fault zone conductors of around 1500 m was shown to be most plausible for the two MT profiles (section 5.5.2). This would be in agreement with healing and cementation processes that plug the fault-fracture mesh. For the mesh to be effective as permeable conduit for fluids at greater depth it needs to be deformed (seismically or aseismically) to keep the cracks open (e.g. Sibson, 1996). Otherwise, solutes carried in the fluid precipitate in the mesh and may eventually seal fluid pathways<sup>1</sup>. The deposited seal depends mainly on the rock composition, which controls the solute in the fluid phase, and the temperature conditions (e.g. Parry, 1998). Quartz sealed structures are typical at greater depth since the kinetics of dissolution and precipitation of silica is only efficient at temperatures  $>70^{\circ}$  -  $90^{\circ}$ C. Carbonate precipitation occurs at low temperatures  $< \sim 80^{\circ}$ C and consequently shallow depth (e.g. Renard et al., 2000; Labaume et al., 2001). Additionally, calcite solubility decreases with depth due to increasing pressure (see also Parry, 1998). Labaume et al. (2001) have observed such vertical sealing patterns for natural cataclastic fault zones in sandstones, where quartz sealing of the faults was effective at depth greater 3 km, while the faults at shallow depth have remained open and allowed for lateral fluid flow. The geochemical analysis of surface alteration zone samples of the Gorila region, outlined in section 4.4, also indicates low temperature conditions ( $35^{\circ}$  -  $95^{\circ}$ C) and no  $\text{SiO}_2$  dissolution, suggesting that the fault-fracture mesh is/was not sealed at shallow depth. Surface water can penetrate the shallow parts of the fault zone, but permeability reduction due to quartz seals is likely to prevent further vertical flow to greater depth (cf. Fig. 6.3).

The WF conductor is confined to a depth range smaller than 3 km, which may be attributed to an anomalous geothermal gradient that causes  $\text{SiO}_2$  reactions to be effective at lesser depth. However, there is no indication for a geothermal gradient elevated above  $30^{\circ}$ C/km in the vicinity of the study area (Springer & Förster, 1998). More likely, that the long inactivity of the WF segment has provided enough time for plugging the permeability even at shallower depth accompanied by progressive exhumation of the fault system .

Particularly the calcareous Jurassic series in the Gorila region are prone to calcite precipitation. This, together with the generally lower bulk porosity of limestones, may explain the low resistivities observed west of the fault trace at the Main profile. It is thus an illustrative example for the case where not only the textural change of the fault zone material but the juxtaposition of country rocks of different composition and permeability properties are influencing fluid migration. Such a 'juxtaposition' seal probably prevents westward fluid flow across the fault (cf. Fig. 6.3).

Renard et al. (2000) modelled compaction and sealing rates of fault gouge and fracture systems for rocks of either quartz or calcite composition for a depth range between 2 and 9 km. The assumed processes are intergranular pressure solution of fine grained gouge and pressure solution along stylolites in the fault damage zone (no further solutes are transported into the system). These experiments

---

<sup>1</sup>In cyclical fault evolution models, episodic permeability reduction and pore-fluid pressure increase in the fault zone controls the stress needed for Mohr-Coulomb failure and thus the earthquake cycle (e.g. Byerlee, 1990, 1993; Rice, 1992 among many others).

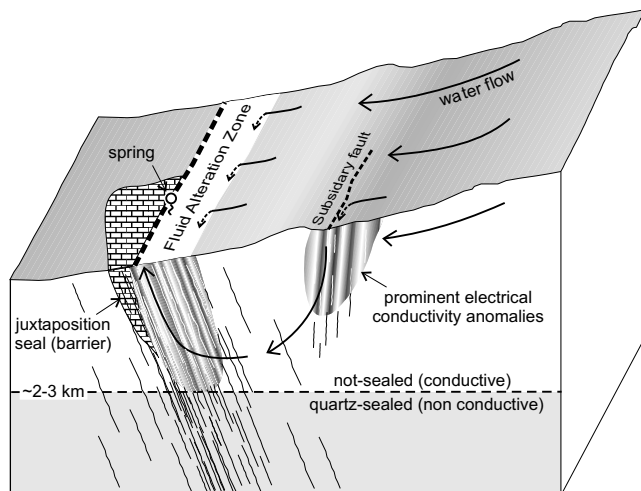


Fig. 6.3: Conceptual sketch showing water inflow into the alteration zone and possible larger subsidiary faults. Electrically conductive anomalies result where permeability in the fault-fracture mesh remains at shallow unsealed depth. Horizontal fluid flow across the fault may be barred by an additional seal resulting from the juxtaposition of rocks with different permeability and healing properties. Waters are forced back to the surface and form springs within the alteration zone.

show that fine grained gouges compact fast within several tens of years compared to open veins and fractures (several hundred to million years; the deeper the higher the sealing rate). For the inactive West Fault segment fine grained gouges should thus not contribute to permeability at all.

On the basis of their experimental results, Renard et al. (2000) suggest that a 'layer' in the crust exists at intermediate depth (4-7 km) for which the characteristics of quartz and calcite sealing cause slower rates of porosity and permeability reduction. For active fault zones it may be possible to image this zone as an anomaly of enhanced electrical conductivity. Such an anomaly, capped by a resistive block, is not published to date. However, conductivity enhancement by this effect may contribute to the deeply reaching conductive anomalies imaged at segments of the San Andreas Fault (e.g. Unsworth et al., 1997, 1999, 2000).

### Lateral fluid migration

The similarity of the conductivity enhancement at the West Fault for the Main and South profile (Fig. 6.1) may suggest that water migration (groundwater flow) is directed parallel to the fault (and the fault slip vector). Additionally, increased electrical conductivity was imaged almost along the entire West Fault segment north of the Radomiro Tomic copper mine in the course of electromagnetic prospecting of the greater Gorila region done by CODELCO<sup>1</sup> (G. Behn, Santiago de Chile, per. comm.). It is difficult to assess whether a horizontal component of flow exists for the West Fault segment. However, considering the morphology of the greater Gorila region, gravity driven penetration of surface waters into the fault zone probably suffices to explain the observed fault parallel electrical conductivity anomaly (cf. Fig. 6.3). In the greater Gorila region water drains (surface and subsurface flow) from the mountain range of the Cerros de Paqui, located to the east, and flows westward towards the fault, following the inclined topography. Reaching the fault, water penetrates into the damage-alteration zone and keeps confined to it. Permeability contrasts and possible seals, e.g. caused by juxtaposition of different rock series (the Jurassic limestones in this special case) restrict further westward flow and may even force the water to flow out in little cold springs located on the fault trace.

<sup>1</sup>The Cooperación Nacional del Cobre (Santiago de Chile, Calama) operates the copper mines of Chuquicamata and Radomiro Tomic.

### **Evolution of West Fault Zone as fluid conduit**

The following description of the West Fault Zone evolution as fluid conduit is based on the data from the well studied copper mines of Chuquicamata, Radomiro Tomic and El Abra in conjunction with the results of this work. First major fluid involvement evidenced for the West Fault system are high-temperature, late magmatic fluids connected with the emplacement of granitoid intrusions around 36-33 Ma (e.g. Ossandón et al., 2001; Camus & Dilles, 2001; compare also Tab. 2.1). These intrusions were controlled by preexisting weaknesses along the Precordilleran Fault System and the West Fault System in particular and were emplaced at relatively shallow depth (between 2 km and less than 4 km for Chuquicamata according to Reutter et al., 1996 and McInnes et al., 1999, respectively). Subsequent hydrothermal mineralisation events, focused in the fractured and brecciated fault zones of high permeability, occurred in several distinguishable pulses (Ossandón et al., 2001; Pemberton, 1997). The last major event in the Chuquicamata complex is dated to ~31 Ma (Ossandón et al., 2001). The authors report that fractures have been opened and mineralized more than once, indicating that hydrothermal alteration was operating intermittently, probably in connection with deformational episodes of the fault system.

Later stage supergene enrichment processes result from the exhumation of the fault system and comprise oxidation and leaching of the hydrothermally mineralized parts within the alternating ground water table and the exposure to surface weathering. Supergene alteration processes only affect the uppermost several hundred meters. For example, at Radomiro Tomic, alteration reaches 200 m into the bedrock, which is overlaid by around 100 m of gravels (Cuadra & Rojas, 2001). Supergene activity ceased at around 14 Ma because climatic change as a consequence of the tectonic uplift caused increasingly arid conditions (Sillitoe & McKee, 1996). The mining districts clearly show that supergene mineralisation by circulation of ground waters has been structurally controlled by fracture permeability of the West Fault System (Lindsay et al., 1995, 1996; Cuadra & Rojas, 2001).

It is worth mentioning here that the copper ore bodies of the Chuquicamata-, Radomiro Tomic- as well as El Abra-deposits are all located to the east of the West Fault trace. At Chuquicamata the copper bearing porphyries are clearly cut off by the fault and there is an economical interest in finding the corresponding western parts. However, where the West Fault dips towards the east, as evidenced for the Gorila region, and supposing an equivalent dip during the hydrothermal and late stage alteration episodes, then circulating fluids likely percolate into the fault-fracture mesh of the hanging wall (i.e. the eastern side). The alteration zones and with them the enriched copper deposits might thus be genetically confined to the eastern side.

The West Fault was still deforming, while supergene alteration was active. Lindsay et al. (1996) even suppose that the large scale sinistral displacement might postdate the supergene mineralisation. Additionally, the exposed late Miocene - Pliocene travertines to the north of the Gorila region might imply another episode of hydrothermal activity (Pardo, 1995; Makshev & Tomlinson, 1995). However, no displacement has been evidenced for the greater Gorila region in Quaternary times.

Although typical supergene alteration products comprise large amounts of clay minerals, like kaolinite and montmorillonite in the case of Radomiro Tomic (Cuadra & Rojas, 2001), the shallow depth extent of such mineralisation makes it impossible to exclusively cause the rather deep fault zone conductors in the Gorila region. The present nature and interplay of fluid regime and electrical



conductivity anomaly is best summarised as follows: Meteoric water driven into the fault zone due to topographic control is the most plausible explanation for the observed conductivity anomalies (see Fig. 6.3). This implies that a fair amount of interconnected porosity must have remained within the alteration zone even after apparent cessation of faulting activity in the Quaternary. The alteration zone presented the locus of fault related deformation and made an increased surface area available for intense alteration processes to be effective. The involvement of the fault-fracture mesh as fluid pathway within the alteration zone, is suggested by the identical dip of deformation elements in the fault's central part and the dip of the fault zone conductor (Fig. 6.2a and b). Infiltration of water is restricted to the upper two kilometers due to likely sealing of the preserved fault-fracture mesh and grain scale porosity at higher temperatures where quartz dissolution and precipitation processes are likely effective. The fault zone conductors, that are imaged along the MT profiles, thus mirror present day fluid penetration into the structurally damaged fault zone and are not directly related to the ore mineralisation processes along the West Fault.

The large scale magnetotelluric profiles that cross the Precordillera and its fault system at latitudes of 20.5° S and 21° S image conductivity enhancements at greater depth of approximately 10-30 km (see Fig. 2.4; Brasse et al., 2002; Lezaeta, 2001). Processes described above are not applicable for enhancing the conductivity in that depth range, although fluid involvement is as well seen as cause for the conductive anomalies (Lezaeta, 2001; Schwalenberg, 2000; Echternacht, 1998). The reasons for the absence of a continuous conductor are speculative. It may be argued, that an impermeable cap at intermediate crustal depth separates shallow from deep fluid circulation systems, both having different sources of fluid, as schematically outlined by Torgersen (1990) and Etheridge et al. (1983). In times of active tectonic or magmatic activity or by hydraulic fracturing due to fluid pressure buildup this cap may break and allow metamorphic fluids to reach the upper crust. Subsequent precipitation of minerals reseals the cap.

### **Internal architecture of the West Fault segment**

The internal architecture of the West Fault segment with its alteration zone differs from the conventional view of brittle fault systems in low porosity rocks. In common models a rather narrow (meter to tens of meter scale) fault core consisting of fault breccia, (ultra-) cataclasite or gouge is surrounded by a wider damage zone with secondary fault related structures (Caine et al., 1996; Caine & Forster, 1999). Porosity and permeability reduction processes in the core typically define it as barrier for fluid flow, while the damage zone exhibits increased fluid permeability compared to fault core and undeformed protolith.

The damage elements of the Gorila region comprise mainly small (subsidiary) faults and slip surfaces (fractures), while mineral filled veins are rare. The frequency distribution of these damage elements (Fig. 4.2 and Fig. 6.2) is rather typical, showing an increasing number with proximity to the fault trace. The difference, now, is that a wide zone up to 400 m with hardly any faults and fractures is not defined by typical fault core material, such as cataclasites, gouge or a series of gouge bands (as in the conceptual model of Faulkner & Rutter, 2001 and Faulkner, 2001), but by intense alteration of the granitoid rocks. The material is strongly comminuted and brecciated and former deformation structures are preserved as coloured bands. Small gouges or cataclasites may be over-

printed by the alteration and thus not preserved. This central part of the fault is electrically conductive for it is sufficiently permeable to allow water entering to a depth of about 1500 m (cf. Fig. 6.3). In Caine et al. (1996) and Caine & Forster (1999) classification of architectural styles and permeability structures this segment of the West Fault is best described as a 'distributed deformation zone', which is characterized by 'well-developed discrete slip surfaces and associated fracture networks', while a well-developed fault core cataclasite is missing. The internal architecture of the WF is the result of long lasting discontinuous activity and multiple reactivation of the fault system with alternating slip sense and the interplay with hydrothermal and surface controlled alteration.

As exemplified by the fault segment exposed in the Chuquicamata copper pit, where a thick gouge of >5 m and a  $\pm 400$  m wide zone of braided shears with montmorillonitic gouge (related to the sinistral displacement episode) is exposed (Ossandón et al., 2001), the characteristics of the fault core change along strike of the fault. However, the Chuquicamata gouge is exposed at a deeper structural level below the surface ( $\sim 500$  m) and it may be possible that similar braided shear/gouge systems are maintained at greater depth for the Gorila region, too.

## 6.2 Comparison with other WFZ segments and San Andreas Fault, California

Many authors have emphasized that structural and fluid flow properties of an evolving large fault system not only vary with time but also in space, in particular along the length of a strike-slip fault (e.g. Evans et al., 1997; Caine et al., 1996). For the West Fault Zone this is evident from comparison of the studies in the Gorila region with structural and magnetotelluric investigations along two profiles crossing the West Fault Zone at latitudes of  $20^{\circ} 55' S$  (Guatacondo Valley) and  $22^{\circ} 40' S$  (Limon Verde; cf. Tauber, 2002), published by Janssen et al. (2002) (see Fig. 2.1a for location of the profiles). Along these fault segments the WFZ is not as clearly confined to an individual branch as in the Gorila region (cf. Fig. 2.1). At both profiles, an alteration zone comparable to the Gorila region is not developed. The fault core is distinguished by an increase in subsidiary fault density above regional levels and the abundance of small-scale cataclastic zones. The analysis of fault patterns on aerial photographs additionally enabled to identify large-scale damage zones from the frequency distribution of faults. On this scale in the order of several tens of meters, damage zone widths of  $\sim 4000$  m and  $\sim 7000$  m result for the Guatacondo and Limon Verde profiles, respectively (Janssen et al., 2002). The large value of the Limon Verde profile is supposed to result from the superposition of damage zones of the West Fault proper and the off-branching Limon Verde Fault. The structural analysis was accompanied with magnetotelluric investigations crossing the zones of highest subsidiary fault density at each profile, with different experimental layouts regarding site spacing and profile length. Electrically conductive zones have been imaged in position of the fault traces, but the depth extent is limited to maximally 200 m (see Tab. 6.2). Sealing and cementation of the fault-fracture mesh and associated permeability has progressed much further on these segments than in the Gorila region.

Tab. 6.2 summarizes the geometric properties of FZC's of the West Fault system together with published data from the San Andreas Fault (SAF), which represents an actively deforming strike-slip fault. Several magnetotelluric investigations with similar experimental layout to the Gorila re-

Property	West Fault System			San Andreas Fault		
	Gorila region <sup>1</sup>	Guatacondo <sup>2</sup>	Limon Verde <sup>2</sup>	Carizo Plain <sup>3</sup>	Parkfield <sup>4</sup>	Hollister <sup>5</sup>
Recent activity	inactive	inactive	inactive	locked since 1857	small earthq., creeping	creeping
Width of FZC	300-400 m	< 100 m	–	< 300 m	600 m	–
Depth of FZC	~ 1500 m	50 m	200 m	~ 3000 m	< 4000 m	~ 8000 m
Conductance	~ 5 S	–	< 5 S	~ 20 S	~ 250 S	~ 600 S
Porosity estim.	~ 1-14%	–	–	> 10-30%	~ 10-30%	~ 10-35%
Cause of low $\rho$	Surface penetration of meteoric fluids			Saline fluids of meteoric origin		

<sup>1</sup> This study. <sup>2</sup> Janssen et al. (2002). <sup>3</sup> Unsworth et al. (1999). <sup>4</sup> Unsworth et al. (1997, 1999, 2000).

<sup>5</sup> Bedrosian et al. (2001, AGU Fall Meeting abstract).

Tab. 6.2: Comparison of high resolution MT studies across the West Fault System and the San Andreas Fault (published data). Recent activity denotes the current state of deformation at the fault segments. The width and depth values of the fault zone conductors (FZC's) are best fitting estimates from the respective modelling studies. The horizontal conductance [S] is the product of width and average conductivity ( $= 1/\rho$ ) of FZC's. Porosities are estimated with Archie's Law using fluid conductivities of water samples (drill hole and spring data) that have been collected in the vicinity of the respective fault segments. The porosity range corresponds to calculations with  $m$ -exponents of one and two. Limits and assumptions of such porosity estimations are outlined in the text. Note that this application of Archie's Law does not account for the electrical conductivity enhancing effects of clays that are likely abundant in fault zones. Porosities should thus be considered as upper bounds. See text for discussion.

gion studies were realised across different segments of the SAF (Unsworth et al., 1997, 1999, 2000; Bedrosian et al., 2001). The Carizo Plain segment is believed to be locked with minimal seismicity since the last 1857 earthquake. Seismic events of  $M \approx 6$  happen on average every 22 years on the Parkfield segment and microseismicity is extensive. The Hollister segment is in a state of active creep. For all these segments a conductive anomaly is imaged in the position of the fault zone, with average resistivities as low as  $3 \Omega\text{m}$  (Parkfield segment; Unsworth et al., 1997). The geometric properties of the fault zone conductors listed in Tab. 6.2 should not be regarded as ultimate values but they represent the most plausible and reliable estimates inferred from modelling the data (see respective publications for details).

For all of the SAF segments hydrogeologic interpretations of the FZC's are favoured. This is supported by seismic tomography studies (Hollister; Chen et al., 1996) and the detection of fault zone guided waves (Parkfield; Li et al., 1997), both evidencing low seismic velocities due to the likely presence of fluids. The  $\delta^{18}\text{O}$  and  $\delta\text{D}$  isotopic signature of waters sampled from thermal / cold springs and wells along the SAF indicate predominantly meteoric fluid origin (Kharaka et al., 1999). Circulation depth of these waters reaches up to 6 km. The depth in which the fluids enter the San Andreas fault zone on the imaged segments is not manifested to date (Unsworth et al., 1999). Comparison of the properties of the different fault zone conductors listed in Tab. 6.2 suggests that the activity of the fault system is correlated to the observed conductivity enhancement, here expressed as the horizontal conductance (product of conductivity and width in [S]). That means, the greater the activity of a fault segment, the more pronounced is the conductivity enhancement. This fits well in the concept of a fault-fracture mesh only being permeable for conductive fluids while it is deformed (Sibson, 1996).

Sealing and cementation of this mesh reduces permeability after cessation of faulting activity (seismical or aseismical): Compared to the presently deforming Parkfield and Hollister segments, the Carizo Plain segment exhibits a conductance an order of magnitude smaller. The conductance of the West Fault segment in the Gorila region, without evident sign of activity in the past million years, is again an order of magnitude smaller. Such comparison is of course limited, since the regional lithologies and their potential fluid dispense is not taken into account. However, the amplitude of the conductive effect of the West Fault in the Gorila region is surprising regarding the historic inactivity of the fault in comparison with the locked Carizo Plain segment.

### 6.3 Fault scaling relationships

#### Fault width to length ratio

Scholz et al. (1993) argued that fault growth is a self-similar process and they predicted several fault scaling relationships based on an elastic-plastic fracture mechanics model. The primary and most intensely studied scaling law relates displacement ( $d$ ) and length ( $l$ ) of a fault. Schlische et al. (1996) have summarized a log-log plot showing  $d/l$  ratio for a fault length range of  $10^{-2}$  to  $10^6$  m and argue that the fault parameters across the entire observed range are most consistently related via a linear scaling law<sup>1</sup>. Based on the mechanical model,  $d$  and  $l$  can be related to width and length of fault process zones or the width of the cataclastic/gouge fault core (Scholz et al., 1993). Here, I will first consider the  $w/l$  ratio, since the fault width estimate for the Gorila WF segment is a result of the presented work. In the next section, the displacement along the segment is included in the discussion.

Similarly to the diagram by Schlische et al. (1996), Vermilye & Scholz (1998) have summarized fault width ( $w$ ) and length ( $l$ ) data pairs from fault studies spanning seven orders of magnitude. This diagram is reproduced in Fig. 6.4 with the following data from this and other published studies added: (i) The West Fault segment presented in this study appears as a single fault branch on aerial photographs compared to the more complex fault zone pattern of the Guatacondo and Limon Verde segments (Janssen et al., 2002). Fault length and width estimates for the West Fault zone used in diagram 6.4 are therefore derived from the Gorila region study. Dilles et al. (1997) reports of 170 km of 'well exposed West Fault'. On landsat satellite images the trace of the WF can be followed for roughly 100 km from Chuquicamata up to  $22.5^\circ$  S without interruption except for stretches where the fault is covered with alluvial debris. The data point is located at an intermediate fault length. (ii) A further large scale fault added to the diagram is the well defined Punchbowl Fault, a parallel branch of the SAF, with a width estimate taken from (Schulz & Evans, 2000). (iii) For the small scale range of the diagram, the laboratory data of fracture process zone width in granites, published by Zang et al. (2000), are included. The resulting  $w/l$  ratio of 0.02 is similar to the value of 0.016 published by Vermilye & Scholz (1998) and lies within the lower bound of the predicted range of 0.01-0.1 (Scholz et al., 1993).

Despite some scatter, the trend of the data shown in Fig. 6.4 may suggest that uniform scaling relations exist over the entire range of observable scales. However, the simplifications of such a rep-

<sup>1</sup> $d = cl^n$  with  $d$  - displacement,  $l$  - length,  $c$  is a constant related to rock properties. For the global data set the best fit curve results in  $c = 0.03$  and  $n = 1.06$ , according to Schlische et al. (1996). The most recent compilation of  $d/l$ -data is published in Schultz & Fossen (2002).

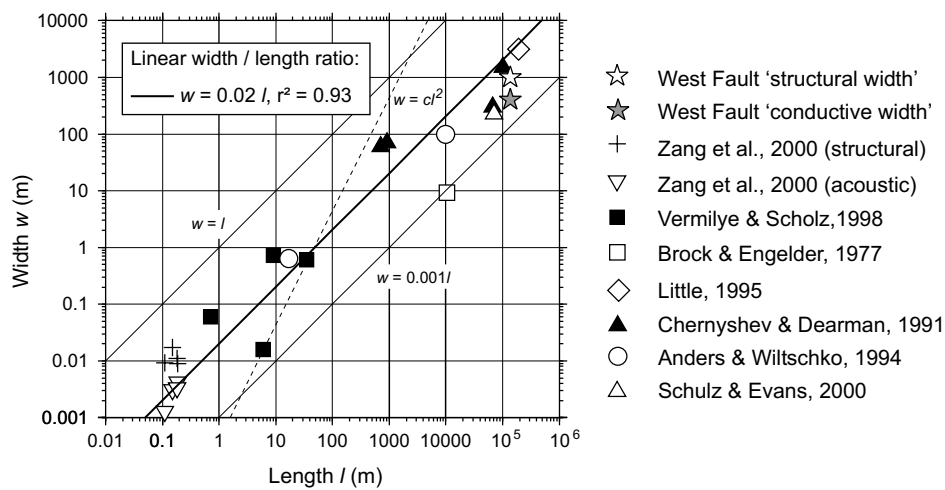


Fig. 6.4: Double-logarithmic plot of fault width versus fault length over a large range of scales. Data are from this study (stars) and additional published research. The linear  $w/l$  ratio is calculated without consideration of the West Fault conductive width value. Also shown for reference are linear curves with  $w/l$  ratios of 1 (upper limit) and 0.001, as well as a curve with exponential  $w/l$  relationship (dashed, exponent of 2).

resentation must be carefully considered: up to date most of the data on geometric properties of faults are from laboratory experiments and small scale (meter-range) natural fault analysis. On the small scale, fault properties such as damage and core zone width, length of the fault and displacement, are relatively well defined and measurable. Additionally, faults can be chosen for investigation that propagated in a more or less isotropic medium. Non of these prerequisites are satisfyingly met for large scale faults greater than several kilometers, in particular the fault or respective fault segment length is difficult to pinpoint. Furthermore, in laboratory experiments the measured fault width is the result of the propagation of the fault tip (fracture process zone; e.g. Vermilye & Scholz, 1998) and the scaling law predicted by Scholz et al. (1993) strictly speaking relates this process zone width to the length of the fault at the time of its tip propagating past the measurement point. For natural faults such a process zone can mostly not be distinguished from the damage zone, that records the entire and accumulated history of slip events, which may comprise reactivation of faults after healing (with probable slip direction reversal), coalescence of fault segments or the interaction of propagating faults. Fault growth models have been modified to account for segmented rupture on a fault and spatial healing and reloading (e.g. Cowie & Shipton, 1998; Cowie & Scholz, 1992b), but the genetic relation of process zone and damage zone of large scale natural faults is not yet established. Little (1995) describes an example, where process and damage zone for a  $> 100$  km long strike-slip fault (Awatere fault in New Zealand) may be discriminated. He relates a broad zone of increased fracturing ( $\sim 3$  km wide) that surrounds a fault damage zone of  $\sim 50$  m to the finite length and finite displacement ( $< 1.5$  km) on the fault. The broad zone was formed during the initial growth of the fault, while softening processes on the evolving or mature fault lead to partitioning of slip and the localisation of displacement in the fault core (see also Wojtal, 1994). Lockner et al. (1991) have evidenced a similar process in the laboratory (using acoustic emission data): The development of a shear fracture evolved from initial distributed brittle deformation to final localisation on the failure plane with accumulating strain.

known parameter(s)	displ. / length scaling		width / displ. scaling scholz93 $w/d = 0.1 - 10$
	schlische96 $d = 0.03l^{1.06}$	scholz93 $d = 0.01l$	
a) WF segment length ( $l$ ) max. 170 km min. 60 km	$d = 10.5$ km $d = 3.5$ km	$d = 1.7$ km $d = 0.6$ km	
b) $w = 1$ km, $d = 35$ km	$l = 529$ km	$l = 3500$ km	$w/d \approx 0.03$
c) $w = 1$ km			$d = 0.1 - 10$ km

schlische96: Schlische et al. (1996), scholz93: Scholz et al. (1993).

Tab. 6.3: Application of fault scaling laws involving displacement to the geometric fault zone properties of the West Fault segment in the Gorila region. Different geometric parameters are assumed to be known (cases a-c) and the corresponding parameter is calculated using the respective scaling law. Two laws are used for the displ. ( $d$ ) / length ( $l$ ) ratio: the best fit estimate for published fault zones by Schlische et al. (1996) and the observed value by Scholz et al. (1993). Fault width  $w$  to displacement  $d$  is the inferred range published in Scholz et al. (1993). See text for explanation.

As Schulz & Evans (1998, 2000) pointed out, »the width of a fault zone is a function of the type of measurement that is used to define it«. This is well demonstrated for the investigations of the West Fault Zone. Where very large scale investigation of faulting pattern is possible, e.g. with the help of aerial photographs (see Janssen et al., 2002), rather broad fault related damage zones of several kilometers width are distinguishable (e.g. about 4 km for the Guatacondo segment). The study on the mesoscopic outcrop scale in the Gorila region revealed increased damage element density for approximately 1000 m across the fault. The width of the fault derived from electromagnetic imaging, again, results in values of less than  $< 500$  m (denoted as grey star in Fig. 6.4). It may be possible, that the width estimates of the electrically conductive fault zone anomalies are closer related to the latest deformation events, which have caused the fault-fracture mesh to be permeable for conductive fluids. Fractures further away from the fault may be sealed and thus restrict fluid flow and associated electrical conductivity effects. Fault and fracture lineations on aerial photographs, beyond that, are still visible when the fault has long ago ceased activity and fractures are sealed and ineffective as fluid and electric current conduit. From this point of view, the different scale investigation methods (aerial  $\rightarrow$  outcrop  $\rightarrow$  electrical conductivity) also sample over different time scales, with the remote sensing method averaging over the longest time span of the faults' evolution.

### Fault displacement scaling

In the above discussion of the fault  $w/l$ -ratio, the displacement of the West Fault segment has not been considered. Tomlinson & Blanco (1997b) and Dilles et al. (1997) describe  $\sim 35$  km of sinistral displacement since the Eocene and another  $0.5 \pm 0.5$  km of dextral displacement since late Miocene/Pliocene times (cf. 2.1). These estimates are inferred from correlation of tectonic units along the  $\sim 60$  km long West Fault segment between the copper mines of Chuquicamata and El Abra. A minimum length of the WF segment is therefore 60 km, the maximum traceable length according to Dilles et al. (1997) is 170 km. These two values are taken as bounds for the investigated WF segment and, together with the other geometric properties of the West Fault, are compared with the predictions

from common scaling laws. The results are shown in Tab. 6.3 for three cases (a-c) in which different parameters are assumed to be known. The used scaling laws are taken from Schlische et al. (1996, see above) and Scholz et al. (1993). The predictions from Scholz et al. (1993) are based on their fracture model. Note that the rather broad range of the width ( $w$ ) to displacement ( $d$ ) ratio inherits the problem of distinguishing process zone from damage zone for large faults, as described in the previous section. Furthermore, the above outlined complications concerning fault length to width ratios are the same for scaling laws involving the fault displacement.

For case (a) in Tab. 6.3 the length of the West Fault segment is given and displacements are calculated from the respective scaling laws. The resulting  $d$  ranges between 10.5 - 0.6 km, which can not be brought to agreement with the mapped 35 km of displacement. Using displacement  $d$  as constraint (case b) a fault length between 500 and 3500 km results which is on the scale of the entire > 2000 km long Precordilleran Fault System. On the other hand, the  $w/d$  ratio of  $\sim 0.03$  for case (b) is an order of magnitude smaller than the lower bound of the range of 0.1-10 published by Scholz et al. (1993). A greater damage zone width would be expected according to this range. A displacement in the range of 100 m to 10 km would be in agreement with the damage zone width of 1 km (case c). This displacement is of the order of the young dextral movements of  $0.5 \pm 0.5$  km on the West Fault.

The discrepancy between fault width/length and displacement on the WF segment may have two possible implications: (i) A considerable amount of displacement must be partitioned to parallel fault segments, which all have developed an individual damage zone. According to field mapping this is very unlikely for the region between the Chuquicamata and El Abra copper mines. (ii) Displacement is episodic and fault growth can not be approximated with an equivalence-model where displacement results from a quasi-continuous event along the entire fault length (Cowie & Scholz, 1992c). The latter is, of course, plausible and modified models consider healing and reloading of the fault (e.g. Cowie & Shipton, 1998; Cowie, 1998). The fault width  $w$  in these modified models relates to the largest slip event on the fault. This eventually implies a smaller displacement estimate for case b) in Tab. 6.3 and consequently a  $w/d$  ratio closer to the inferred range of Scholz et al. (1993). Additionally, fault healing might not restore the initial strength of the fault but allow for processes of strain softening which leads to localisation of process zones of later slip stages on the fault's central parts, as delineated in the previous section. The overprinting of process/damage zones can ultimately lead to the formation of a cataclastic fault core (Scholz et al., 1993; Vermilye & Scholz, 1998). If these processes are generally applicable to large-scale and long-lived fault zones, it may be expected, that fault width to length scaling reaches a plateau for the upper scale end of Fig. 6.4.

## 6.4 Conclusion

Surface and subsurface characteristics of a segment of the West Fault have been studied in this thesis using two different methods of investigation: outcrop based structural geology studies and magnetotelluric surveying. The findings of the respective methods show strong correlation. Several points, regarding the posed questions in the introduction, shall be emphasised below.

- The fault-related brittle damage elements of the West Fault segment in the studied Gorila region record prevalent strike-slip deformation on subvertically oriented shear planes. Reactivation of the fault is evident. Dextral and sinistral slip events within the fault zone can be confirmed, whereupon dextral kinematics apparently dominate.
- Damage element density is increased around the fault over a width of about 1000 m. A zone of profound alteration and comminution of rocks forms the central part of about 400 m width.
- The dimensionality analysis of the MT data justifies a two dimensional modelling approximation of the data in the frequency range from 1000 Hz to 0.01 Hz. A regional geoelectric strike approximately parallel to the West Fault strike of N10°E is indicated for this frequency range.
- A fault zone conductor is imaged on both MT profiles. Induction arrows (GDS) indicate its expansion parallel to the West Fault. The zones of enhanced conductivity are located to the east of the fault's surface trace and coincide in position with the alteration zone.
- The fault zone conductor and the damage elements of the fault's central part both exhibit steep eastward dip (70-80°). This suggests, together with the spatial correlation of the fault zone conductor and the alteration zone, that the electrical conductivity enhancement is causally related to a mesh of minor faults and fractures. This mesh is a likely pathway for fluids.
- The (interconnected) rock-porosity that is necessary to explain the observed conductivity enhancement by means of fluids, is estimated using the salinity of several ground water samples (Archie's Law). The results indicate that fluids penetrating the damaged fault zone from the surface are sufficient to explain the conductivity anomalies. This is supported by the preserved geochemical signature of rock samples from the alteration zone. The analysis reveals that late stage alteration processes were active in a low temperature regime (<95°C) and does not indicate the involvement of fluids from deeply rooted sources.
- The modelling of the MT data results in a depth extent of the fault zone conductor of at least 1100 m and indicates less than 2000 m vertical extent. Dissolution and precipitation of minerals at greater depth and increased temperature may lead to sealing of the fault/fracture mesh, assuming a conventional geothermal gradient and the kinetics of crack-sealing of silica.
- Comparison of the results of the West Fault with published studies on the electrical conductivity structure of the actively deforming San Andreas Fault, suggests that the depth extent and conductivity of a fault zone conductor may be correlated to the recent fault activity. Ongoing deformation will keep the fault/fracture mesh permeable for fluids and impede cementation and sealing of fluid-pathways.
- The width estimate of the damage zone around the West Fault depends on the method applied: a) imaging of the 'conductive width' (~300 m), b) investigation of damage element density



on outcrop scale ( $\sim 1000$  m) and c) investigation of fault lineation density on regional scale (remote sensing of Guatacondo segment of WFZ;  $\sim 4000$  m). The scale increases, on which fault related damage is sampled, with each method listed. Also, the time interval of fault evolution, that is preserved on the respective scales, increases. Due to the complexity of large, long-lived fault zones and the difficulties in assigning unique values to either fault length or fault width, the application of fault scaling laws to large-scale faults must be treated with care.

Investigations of the kind presented here always represent case studies for a specific geodynamic environment. More examples of large-scale fault systems need to be studied and compared among each other to work out common characteristics and fundamental differences. As this work shows, a complex displacement history of a fault makes it difficult to relate deformational events to distinct episodes of fault evolution. Faults to be investigated should therefore ideally have a simple displacement history. The magnetotelluric method for investigating upper crustal electrical anomalies connected to fault zones proved to be very suitable. To achieve an increased resolution of the depth extent of the conductivity anomalies, longer but similarly dense MT profiles are needed. This will likely lead to an increased dimensional complexity of the resolved features and would make the application of 3D modelling techniques necessary. Since the electrical conductivity structure of a fault zone is likely connected to its recent activity, monitoring of electrical properties of fault zone conductors of active faults may be promising to understand the relation between conductivity enhancement or reduction and fault activity.

# Appendix

## A.1 Methods applied for paleo-strain / stress reconstruction

The methods applied for fault striae analysis are primarily based on a program package written by Sperner et al. (1993; see also Sperner & Ratschbacher, 1994; Sperner, 1996). The principles and assumptions underlying each of these methods are briefly described in the paragraphs below. Pros and cons of the different methods are thoroughly discussed in the above listed publications.

### P-T axes calculation (TURNER)

This method for determining shortening (P) and extension (T) axes was originally developed by Turner (1953) for stress analysis from calcite lamellae. In its application for fault striae analysis theoretical P- and T-axes are calculated for each fault-slip datum. It is assumed that the P- and T-axes lie within the plane that contains the fault plane normal and the slicken-line. The sense of slip is crucial for this method, since it defines the position of the P-axes (and T-axes) in relation to the fault plane. The angle  $\Theta$  between the shortening axes and the fault plane (or lineation) is a matter of interpretation:  $\Theta$  is a material property and related to the coefficient of friction  $\mu_f$  by the equation:  $\Theta = 45^\circ - 0.5 \arctan \mu_f$ . A good general estimate for  $\Theta$  is  $30^\circ$ , based on experimental studies (Sperner, 1996). Natural fault observations, however, imply great variability of this value. For the P-T method, a constant  $\Theta$ -value is applied for the entire set of fault slip data<sup>1</sup>. Principal shortening and extension axes are then derived from density contouring the individual P- and T-axes or from calculation of vector means. Concentrations of P- and T-axes, finally, are interpreted as the orientations of  $\sigma_1$  and  $\sigma_3$ .

The individual poles of P- and T-axes corresponding to each fault-slip datum are plotted in Fig. 4.6 to demonstrate their distribution around the calculated vector means. Vector means, of course, are only reasonable if P- and T-axes are distributed in clusters and not in girdles along a great circle. For the strike slip kinematics observed in the Gorila region clustering of both P- and T-axes is most often obtained.

Theoretically, the P-T method is only valid for newly formed slip surfaces for which the assumption that P- and T-axes lie in the normal plane to the fault containing the lineation is met. The pre-

---

<sup>1</sup>If the angle  $\Theta$  is set to  $45^\circ$ , the method is essentially equivalent to the construction of a fault plane solution as familiar to seismologists. The derived P- and T-axes bisect the orthogonal nodal planes, one of which is the fault plane. This defines compressional and dilational quadrants. Marrett & Allmendinger (1990) emphasise that this is simply a different representation of data and does not involve interpretation. Superposing the compressional and dilational quadrants of all individual fault-slip data in a stereonet may define the orientation of the bulk P- and T-axes ('right dihedral method' by Angelier & Mechler 1977).

existence of slip surfaces can alter this assumption. However, results obtained with the P-T method from larger populations are usually very well comparable with other methods.

The angle  $\Theta$ , that is needed for the P-T method can be constrained using the additional program KINEMAT by Michel (1993, 1994). This program determines a value of  $\Theta$  that most tightly clusters the orientation of all of the P-axes (or T-axes) that correspond to each individual fault-slip datum. The obtained value can subsequently be used in the P-T axes analysis described above or for the NDA method (see below). In the case of plane strain strike-slip kinematics the clustering characteristics of both shortening and extension axes can be optimized. Contrary, in a case of radial extension, for example, only the P-axes define a cluster. The clustering statistics also help to separate data into populations exhibiting a common P- or / and T-axes orientation.

### Numerical dynamic analysis (NDA)

This method is an extension to the P-T-axes analysis based on Spang (1972). A reduced stress tensor with shortening ( $P = \sigma_1$ ), extension ( $T = \sigma_3$ ) and intermediate ( $B = \sigma_2$ ) axes is calculated for each fault-slip datum: The orientation of the principal axes is derived equivalently to the Turner method described above, while their relative magnitudes are based on arbitrarily setting the shear stress on each plane to one. Summation of all individual tensors and division by the number of fault-slip data results in a bulk stress tensor. The principal axes of this tensor are obtained from an eigenvalue analysis. Additionally, we obtain the stress ratio or strain factor  $R$ , which is the ratio of magnitudes of the principal axes of the reduced stress tensor:  $R = \frac{\sigma_2 - \sigma_3}{\sigma_1 - \sigma_3}$  (Etchecopar et al., 1981). Together with the orientation of the principle axes, the stress ratio denotes the stress regime. If faults are formed in pure normal, thrust or strike-slip regimes  $R$  is close to 0.5. It deviates from 0.5 the greater the transpressive or transtensive component is.

The measured displacement direction for each fault can be checked for consistency with the slip sense resulting from the calculated bulk tensor. Using Bott's (1959) equation we can calculate the predicted direction of maximum shear stress on a given fault plane that corresponds to the bulk tensor and the respective stress ratio  $R$ . This predicted orientation is then compared to the measured slip orientation. The mean angular deviation of the measured slip direction of each fault from the orientation of the calculated maximum shear stress is expressed as fluctuation  $F[^\circ]$ , which ideally should be zero. The values of  $R$  and  $F$  are given in Fig. 4.6.

### Direct inversion (INVERS)

The above mentioned Bott-equation for determination of the direction of maximum shear stress on a *given* fault plane within a defined stress field, is the basis for direct inversion of fault slip data. The pre-existence of weaknesses (fractures, that might develop during the tectonic event; preexisting slip-surfaces; bedding planes) is an implicit requirement for this method. The direct inversion applied in this work (INVERS) is based on an algorithm by Angelier & Goguel (1979). A reduced stress tensor is calculated by minimizing the least square misfit between the calculated orientation of the maximum shear stress and the measured direction of the striation for all data. The eigenvectors and eigenvalues of the tensor define the principal stress directions and the stress ratio  $R$ , respectively. The angle  $\Theta$  and the sense of slip is not required. Again, the slip sense is subsequently tested against the predictions from the obtained stress tensor and the fit is expressed with the fluctuation value  $F$ .

Since the determination of a reduced stress tensor requires to solve for 4 unknowns ( $\sigma_1, \sigma_2, \sigma_3, R$ ) a homogeneously distributed fault slip data set (of at least four data) is required. The method fails for sets with a marked dominance of one fault orientation or for sets of conjugate faults. The presence of extreme data outliers ('data discrepant with respect to the majority of the measurements'; Sperner 1996) can as well lead to unreasonable results.

### **Conclusion**

The analysed fault slip data of the Gorila region exhibit strong dominance of certain fault orientations (cf. Fig. 4.1), which is expected if the West Fault system experienced several reversals of slip direction. That makes the NDA and P-T axes method in most cases more suitable than the INVERS method. Although the NDA and TURNER methods are theoretically restricted to newly formed faults, the averaging over larger populations accounts for deviations from the prerequisite, that the shortening and extension axes lie in a plane that contains the striation and the fault plane normal. In contrast to that, the direct inversion is theoretically not applicable if more than one deformational phase is involved in the data (Etchecopar et al., 1981). By choosing angles of  $\Theta$  that exceed a value of  $30^\circ$  it can be accounted for fault weakness due to preexisting slip surfaces. The NDA method additionally allows to check whether the resultant bulk (reduced) stress tensor is reasonable for each of the faults in the analysed population. Thus, most of the kinematic results of this work are based on the NDA method.

## A.2 Magnetotelluric data and model response

### Impedance curves

The following three pages (Fig. A1) show the measured apparent resistivity  $\rho_a$  and phase  $\phi$  curves versus period  $T (= 1/f)$  for all sites, starting with the Main profile and followed by the South profile. Sites are enlisted from west to east, little maps give the relative site locations. Circles denote TE mode data and triangles TM mode data. 'ss' signifies single site processing, 'rr' remote reference processing for certain frequency ranges with the specified site(s).

The inversion model response of the models shown in Fig. 5.9 of section 5.5 are superposed as solid lines. Note, that only the period range from  $10^{-3}$  s to 10 s was subjected to inversion.

### Pseudo-sections

Pseudo-sections represent apparent resistivity  $\rho_a$  or phase  $\phi$  data for the complete profile versus a vertical period  $T$  axis. Resistivity or phase values are interpolated between sites for each period. Lowest period (highest frequency) data are equivalent to small penetration depth of the electromagnetic signal. Fig. A2 shows pseudo-sections for the Main profile, Fig. A3 presents pseudo-sections for the South profile. In each figure, the left diagrams represent original data; the model response is shown on the right. The upper two rows show TE mode pseudo-sections, the bottom two rows TM mode. Black dots denote the individual frequencies that have been used for the inversion at the corresponding site. The white stripes in the sections result from marginal sites having greater distance from each other than the chosen width for interpolating the data.

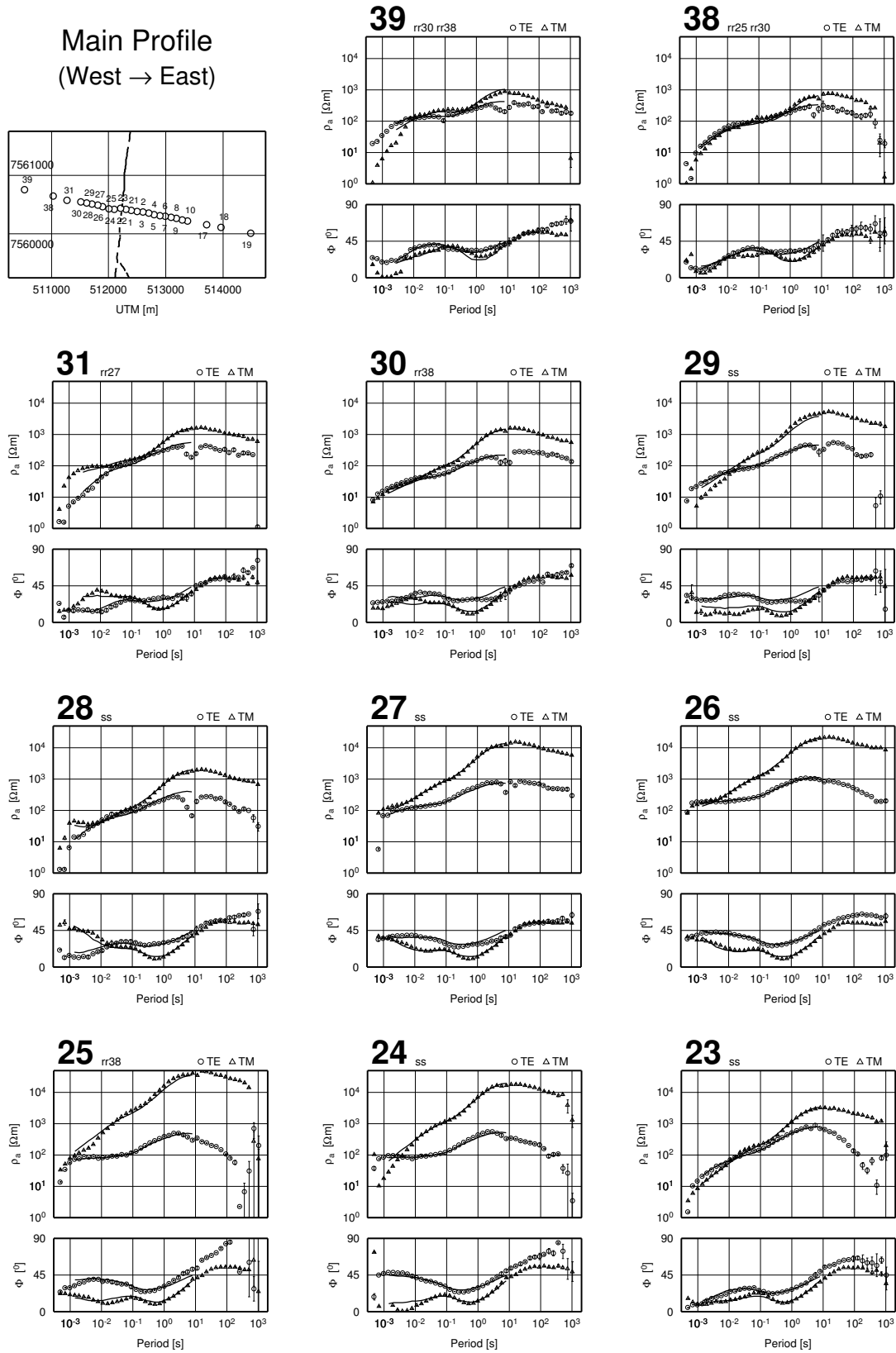


Fig. A1: Station by station representation of apparent resistivity- and phase data fit. See explanatory text at beginning of section.

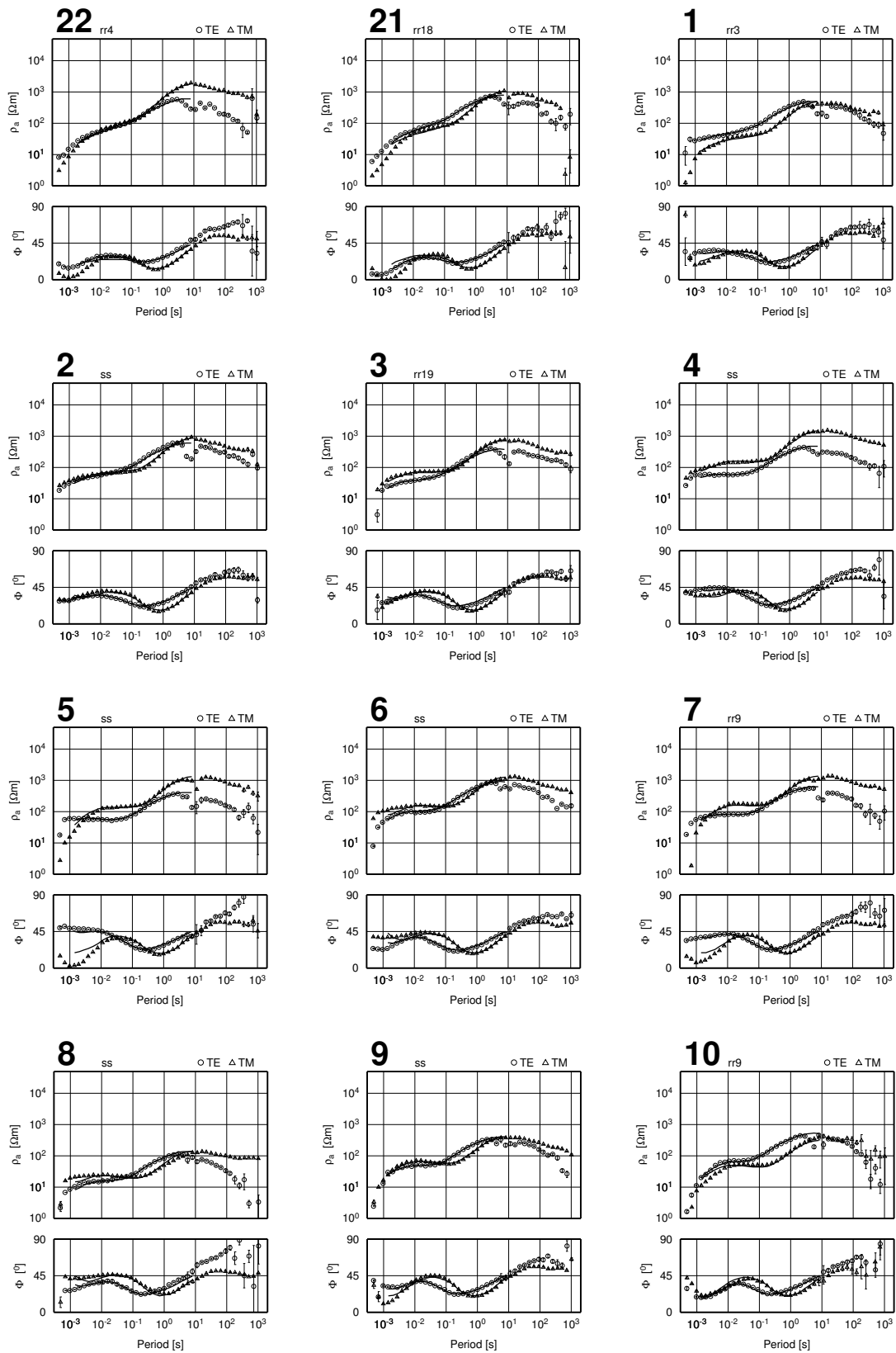


Fig. A1: Continued from previous page.

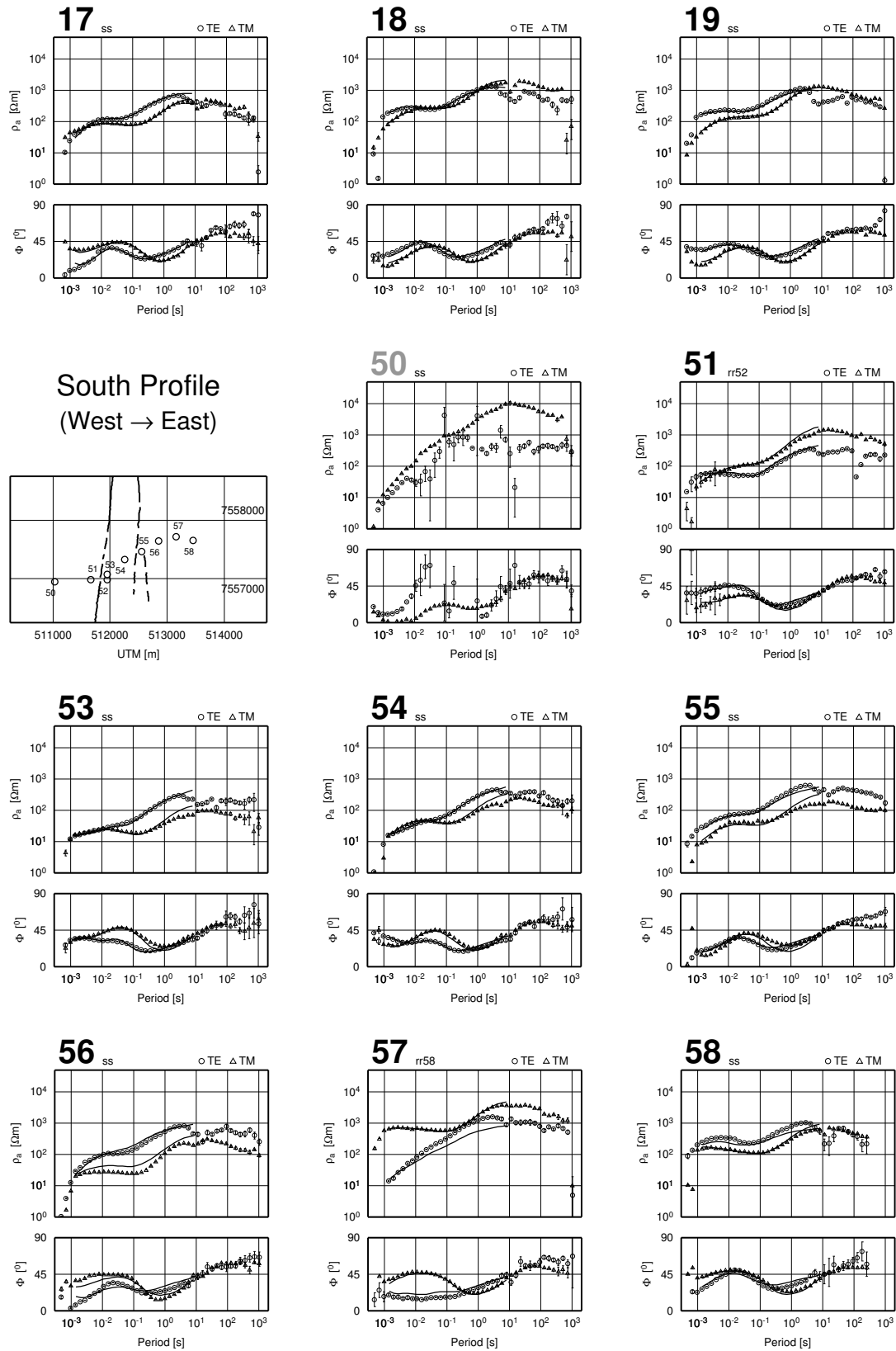


Fig. A1: Continued from previous page. Site 50 has bad quality and only few frequencies were used to give some resistivity constraint on the western boundary of the inversion models.



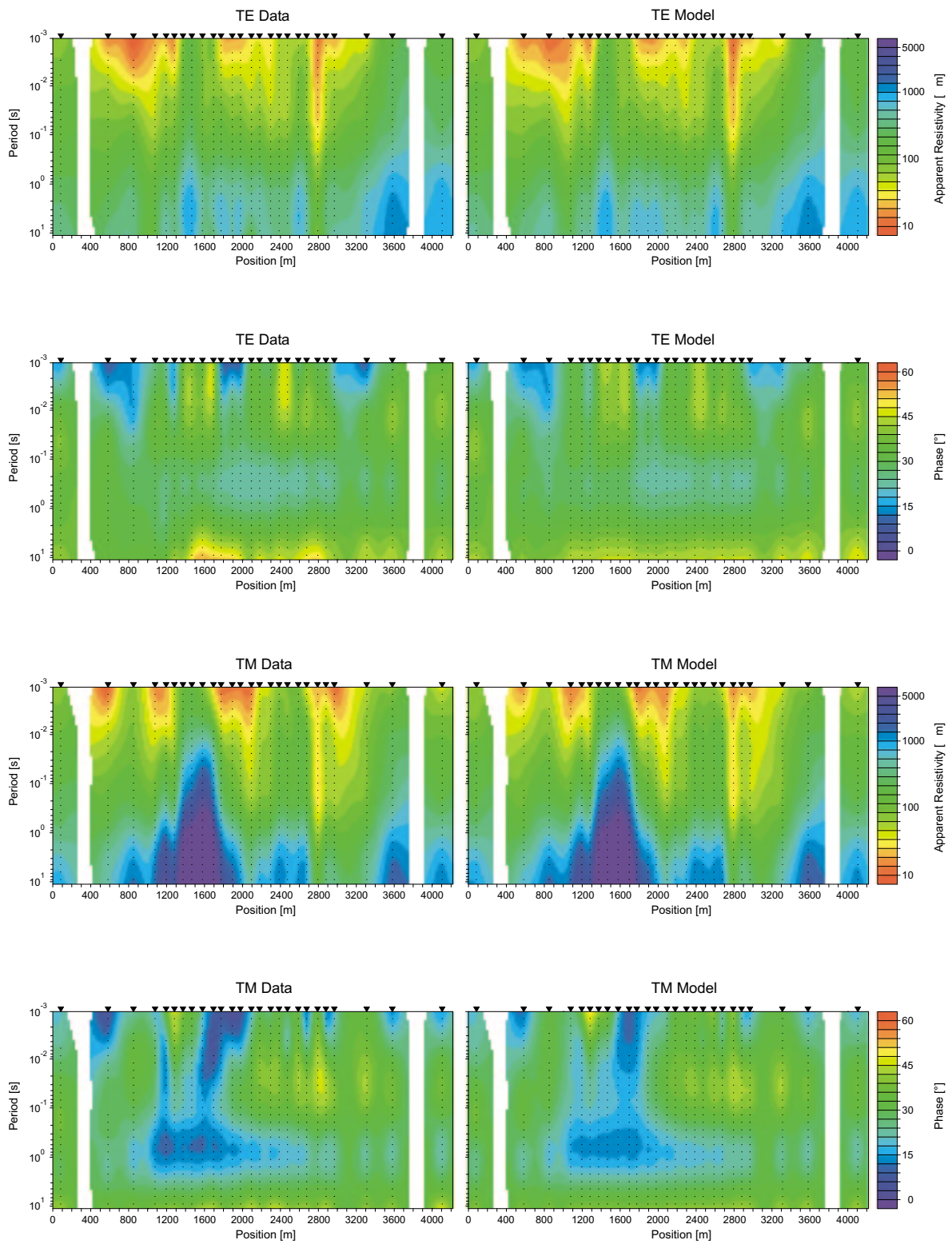


Fig. A2: Apparent resistivity and phase pseudosections for the Main profile. The upper two rows are TE mode, the lower two rows TM mode sections. The left hand side shows data, the right hand side model response. Little black dots mark the frequencies used for modelling.

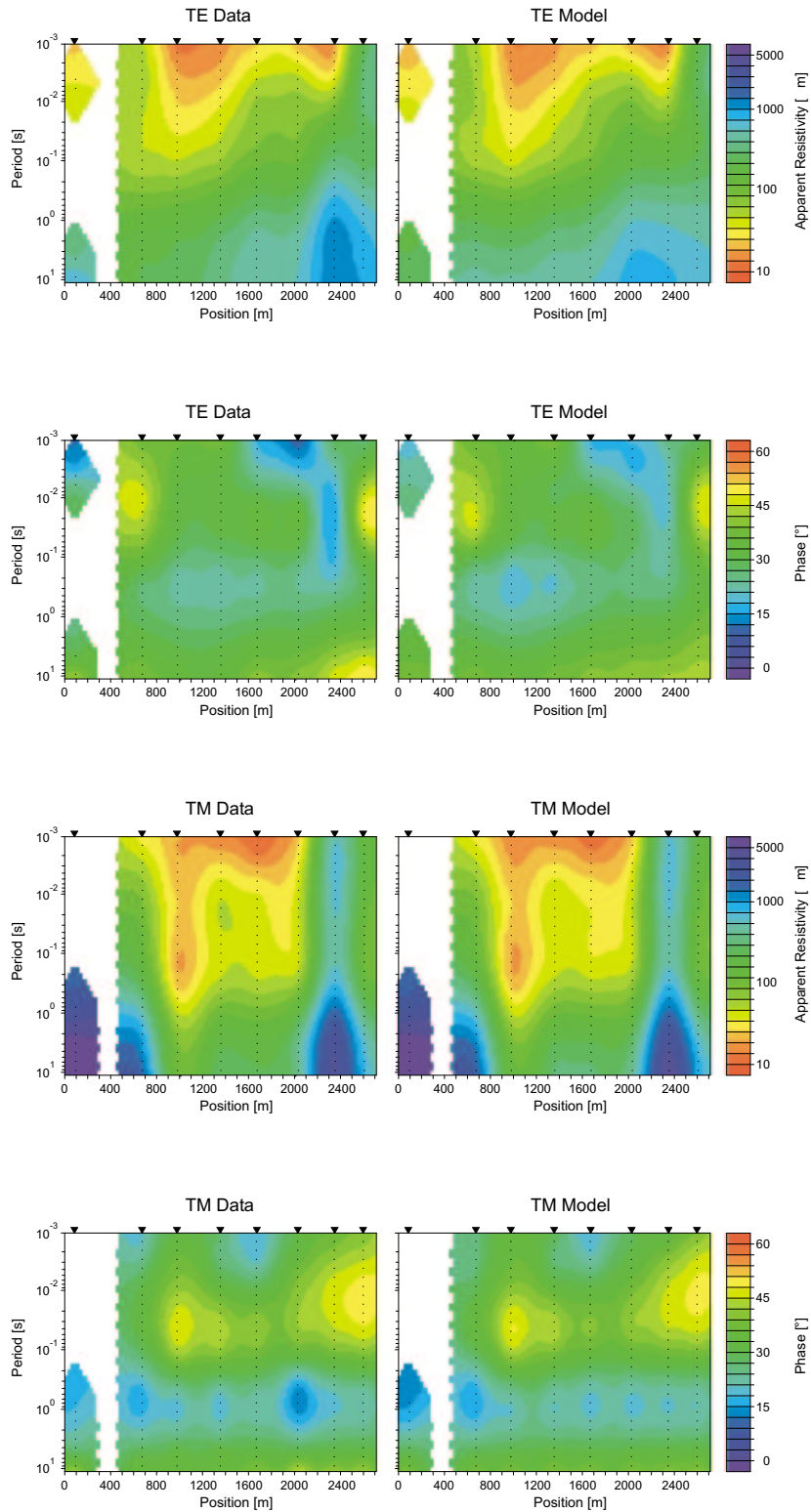


Fig. A3: Apparent resistivity and phase pseudosections for the South profile. The upper two rows are TE mode, the lower two rows TM mode sections. The left hand side shows data, the right hand side model response. Little black dots mark the frequencies used for modelling.

### A.3 Photo plates (Locations of photographs indicated on map, Appx. A.4)

#### Slip surfaces and slicken-lines

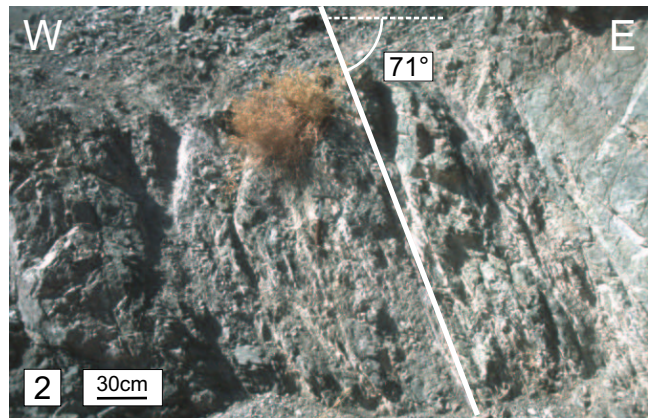
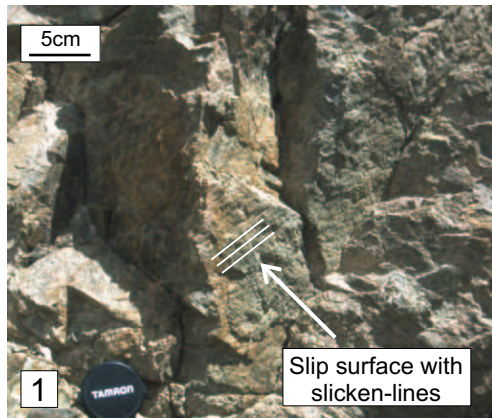


Photo 1: Slip surface with slicken-lines in Triassic andesites. This slip surface is coated with remains of a fine grained fault breccia on which the striation is preserved.

Photo 2: Outcrop close to the fault trace (Triassic andesites). Slip surfaces and several minor faults show consistent dip of about  $71^\circ$  towards the east.

#### Minor faults

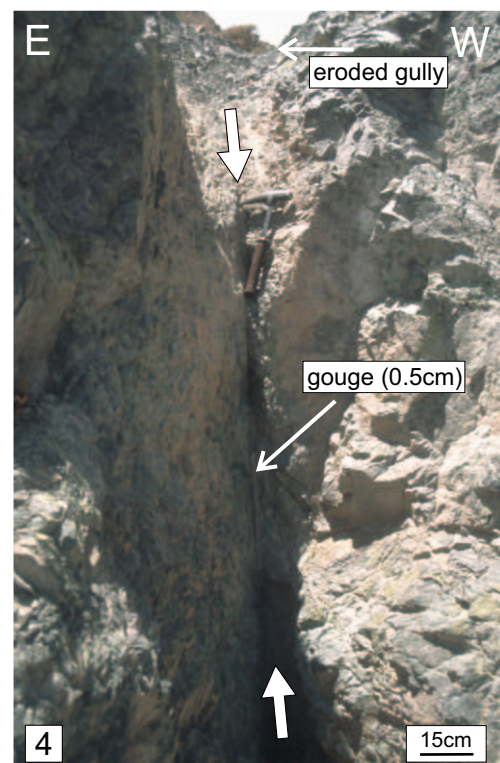
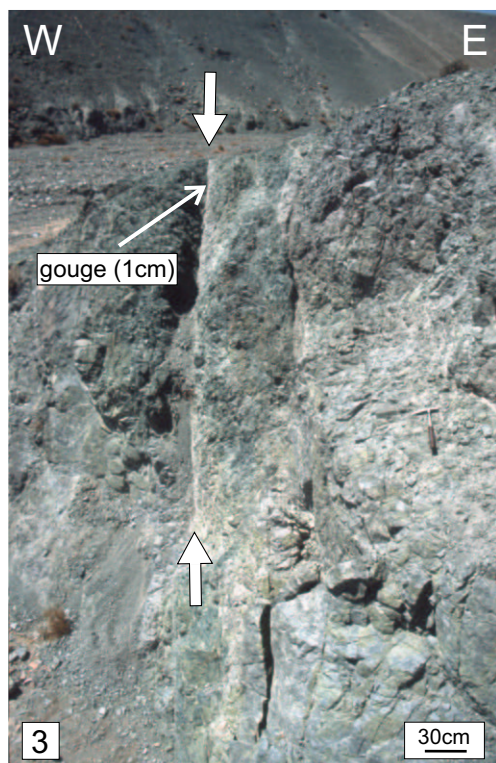


Photo 3: Vertical minor fault with 1 cm wide white gouge in strongly fractured and faulted Triassic andesites.

Photo 4: Vertical minor fault with brownish gouge of 0.5 cm width in Triassic andesites. Erosion formed a little gully.



### The alteration zone

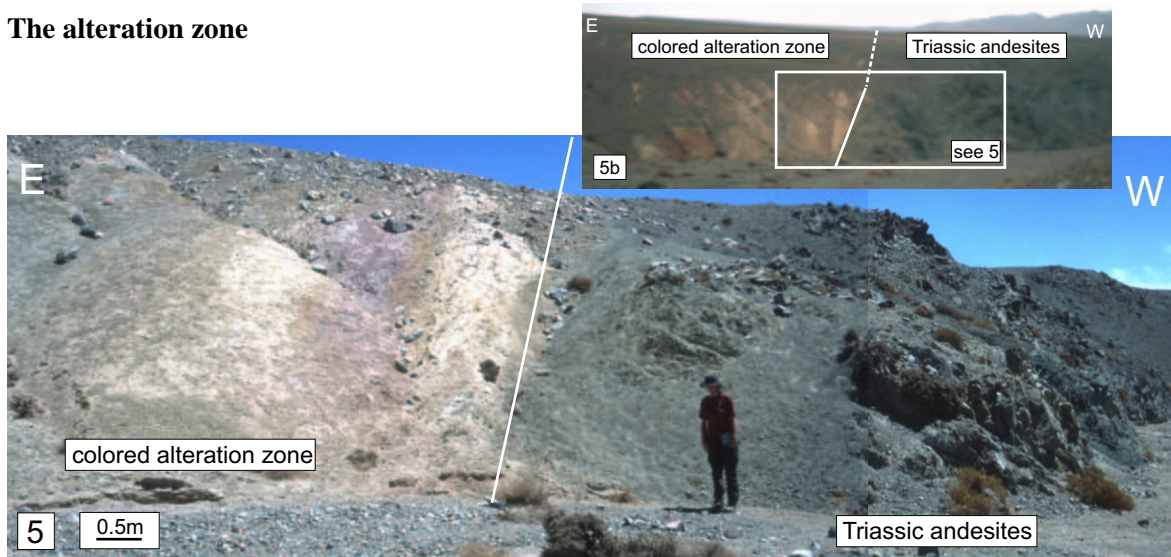


Photo 5: Contact of colored alteration zone in monzodiorites (left) to brittle deformed Triassic andesites (right). The inset gives an overview. Photos 2 and 3 were taken at the western edge of the shown Triassic outcrop. The outcrop faces in this picture are typical for the exposures in this main drainage valley.



Photo 6: Central region of the alteration zone.



Photo 7: Close up of some colored bands in the fluid alteration zone. The dip is representative for most bands.



Photo 8: Unconsolidated alteration zone material. Mineral and ore (mainly Fe-) enrichment processes cause the coloration.

## A.4 Map of the Gorila region

The map shows a slightly simplified representation of the geologic map of Makshev et al. (1999). A small map gives the geology of the surrounding area and the position of the South MT profile. Please refer to Fig. 3.1 in chapter 3 for a representation of the topography. Information included in the map are:

- The drainage valley system as extracted from aerial photography and field mapping. Branches that trend parallel to the West Fault strike, due to erosional exploit of less cohesive material, are marked with grey arrows.
- Midpoint positions of locations, where structural geology information were obtained (black dots).
- Rock sample sites for geochemical analysis (red points).
- Position of magnetotelluric stations. The orientation of the electrode layout (and, accordingly, the induction magnetometer coils) for each site of the Main profile is indicated with black crosses.
- Averaged bedding orientations of the Jurassic calcareous series.
- Position of the cold surface spring.
- Photography locations for the pictures shown in Appx. A.3.
- **Results of the kinematic analysis:** The results of the kinematic analysis, as outlined in section 4.3.2, are represented as pseudo-focal mechanisms. The orientation of shortening (P or  $\sigma_1$  axes, black dots) and elongation (T or  $\sigma_3$  axes, white squares) are used to construct two mutually perpendicular nodal planes that delimit quadrants of compression (white) and dilation (black). The intersection of the nodal planes is equivalent to the intermediate kinematic axes (B or  $\sigma_2$ ). See Fig. 4.7 for examples. This representation facilitates to distinguish between different deformation mechanisms, such as strike-slip (upper two rows on the map) and normal faulting (fourth row). Dextral and sinistral systems are separated according to their shortening axes orientation relative to the strike of the West Fault. The row entitled '*other*' shows additional results at a given outcrop (e.g. kinematic solutions that result from a distinct block). Outcrop A19 serves as example for the kinematic analysis in section 4.3.2. In three cases the orientation of the elongation axes did not cluster (radial extension), therefore only the orientation of the shortening axes is shown.

# Symbols and abbreviations

<b>General</b>	AFZ	Atacama Fault Zone	
	FZC	Fault Zone Conductor	
	GDS	Geomagnetic Depth Sounding	
	MT	Magnetotelluric(s)	
	PFS	Precordilleran Fault System	
	SAF	San Andreas Fault	
	WF, WFZ	West Fault, West Fault Zone	
	<b>MT / GDS</b>	$x, y, z$	cartesian coordinates, $x \equiv$ north, $y \equiv$ east, $z$ positive down
		$\underline{x}, \underline{y}$	unit vectors in respective coordinate direction
		$i$	imaginary unit ( $i^2 = -1$ )
<b>E</b>		electric field [V/m]	
<b>H</b>		magnetic field [A/m]	
<b>B</b>		magnetic induction [ $T=Vs/m^2$ ]	
$f$		frequency [Hz]	
$T$		period [s]	
$\omega$		angular frequency ( $= 2\pi f$ ) [Hz]	
$k$		complex wave number [1/m]	
$\mu_0$		magnetic permeability of free space [ $4\pi \cdot 10^{-7}$ Vs/Am]	
<b>j</b>		current density [ $A/m^2$ ]	
$\hat{Z}$		impedance tensor [m/s]	
$Z_{xx}, Z_{xy}, Z_{yx}, Z_{yy}$		elements of impedance tensor $\hat{Z}$	
$\rho, \rho_a$		absolute and apparent specific resistivity [ $\Omega m$ ]	
$\sigma$		specific electric conductivity [S/m]	
$\phi$		phase of impedance $\hat{Z}$ [ $^\circ$ ]	
$T_x, T_y$		magnetic transfer functions	
$S_{Swift}, S_{Bahr}$		Conventional (Swift) and phase sensitive (Bahr) tensor skewness	
$\theta$		Swift / Bahr angle [ $^\circ$ ]	
$\tau$	regularisation (smoothness) parameter		
<b>Geology &amp; Discussion</b>	$\sigma_1 > \sigma_2 > \sigma_3$	principle stress axes	
	P, B, T	principle strain axes (shortening, intermediate, extension)	
	$\mu_f$	coefficient of friction	
	$\Theta$	$\angle$ between $\sigma_1$ or P and fault plane [ $^\circ$ ]	
	$R$	stress ratio (shape factor) with $0 < R < 1$	
	$F$	Fluctuation [ $^\circ$ ]	
	$\rho_f, \rho_r$	specific resistivity of fluid or rock [ $\Omega m$ ]	
	$\Phi$	porosity [%]	
	$m$	Archie's Law exponent	
	$B$	equivalent concentration [mequ/l]	
	$l$	fault (segment) length [m]	
	$w$	damage zone (process zone) width [m]	
	$d$	fault displacement [m]	

# References

- ANCORP Working Group (1999): Seismic reflection image revealing offset of Andean subduction-zone earthquake locations into oceanic mantle. *Nature*, 397:341–344.
- Anders, M. H. & Wiltschko, D. V. (1994): Microfracturing, paleostress and the growth of faults. *J. Structural Geology*, 16(6):795–815.
- Angelier, J. (1984): Tectonic analysis of fault slip data sets. *J. Geophys. Res.*, 89(B7):5835–5848.
- Angelier, J. (1989): From orientation to magnitude in paleostress determinations using fault slip data. *J. Structural Geology*, 11(1/2):37–50.
- Angelier, J. & Goguel, J. (1979): Sur une méthode simple de détermination des axes principaux et contraintes pour une population de failles. *C.R. Acad. Sci. Paris*, 288:307–310.
- Angelier, J. & Mechler, P. (1977): Sur une méthode graphique de recherche des contraintes principales également utilisable en tectonique et en seismologie: la méthode des dièdres droits. *Bull. Soc. Géol. France*, 7(19):1309–1318.
- Angermann, D., Klotz, J. & Reigber, C. (1999): Space-geodetic estimation of the Nazca-South America Euler vector. *Earth Planet. Sci. Lett.*, 177:329–334.
- Bahr, K. (1988): Interpretation of the magnetotelluric impedance tensor: regional induction and local telluric distortion. *J. Geophys.*, 62:119–127.
- Bahr, K. (1991): Geological noise in magnetotelluric data: a classification of distortion types. *Phys. Earth Planet. Inter.*, 66:24–38.
- Beck, M. E. (1983): On the mechanism of tectonic transport in zones of oblique subduction. *Tectonophysics*, 93:1–11.
- Beck, S. L. (1996): Crustal-thickness variations in the central Andes. *Geology*, 24(5):407–410.
- Beck Jr., M. E. (1991): Coastwise transport reconsidered: lateral displacement in oblique subduction zones, and tectonic consequences. *Phys. Earth Planet. Inter.*, 68:1–8.
- Bedrosian, P. A., Unsworth, M. J., Egbert, G. & Thurber, C. (2001): Electrical structure of the creeping San Andreas Fault at Hollister, California. *EOS Transactions, AGU*, 82(47):S32E–04. Fall Meet. Supple., Abstract.
- Ben-Avraham, Z. & Zoback, M. D. (1992): Transform-normal extension and asymmetric basins: An alternative to pull-apart models. *Geology*, 20:423–426.
- Berdichevsky, M. N., Dmitriev, V. I. & Pozdnjakova, E. E. (1998): On two-dimensional interpretation of magnetotelluric soundings. *Geophys. J. Int.*, 133:585–606.
- Berkthold, A. (1982): Electrical conductivity of moisture containing rocks. In Angenheister, G., editor, *Physical properties of rocks*, volume 1b of *Landolt-Börnstein, Numerical Data and Functional Relationships in Science and Technology*, pages 262–275, Berlin. Springer Verlag.

- Blanpied, M. L., Lockner, D. A. & Byerlee, J. D. (1992): An earthquake mechanism based on rapid sealing of faults. *Nature*, 358:574–576.
- Bonnet, E., Bour, O., Odling, N. E., Davy, P., Main, I., Cowie, P. & Berkowitz, B. (2001): Scaling of Fracture Systems in Geological Media. *Rev. of Geophys.*, 39(3):347–383.
- Bott, M. H. P. (1959): The mechanics of oblique slip faulting. *Geol. Mag.*, 96(2):109–117.
- Brasse, H., Lezaeta, P., Schwalenberg, K., Soyer, W. & Haak, V. (2002): The Bolivian Altiplano Conductivity Anomaly. *J. Geophys. Res.*, 107(5):10.1029/2001JB000391.
- Brock, W. G. & Engelder, J. T. (1977): Deformation associated with the movement of the Muddy Mountain overthrust in the Buffington window, southeastern Nevada. *Bull. Geol. Soc. Am.*, 88:1667–1677.
- Buddin, T., Simpson, I. G. & Williams, G. D. (1993): North Chilean forearc tectonics and Cenozoic plate kinematics. *Tectonophysics*, 220:193–203.
- Byerlee, J. (1978): Friction of rocks. *Pure and Applied Geophys.*, 116:615–626.
- Byerlee, J. (1990): Friction, overpressure and fault normal compression. *Geophys. Res. Letters*, 17(12):2109–2112.
- Byerlee, J. (1993): Model for episodic flow of high-pressure water in fault zones before earthquakes. *Geology*, 21:303–306.
- Cagniard, L. (1953): Basic theory of the magneto-telluric method of geophysical prospecting. *Geophysics*, 18:605–635.
- Cahill, T. & Isacks, B. L. (1992): Seismicity and shape of the subducted Nazca plate. *J. Geophys. Res.*, 97(B12):17 503–17 529.
- Caine, J. S., Evans, J. P. & Forster, C. P. (1996): Fault zone architecture and permeability structure. *Geology*, 24(11):1125–1128.
- Caine, J. S. & Forster, C. P. (1999): Fault zone architecture and fluid flow: Insights from field data and numerical modeling. In Haneberg, W. C., editor, *Faults and subsurface fluid flow in the shallow crust*, volume 113 of *Geophys. Monograph*, pages 101–127. Am. Geophys. Union.
- Campbell, W. H., Schiffmacher, E. R. & Arora, B. R. (1992): Quiet geomagnetic field representation for all days and latitudes. *J. Geomag. Geoelect.*, 44:459–480.
- Camus, F. & Dilles, J. H. (2001): A special issue devoted to porphyry copper deposits of Northern Chile: Preface. *Econ. Geology*, 96(2):233–237.
- Cello, G. (2000): A quantitative structural approach to the study of active fault zones in the Apennines (Peninsular Italy). *J. Geodynamics*, 29:265–292.
- Cello, G., Gambini, R., Mazzoli, S., Read, A., Tondi, E. & Zucconi, V. (2000): Fault zone characteristics and scaling properties of the Val d’Agri Fault System (Southern Apennines, Italy). *J. Geodynamics*, 29:293–307.
- Cello, G., Invernizzi, C., Mazzoli, S. & Tondi, E. (2001): Fault properties and fluid flow patterns from Quaternary faults in the Apennines (Italy). *Tectonophysics*, 336:63–78.



- Chen, Y. H., Roecker, S. W., Thurber, C. & Lutter, W. (1996): P-wave precursors and tomographic images of the San Andreas Fault near Hollister, California. *EOS Transactions, AGU*, 77(46):466. Fall Meet. Supple., Abstract.
- Chernyshev, S. N. & Dearman, W. R. (1991): *Rock fractures*. Butterworth-Heinemann.
- Chester, F. M. & Chester, J. S. (1998): Ultracataclasite structure and friction processes of the Punchbowl fault, San Andreas system, California. *Tectonophysics*, 295:199–221.
- Chester, F. M., Evans, J. P. & Biegel, R. L. (1993): Internal structure and weakening mechanisms of the San Andreas Fault. *J. Geophys. Res.*, 98:771–786.
- Chester, F. M. & Logan, J. M. (1986): Implications for mechanical properties of brittle faults from observations of the Punchbowl Fault Zone, California. *Pure and Applied Geophys.*, 124(1/2):79–106.
- Chester, F. M. & Logan, J. M. (1987): Composite planar fabrics of gouge from the Punchbowl Fault, California. *J. Structural Geology*, 9(5/6):621–634.
- Coira, B., Davidson, J., Mpodozis, C. & Ramos, V. (1982): Tectonic and magmatic evolution of the Andes of northern Argentina and Chile. *Earth Sci. Rev.*, 18:303–332.
- Cowie, P. A. (1998): A healing–reloading feedback control on the growth rate of seismogenic faults. *J. Structural Geology*, 20(8):1075–1087.
- Cowie, P. A. & Scholz, C. H. (1992a): Displacement-length scaling relationship for faults: data synthesis and discussion. *J. Structural Geology*, 14(10):1149–1156.
- Cowie, P. A. & Scholz, C. H. (1992b): Growth of faults by accumulation of seismic slip. *J. Geophys. Res.*, 97(B7):11 085–11 095.
- Cowie, P. A. & Scholz, C. H. (1992c): Physical explanation for the displacement-length relationship of faults using a post-yield fracture mechanics model. *J. Structural Geology*, 14(10):1133–1148.
- Cowie, P. A. & Shipton, Z. K. (1998): Fault tip displacement gradients and process zone dimensions. *J. Structural Geology*, 20(8):983–997.
- Cuadra, P. & Rojas, G. (2001): Oxide mineralisation at the Radomiro Tomic porphyry copper deposit, Northern Chile. *Econ. Geology*, 96:387–400.
- Delouis, B. (1998): Recent crustal deformation in the Antofagasta region. *Geophys. J. Int.*, 132:302–338.
- DeMets, C., Gordon, R. G., Argus, D. F. & Stein, S. (1994): Effect of recent revision to the geomagnetic reversal time scale on estimates of current plate motion. *Geophys. Res. Letters*, 21:2191–2194.
- DeSilva, S. L. & Francis, P. W. (1991): *Volcanoes of the Central Andes*. Springer Verlag, Berlin, Heidelberg, New York.
- Dilles, J., Tomlinson, A. J., Martin, M. & Blanco, N. (1997): The El Abra and Fortuna complexes: a porphyry copper batholith sinistrally displaced by the Falla Oeste. In *VIII Congreso Geológico Chileno, ACTAS Vol III – Nuevos Antecedentes de la Geología del Distrito de Chuquicamata, Periodo 1994–1995–Sesión 1: Geología Regional*. Universidad Católica del Norte, Departamento de Ciencias Geológicas.

- Doblas, M. (1998): Slickenside kinematic indicators. *Tectonophysics*, 295:187–197.
- Duba, A. G., Mathez, E. A. & Shankland, T. J. (2001): Workshop Addresses Crustal Carbon and its Effect on Electrical Conductivity. *EOS Transactions, AGU*, 82(40):456.
- Eberhart-Phillips, D., Stanley, W. D., Rodriguez, B. D. & Lutter, W. J. (1995): Surface seismic and electrical methods to detect fluids related to faulting. *J. Geophys. Res.*, 100(B7):12 919–12 936.
- Echternacht, F. (1998): *Die elektrische Leitfähigkeitsstruktur im Forearc der südlichen Zentralanden bei 20°–21°S, abgeleitet aus magnetotellurischen und geomagnetischen Sondierungen*. PhD thesis, Freie Universität Berlin, GFZ-Scientific Technical Report STR98/20.
- Echternacht, F., Tauber, S., Eisel, M., Brasse, H., Schwarz, G. & Haak, V. (1997): Electromagnetic study of the active continental margin in northern Chile. *Phys. Earth Planet. Inter.*, 102:69–87.
- Elektb Group (1997): KTB and the electrical conductivity of the crust. *J. Geophys. Res.*, 102(B8):18 289–18 305.
- Etchecopar, A., Vasseur, G. & Daignieres, M. (1981): An inverse problem in microtectonics for the determination of stress tensors from fault striation analysis. *J. Structural Geology*, 3(1):51–65.
- Etheridge, M. A., Wall, V. J. & Vernon, R. H. (1983): The role of the fluid phase during regional metamorphism and deformation. *J. Metamorphic Geol.*, 1:205–226.
- Evans, J. P., Forster, C. B. & Goddard, J. V. (1997): Permeability of fault-related rocks, and implications for hydraulic structure of fault zones. *J. Structural Geology*, 19(11):1393–1404.
- Faulkner, D. R. (2001): On the internal structure and mechanics of large strike-slip fault zones: Field observations of the Carboneras Fault in Southeastern Spain. *EOS Transactions, AGU*, 82(47):T31B–0839. Fall Meet. Supple., Abstract.
- Faulkner, D. R. & Rutter, E. H. (2001): Can the maintenance of overpressured fluids in large strike-slip fault zones explain their apparent weakness? *Geology*, 29(6):503–506.
- Fischer, G., Szarka, L., Adam, A. & Weaver, J. T. (1992): The magnetotelluric phase over 2-D structures. *Geophys. J. Int.*, 108:778–786.
- Fitch, T. J. (1972): Plate convergence, transcurrent faults, and internal deformation adjacent to southeast Asia and the western Pacific. *J. Geophys. Res.*, 77:4432–4460.
- Fournier, R. O. & Potter, R. W. (1982): An equation correlating the solubility of quartz in water from 25 to 900°C at pressure up to 10 000 bars. *Geochim. Cosmochim. Acta*, 46:1969–1973.
- Gamble, T. D., Goubeau, W. M. & Clarke, J. (1979): Magnetotellurics with remote magnetic reference. *Geophysics*, 44(1):53–68.
- Gapais, D., Cobbold, P. R., Bourgeois, O., Rouby, D. & de Urreizeta, M. (2000): Tectonic significance of fault-slip data. *J. Structural Geology*, 22:881–888.
- Giese, P., Scheuber, E., Schilling, F., Schmitz, M. & Wigger, P. (1999): Crustal thickening processes in the Central Andes and the different natures of the Moho–discontinuity. *J. South Americ. Earth Sci.*, 12:201–220.

- Glover, P., Hole, M. J. & Pous, J. (2000): A modified Archie's law for two conducting phases. *Earth Planet. Sci. Lett.*, 180:369–383.
- Gray, D. R., Janssen, C. & Wapnik, J. (1999): Deformation character and fluid flow across a wrench fault within Paleozoic accretionary wedge: Waratah Fault Zone, southeastern Australia. *J. Structural Geology*, 21:194–214.
- Groom, R. W. & Bailey, R. C. (1989): Decomposition of magnetotelluric impedance tensors in presence of local three-dimensional galvanic distortion. *J. Geophys. Res.*, 94(B2):1913–1925.
- Groom, R. W., Kurtz, R. D., Jones, A. G. & Boerner, D. E. (1993): A quantitative methodology to extract regional magnetotelluric impedances and determine the dimension of the conductivity structure. *Geophys. J. Int.*, 115:1095–1118.
- Gudmundsson, A. (2000): Active fault zones and groundwater flow. *Geophys. Res. Letters*, 27(18):2993–2996.
- Günther, A. (2001): *Strukturgeometrie, Kinematik und Deformationsgeschichte des oberkretazisch-alttertiären magmatischen Bogens (nord-chilenische Präkordillere, 21,7°-23°S)*. PhD thesis, Freie Universität Berlin.
- Gutenberg, B. & Richter, C. F. (1954): *Seismicity of the Earth*. Princeton University Press.
- Haak, V. & Hutton, V. R. S. (1986): Electrical resistivity in continental lower crust. In Dawson, J. B., editor, *The Nature of the Lower Continental Crust*, volume 24 of *Spec. Publ.*, pages 35–49. Geol. Soc. London.
- Hartley, A. J., May, G., Chong, G., Turner, P., Kape, S. J. & Jolley, E. J. (2000): Development of a continental forearc: A Cenozoic example from the Central Andes, northern Chile. *Geology*, 28(4):331–334.
- Hickman, S. H. (1991): Stress in the lithosphere and the strength of active faults. *Rev. of Geophys., Suppl.*, 29:759–775.
- Hickman, S. H., Sibson, R. & Bruhn, R. (1995): Mechanical involvement of fluids in faulting. *J. Geophys. Res.*, 100:12 831–12 840.
- Hobbs, B. A. (1992): Terminology and symbols for use in studies of electromagnetic induction in the Earth. *Surv. in Geophys.*, 13:489–515.
- Hoefs, J. (1987): *Stable Isotope Geochemistry*. 3rd edition. 241 pp. Springer-Verlag.
- Hoepfner, R. (1955): Tektonik im Schiefergebirge. *Geol. Rundschau*, 44(1):26–58.
- Hoffmann-Rothe, A., Ritter, O. & Haak, V. (2001): Magnetotelluric and geomagnetic modelling reveals zones of very high electrical conductivity in the upper crust of Central Java. *Phys. Earth Planet. Inter.*, 124:131–151.
- Isacks, B. (1988): Uplift of the central Andean plateau and bending of the Bolivian orocline. *J. Geophys. Res.*, 93:3211–3231.
- Janssen, C., Hoffmann-Rothe, A., Tauber, S. & Wilke, H. (2002): Internal structure of the Precordilleran fault system (Chile) - insights from structural and geophysical observations. *J. Structural Geology*, 24:123–143.
- Janssen, C., Lüders, V. & Hoffmann-Rothe, A. (submitted): Contrasting styles of fluid-rock interaction within the West Fissure Zone (Chile). *Tectonophysics*.

- Jones, A. G. (1988): Static shift of magnetotelluric data and its removal in a sedimentary basin environment. *Geophysics*, 53(7):967–978.
- Jones, A. G. (1992): Electrical conductivity of the continental lower crust. In Fountain, D. M., Arculus, R. J. & Kay, R. W., editors, *Continental Lower Crust*, pages 81–143. Elsevier, Amsterdam.
- Jones, A. G. (1998): Waves of the future: Superior inferences from collocated seismic and electromagnetic experiments. *Tectonics*, 286:273–298.
- Jones, A. G., Kurtz, R. D., Boerner, D. E., Craven, J. A., McNeice, G. W., Gough, D. I., DeLaurier, J. M. & Ellis, R. G. (1992): Electromagnetic constraints on strike-slip fault geometry – The Fraser River fault system. *Geology*, 20:561–564.
- Jordan, T. E. & Alonso, R. N. (1987): Cenozoic stratigraphy and basin tectonics of the Andes mountains, 20–28° south latitude. *Am. Assoc. Petrol. Geol. Bull.*, 71:49–64.
- Junge, A. (1994): *Induzierte elektrische Felder - neue Beobachtungen in Norddeutschland und im Bramwald*. Habil., Math.-nat. Fachb., Univ. Göttingen.
- Junge, A. (1996): Characterization of and correction for cultural noise. *Surv. Geophys.*, 17:361–391.
- Kaufman, A. A. & Keller, G. V. (1981): *The Magnetotelluric Sounding Method*, volume 15 of *Methods in Geochemistry and Geophysics*. Elsevier Scientific Publishing Company, Amsterdam, Oxford, New York.
- Kharaka, Y. K., Thordsen, J. J. & Evans, W. C. (1999): Geochemistry and hydromechanical interactions of fluids associated with the San Andreas Fault System, California. In Haneberg, W. C., editor, *Faults and subsurface fluid flow in the shallow crust*, volume 113 of *Geophys. Monograph*, pages 129–148. Am. Geophys. Union.
- Kim, Y.-S., Andrews, J. R. & Sanderson, D. J. (2001): Reactivated strike-slip faults: examples from north Cornwall, UK. *Tectonophysics*, 340:173–194.
- Kley, J. & Monaldi, C. R. (1998): Tectonic shortening and crustal thickness in the central Andes: How good is the correlation. *Geology*, 26:723–726.
- Labaume, P., Sheppard, S. M. F. & Moretti, I. (2001): Fluid flow in cataclastic thrust fault zones in sandstones, Sub-Andean Zone, southern Bolivia. *Tectonophysics*, 340:141–172.
- Lamb, D. H. & Hoke, L. (1997): Origin of the high plateau on the Central Andes, Bolivia, South America. *Tectonics*, 16:623–649.
- Lezaeta, P. (2001): *Distortion analysis and 3-D modeling of magnetotelluric data in the Southern Central Andes*. PhD thesis, Freie Universität Berlin.
- Li, Y., Ellsworth, W. L., Thurber, C. H., Malin, P. E. & Aki, K. (1997): Fault-zone guided waves from explosions in the San Andreas Fault at Parkfield and Cienega Valley, California. *Bul. Seismol. Soc. Am.*, 87:210–221.
- Lindsay, D., Zentilli, M. & Ossandon, G. (1996): Falla Oeste fault system: record of its regional significance as exposed in the Chuquicamata open pit, northern Chile. In *Third Int. Symp. Andean Geodynamics*, pages 427–430, St. Malo.

- Lindsay, D., Zentilli, M. & Rojas de la Rivera, J. (1995): Evolution of an active ductile to brittle shear system controlling mineralization at the Chuquicamata porphyry copper deposit, Chile. *Int. Geol. Rev.*, 37:945–958.
- Little, T. A. (1995): Brittle deformation adjacent to the Awatare strike-slip fault in New Zealand: Faulting patterns, scaling relationships, and displacement partitioning. *GSA Bulletin*, 107(11):1255–1271.
- Lockner, D., Byerlee, J. D., Kuksenko, V., Ponomarev, A. & Sidorin, A. (1991): Quasi-static fault growth and shear fracture energy in granite. *Nature*, 350:39–42.
- Logan, J. M., Dengo, C. A., Higgs, N. G. & Wang, Z. Z. (1992): Fabrics of Experimental Fault Zones: Their Development and Relationship to Mechanical Behavior. In Evans, B. & Wong, T.-F., editors, *Fault Mechanics and Transport Properties of Rocks*, pages 33–67. Academic Press.
- Mackie, R. L., Livelybrooks, D. W., Madden, T. R. & Larsen, J. C. (1997): A magnetotelluric investigation of the San Andreas fault at Carrizo Plain, California. *Geophys. Res. Letters*, 24(15):1847–1850.
- Maksaev, V., Dilles, H. H. & Tomlinson, A. J. (1999): *Mapa geológico del Cuadrángulo Cerros de Paqui, Región de Antofagasta. 1 mapa escala 1:50.000*. Servicio Nacional de Geología y Minería y Cooperación Nacional del Cobre, Registered Report. Geological Map, new reference.
- Maksaev, V. & Tomlinson, A. J. (1995): *Cuadrangulo Cerros de Paqui, Región de Antofagasta, Escala 1:50 000*. Servicio Nacional de Geología y Minería y Cooperación Nacional del Cobre. Geological Map.
- Mandl, G. (1993): *Mechanics of tectonic faulting - models and basic concepts*. Developments in Structural Geology. Elsevier. 407 pp.
- Marrett, R. & Allmendinger, R. W. (1990): Kinematic analysis of fault-slip data. *J. Structural Geology*, 12:973–986.
- McCaffrey, R. (1992): Oblique plate convergence, slip vectors, and forearc deformation. *J. Geophys. Res.*, 97(B6):8905–8915.
- McCaffrey, R. (1996): Estimates of modern arc-parallel strain rates in fore arcs. *Geology*, 24(1):27–30.
- McCaig, A. M. (1989): Fluid flow through fault zones. *Nature*, 340:600.
- McInnes, B. I. A., Farley, K. A., Sillitoe, R. H. & Kohn, B. P. (1999): Application of apatite (U-Th)/He thermochronometry to the determination of the sense and amount of vertical displacement at the Chuquicamata porphyry copper deposit, Chile. *Economic Geology*, 94:937–948.
- McNeice, G. W. & Jones, A. G. (2001): Multisite, multifrequency tensor decomposition of magnetotelluric data. *Geophysics*, 66(1):158–173.
- Michel, G. W. (1993): Modeling Fault-slip Data Sets: a Key for Approximating Stretching Ratios? *Z. dt. geol. Ges.*, 144:150–158.
- Michel, G. W. (1994): *Neo-Kinematics along the North Anatolian Fault (Turkey)*. Tübinger Geowiss. Arb., Reihe A, Band 16. Tübingen.
- Miller, D. D. (1998): Distributed shear, rotation, and partitioned strain along the San Andreas fault, central California. *Geology*, 26(10):867–870.

- Mitra, G. & Ismat, Z. (2001): Microfracturing associated with reactivated fault zones and shear zones: what can it tell us about deformation history? In Holdsworth, R. E., Strachan, R. A., Magloughlin, J. F. & Knipe, R. J., editors, *The Nature and Tectonic Significance of Fault Zone Weakening*, volume 186 of *Geological Society, Special Publications*, pages 113–140. London.
- Mpodozis, C., Marinovic, N. & Smoje, I. (1993): Eocene left lateral strike-slip faulting and clockwise block rotations in the Cordillera de Domeyko, west of Salar de Atacama, northern Chile. In *Second Int. Symp. Andean Geodynamics*, pages 225–228, Oxford, UK.
- Mpodozis, C. & Tomlinson, A. (1998): Antithetic trench-parallel strike-slip faults: the Cenozoic Domeyko Fault System of Northern Chile. In *Fall 1998 AGU Meeting, Abstract*.
- Norabuena, E. O., Dixon, T. H., Stein, S. & Harrison, C. G. A. (1999): Decelerating Nazca-South America and Nazca-Pacific plate motions. *Geophys. Res. Letters*, 26:3405–3408.
- Ossandón, G., Fréaut, R., Gustafson, L. B., Lindsay, D. D. & Zentilli, M. (2001): Geology of the Chuquicamata Mine: A Progress Report. *Econ. Geology*, 96:249–270.
- Palacky, G. J. (1987): Resistivity characteristics of geologic targets. In Nabighian, M. N., editor, *Electromagnetic Methods in Applied Geophysics – Theory*, volume 1, pages 53–129. Soc. Explor. Geophys., Tulsa, Okla.
- Pardo, R. (1995): *Prospecto Arkansa - Borde Occidental Cerros de Paqui (Informe de Avance), II Region*. CODELCO, Chile, Vicepresidencia de Exploraciones y Asociaciones Mineras, Calama, Marzo 1995.
- Pardo-Casas, F. & Molnar, P. (1987): Relative motion of the Nazca (Farallon) and South American plates since late Cretaceous time. *Tectonics*, 6:233–248.
- Parry, W. T. (1998): Fault-fluid compositions from fluid-inclusion observation and solubilities of fracture-sealing minerals. *Tectonophysics*, 290:1–26.
- Peacock, D. C. P. & Marrett, R. (2000): Strain and stress: Reply. *J. Structural Geology*, 22:1369–1378.
- Pek, J. & Verner, T. (1997): Finite-difference modelling of magnetotelluric fields in two-dimensional anisotropic media. *Geophys. J. Int.*, 128:505–521.
- Pelz, K. (2000): *Tektonische Erosion am zentralandinen Forearc (20–24°S)*. Scientific Technical Report STR00/20 (GFZ), Freie Universität Berlin.
- Pemberton, G. B. (1997): *Dating of alteration at the Radomiro Tomic porphyry copper deposit, northern Chile by the high precision <sup>40</sup>Ar/<sup>39</sup>Ar method; (Bachelor)*. Dalhousie University, Halifax, NS, Canada. Abstract.
- Petit, J.-P. (1987): Criteria for sense of movement on fault surfaces in brittle rocks. *J. Structural Geology*, 9(5/6):597–608.
- Poll, H. E., Weaver, J. T. & Jones, A. G. (1989): Calculations of voltages for magnetotelluric modelling of a region with near-surface inhomogeneities. *Phys. Earth Planet. Inter.*, 53:287–297.
- Pollard, D. D. (2000): Strain and stress: Discussion. *J. Structural Geology*, 22:1359–1367.
- Rawling, G. C., Goodwin, L. B. & Wilson, J. L. (2001): Internal architecture, permeability structure, and hydrologic significance of contrasting fault-zone types. *Geology*, 29(1):43–46.

- Reches, Z. & Lockner, D. A. (1994): Nucleation and growth of faults in brittle rocks. *J. Geophys. Res.*, 99(B9):18 159–18 173.
- Renard, F., Gratier, J.-P. & Jamtveit, B. (2000): Kinetics of crack-sealing, intergranular pressure solution, and compaction around active faults. *J. Structural Geology*, 22:1395–1407.
- Reutter, K.-J., Döbel, R., Bogdanic, T. & Kley, J. (1994): Geological map of the central Andes between 20° - 26° S. In Reutter, K.-J., Scheuber, E. & Wigger, P., editors, *Tectonics of the Southern Central Andes*. Springer.
- Reutter, K.-J., Scheuber, E. & Chong, G. (1996): The Precordilleran fault system of Chuquicamata, Northern Chile: evidence for reversals along arc-parallel strike-slip faults. *Tectonophysics*, 259:213–228.
- Reutter, K.-J., Scheuber, E. & Helmcke, D. (1991): Structural evidence of orogen-parallel strike slip displacements in the Precordillera of northern Chile. *Geol. Rundschau*, 80:135–153.
- Reynolds, P., Ravenhurst, C., Zentilli, M. & Lindsay, D. (1998): High-precision  $^{40}\text{Ar}/^{39}\text{Ar}$  dating of two consecutive hydrothermal events in the Chuquicamata porphyry copper system, Chile. *Chemical Geology*, 148:45–60.
- Rice, J. R. (1992): Fault stress states, pore pressure distributions, and the weakness of the San Andreas Fault. In Evans, B. & Wong, T.-F., editors, *Fault Mechanics and Transport Properties of Rocks*, pages 474–503. Academic Press.
- Riedel, W. (1929): Zur Mechanik geologischer Brucherscheinungen. *Centralbl. f. Mineral. Geol. u. Pal.*, 1929:354–368.
- Ritter, O. (1995): *An audiomagnetotelluric investigation of the Southern Upland Fault: novel instrumentation, field procedures and 3D modelling*. PhD thesis, University of Edinburgh.
- Ritter, O., Junge, A. & Dawes, G. J. K. (1998): New equipment and processing for magnetotelluric remote reference observations. *Geophys. J. Int.*, 132:535–548.
- Rodi, W. & Mackie, R. L. (2001): Nonlinear conjugate gradients algorithm for 2-D magnetotelluric inversion. *Geophysics*, 66(1):174–187.
- Rutter, E. H., Holdsworth, R. E. & Knipe, R. J. (2001): The nature and tectonic significance of fault-zone weakening: an introduction. In Holdsworth, R. E., Strachan, R. A., Magloughlin, J. F. & Knipe, R. J., editors, *The Nature and Tectonic Significance of Fault Zone Weakening*, volume 186 of *Geological Society, Special Publications*, pages 1–11. London.
- Scheuber, E. & Andriessen, P. A. M. (1990): The kinematic and geodynamic significance of the Atacama fault zone, Northern Chile. *J. Structural Geology*, 12(2):243–257.
- Scheuber, E., Bogdanic, T., Jensen, A. & Reutter, K.-J. (1994): Tectonic development of the North Chilean Andes in relation to plate convergence and magmatism since the Jurassic. In Reutter, K.-J., Scheuber, E. & Wigger, P., editors, *Tectonics of the Southern Central Andes*, pages 121–139. Springer.
- Scheuber, E. & Giese, P. (1999): Architecture of the Central Andes – a compilation of geoscientific data along a transect at 21°S. *J. South Americ. Earth Sci.*, 12:103–107.

- Scheuber, E., Hammerschmidt, K. & Friedrichsen, H. (1995):  $^{40}\text{Ar}/^{39}\text{Ar}$  and Rb-Sr analyses from ductile shear zones from the Atacama Fault Zone, northern Chile: the age of deformation. *Tectonophysics*, 250:61–87.
- Schlische, R. W., Young, S. S., Ackermann, R. V. & Gupta, A. (1996): Geometry and scaling relations of a population of very small rift-related normal faults. *Geology*, 24(8):683–686.
- Schmitz, M. (1994): A balanced model of the southern Central Andes. *Tectonics*, 13:484–492.
- Schmucker, U. (1970): Anomalies of geomagnetic variations in the south-western United States. *Bull. Scripps Inst. Oceanogr.*, 13:1–165.
- Scholz, C. H. (1990): *The Mechanics of Earthquakes and Faulting*. Cambridge Univ. Press. 439 pp.
- Scholz, C. H. & Cowie, P. A. (1990): Determination of total strain from faulting using slip measurements. *Nature*, 346:837–839.
- Scholz, C. H., Dawers, N. H., Yu, J.-Z., Anders, M. H. & Cowie, P. A. (1993): Fault growth and fault scaling laws: Preliminary results. *J. Geophys. Res.*, 98(B12):21 951–21 961.
- Scholz, C. H. & Gupta, A. (2000): Fault interactions and seismic hazard. *J. Geodynamics*, 29:459–467.
- Schopper, J. R. (1982): Electrical conductivity of rocks containing electrolytes. In Angenheister, G., editor, *Physical properties of rocks*, volume 1b of *Landolt-Börnstein, Numerical Data and Functional Relationships in Science and Technology*, pages 276–291, Berlin. Springer Verlag.
- Schultz, R. & Fossen, H. (2002): Displacement-length scaling in three dimensions: the importance of aspect ratio and application to deformation bands. *J. Structural Geology*, 24:1389–1411.
- Schulz, S. E. & Evans, J. P. (1998): Spatial variability in microscopic deformation and composition of the Punchbowl fault, southern California: implications for mechanisms, fluid-rock interaction, and fault morphology. *Tectonophysics*, 295:223–244.
- Schulz, S. E. & Evans, J. P. (2000): Mesoscopic structure of the Punchbowl fault, Southern California and the geologic and geophysical structure of active strike-slip faults. *J. Structural Geology*, 22:913–930.
- Schwalenberg, K. (2000): *Die Leitfähigkeitsstruktur der Zentralen Anden bei 21°S. Zweidimensionale Modellstudien und Untersuchungen zur Auflösbarkeit*. PhD thesis, Freie Universität Berlin, GFZ-Scientific Technical Report STR00/24.
- Schwarz, G. & Krüger, D. (1997): Resistivity cross section through the southern central Andes as inferred from magnetotelluric and geomagnetic deep soundings. *J. Geophys. Res.*, 102:11 957–11 978.
- Sempere, T., Hérail, G., Oller, J. & Bonhomme, M. (1990): Late Oligocene-Early Miocene major tectonic crisis and related basins in Bolivia. *Geology*, 18:946–949.
- Sheppard, S. M. F. & Gilg, H. A. (1995): Stable isotope geochemistry of clay minerals. *Clay Mineralogy*, 31:1–24.
- Sibson, R. H. (1986): Brecciation Processes in Fault Zones: Inferences from Earthquake Rupturing. *Pure and Applied Geophys.*, 124(1/2):159–173.



- Sibson, R. H. (1996): Structural permeability of fluid-driven fault-fracture meshes. *J. Structural Geology*, 18(8):1031–1042.
- Sillitoe, R. H. & McKee, E. H. (1996): Age of supergene oxidation and enrichment in the Chilean porphyry copper province. *Economic Geology*, 91:164–179.
- Sleep, N. H. & Blanpied, M. L. (1992): Creep, compaction and the weak rheology of major faults. *Nature*, 359:687–692.
- Smith, J. T. (1995): Understanding telluric distortion matrices. *Geophys. J. Int.*, 122:219–226.
- Somoza, R. (1998): Updated Nazca (Farallon)- South America relative motions during the last 40 My: implications for mountain building in the central Andean region. *J. South American Earth Sciences*, 11(3):211–215.
- Soyer, W. (2002): *Analysis of geomagnetic variations at the Chilean active continental margin*. PhD thesis, Freie Universität Berlin. in preparation.
- Soyer, W. & Brasse, H. (2001): A magneto-variation array study in the central Andes of N Chile and SW Bolivia. *Geophys. Res. Letters*, 28(15):3023–3026.
- Spang, J. H. (1972): Numerical method for dynamic analysis of calcite twin lamellae. *Geol. Soc. Am. Bull.*, 83:467–472.
- Sperner, B. (1996): *Computer programs for the kinematic analysis of brittle deformation structures and the Tertiary tectonic evolution of the Western Carpathians (Slovakia)*. Tübinger Geowiss. Arb., Reihe A, Band 27. Tübingen.
- Sperner, B. & Ratschbacher, L. (1994): A Turbo Pascal program package for graphical presentation and stress analysis of calcite deformation. *Z. dt. geol. Ges.*, 145:414–423.
- Sperner, B., Ratschbacher, L. & Ott, R. (1993): Fault-striae analysis: A Turbo Pascal program package for graphical presentation and reduced stress tensor calculation. *Computers & Geosciences*, 19(9):1361–1388.
- Spitzer, K. (2001): Magnetotelluric static shift and direct current sensitivity. *Geophys. J. Int.*, 144(2):289–299.
- Springer, M. (1999): Interpretation of heat-flow density in the Central Andes. *Tectonophysics*, 306:377–395.
- Springer, M. & Förster, A. (1998): Heat-flow density across the Central Andean subduction zone. *Tectonophysics*, 291:123–139.
- Swift, C. M. (1967): *A Magnetotelluric Investigation of an Electrical Conductivity Anomaly in the Southwestern United States*. PhD thesis, MIT, Dept. of Geol. and Geophys., Cambridge, Mass.
- Sylvester, A. G. (1988): Strike-slip faults. *Geol. Soc. Am. Bull.*, 100:1666–1703.
- Tauber, S. (2002): *Audiomagnetotellurik an der Limon Verde Störung, Nord-Chile*. PhD thesis, Freie Universität Berlin. in preparation.
- Tchalenko, J. S. (1970): Similarities between shear zones of different magnitudes. *Geol. Soc. Am. Bull.*, 81:1625–1640.

- Telford, W. M., Geldart, L. P. & Sheriff, R. E. (1990): *Applied Geophysics, Second Edition*. Cambridge University Press, Cambridge.
- Tikhonov, A. N. (1950): On determining electrical characteristics of the deep layers of the Earth. *Dokl. Akad. Nauk. SSSR*, 73:295–297.
- Tikoff, B. & Wojtal, S. F. (1999): Displacement control of geologic structures. *J. Structural Geology*, 21(8–9):959–967.
- Tomlinson, A. J. & Blanco, N. (1997a): Structural evolution and displacement history of the West Fault system, Precordillera, Chile: part I, synmineral history. In *VIII Congreso Geológico Chileno*, ACTAS Vol III – Nuevos Antecedentes de la Geología del Distrito de Chuquicamata, Periodo 1994–1995–Sesión 1: Geología Regional, pages 1873–1877. Universidad Católica del Norte, Departamento de Ciencias Geológicas.
- Tomlinson, A. J. & Blanco, N. (1997b): Structural evolution and displacement history of the West Fault system, Precordillera, Chile: part II, postmineral history. In *VIII Congreso Geológico Chileno*, ACTAS Vol III – Nuevos Antecedentes de la Geología del Distrito de Chuquicamata, Periodo 1994–1995–Sesión 1: Geología Regional, pages 1878–1882. Universidad Católica del Norte, Departamento de Ciencias Geológicas.
- Torgersen, T. (1990): Crustal-scale fluid transport - Magnitude and mechanisms. *EOS Transactions, AGU*, 71(1):4–6.
- Turner, F. J. (1953): Nature and dynamic interpretation of deformation lamellae in calcite of three marbles. *Am. Jour. Science*, 251(4):276–198.
- Twiss, R. J. & Unruh, J. R. (1998): Analysis of fault slip inversion: do they constrain stress or strain rate? *J. Geophys. Res.*, 103(6):12 205–12 222.
- Unsworth, M. J., Bedrosian, P., Eisel, M., Egbert, G. D. & Siripunvaraporn, W. (2000): Along strike variations in the electrical structure of the San Andreas Fault at Parkfield, California. *Geophys. Res. Letters*, 27(18):3021–3024.
- Unsworth, M. J., Egbert, G. D. & Booker, J. R. (1999): High resolution electromagnetic imaging of the San Andreas fault in Central California. *J. Geophys. Res.*, 104:1131–1150.
- Unsworth, M. J., Malin, P. E., Egbert, G. D. & Booker, J. R. (1997): Internal structure of the San Andreas fault at Parkfield, California. *Geology*, 25(4):359–362.
- Vermilye, J. M. & Scholz, C. H. (1998): The process zone: A microstructural view of fault growth. *J. Geophys. Res.*, 103(B6):12 223–12 237.
- Victor, P. (2000): *Die Entwicklung der Altiplano Westflanke und ihre Bedeutung für die Plateaubildung und Krustenverdickung in N-Chile (20-21°S)*. Scientific Technical Report STR00/13 (GFZ), Freie Universität Berlin.
- von Huene, R., Weinrebe, W. & Heeren, F. (1999): Subduction erosion along the North Chile margin. *J. Geodynamics*, 27:345–358.
- Vozoff, K. (1991): The Magnetotelluric Method. In Nabighian, M. N., editor, *Electromagnetic Methods in Applied Geophysics – Applications*, volume 2B, chapter 8, pages 641–711. Soc. Explor. Geophys., Tulsa, Okla.

- Weckmann, U. (1999): *Audiomagnetotellurikmessungen im Nördlichen Spessart*. Diploma thesis. University of Frankfurt, Inst. f. Meteorology and Geophysics.
- Weidelt, P. (1985): Construction of conductance bounds from magnetotelluric impedances. *J. Geophys.*, 57:191–206.
- Wiese, H. (1962): Die Streichrichtung der Untergrundstrukturen des elektrischen Widerstandes, erschlossen aus geomagnetischen Variationen. *Pure and Applied Geophys.*, 52:83–103.
- Wildenschild, D., Roberts, J. J. & Carlberg, E. D. (2000): On the relationship between microstructure and electric and hydraulic properties of sand-clay mixtures. *Geophys. Res. Letters*, 27(19):3085–3088.
- Wojtal, S. F. (1994): Fault scaling laws and the temporal evolution of fault systems. *J. Structural Geology*, 16(4):603–612.
- Wojtal, S. F. (2001): The nature and origin of asymmetric arrays of shear surfaces in fault zones. In Holdsworth, R. E., Strachan, R. A., Magloughlin, J. F. & Knipe, R. J., editors, *The Nature and Tectonic Significance of Fault Zone Weakening*, volume 186 of *Geological Society, Special Publications*, pages 171–193. London.
- Woodcock, N. H. (1986): The role of strike-slip fault systems at plate boundaries. *Philos. Trans. Royal Soc. London Abstracts*, 317:13–29.
- Yáñez, G., Mpodozis, C. & Tomlinson, A. (1994): Eocene dextral oblique convergence and sinistral shear along the Domeyko fault system: A thin viscous sheet approach with asthenospheric drag at the base of the crust. In *7th Congreso Geológico Chileno*, volume 2, pages 1478–1482, Concepción.
- Yu, G., Wesnousky, S. G. & Ekström, G. (1993): Slip partitioning along major convergent plate boundaries. *PAGEOPH*, 140(2):183–210.
- Zang, A., Wagner, C., Stanchits, S., Janssen, C. & Dresen, G. (2000): Fracture process zone in granite. *J. Geophys. Res.*, 105:23 6511–23 661.
- Zonenshayn, L. P., Savostin, L. & Sedov, A. (1984): Global paleogeodynamic reconstruction for the last 160 million years. *Geotectonics*, 18:181–195.

## Acknowledgements

I wish to thank Prof. Dr. G. Dresen for providing me with an interesting research topic and for support and advice throughout the course of this investigation. I also thank Dr. C. Janssen, with whom I spent many weeks in the field and who was always ready to discuss the findings of this work.

This project would not have been possible without the strong support of Prof. Dr. V. Haak and the Electromagnetic Deep Sounding group at GFZ (PB.2.3). I particularly wish to thank Dr. O. Ritter and Dr. U. Weckmann for their continuous advice whatever practical and theoretical problems arose. They helped during the preparation of the MT-experiment and provided an extensive program package for the data processing. Dr. O. Ritter was furthermore present during the startup of the MT-experiment in Chile and helped coping with the unavoidable initial problems. The MT-instruments were gratefully provided by the GFZ GIPP.

Another source of expertise on electromagnetic theory and field campaign logistics is located at the Free University of Berlin. I am grateful for the support of Dr. H. Brasse, W. Soyer and S. Tauber in particular. Special thanks to Wolfgang for his assistance in the MT field campaign.

The cooperation with and help of many colleagues in Chile was crucial for the outcome of this work. I wish to thank Dr. H. Wilke of the Universidad Catolica del Norte for practical support in organising the field campaigns. Thank's to him and his family for a wonderful Christmas '99 and for many other occasions. I am obliged to the late Dr. G. Behn and Dr. L. Baeza of CODELCO who gave most valuable advice and information regarding the study area. The Calama division of CODELCO additionally provided space for our equipment. Furthermore, I am thankful to Eduardo Cisternas who helped with the geological fieldwork (not to forget the delicious dinners at his sisters family Fabiola and Christian Teraldo in Chuquicamata), and to Pablo Salazar and Liey-si Wong who helped during the MT field work.

I should also like to thank Dr. A. Tomlinson of SERNAGEOMIN for providing information on the West Fault system and Dr. Daryl Lindsay (CODELCO) who guided a tour to the West Fault in the Chuquicamata open pit mine. Thanks to Dr. Andreas Günther for providing us with some GPS-locations of impressive outcrops at the West Fault.

Back home, my thanks go to Dr. P. Dulski, Dr. V. Lüders, R. Naumann and Dr. G. Schettler who transformed the rock samples into important geochemical data. I am furthermore thankful to Dr. G. Nover for finding time to analyse some rock samples, too. Dr. M. Rother is thanked for his patience in solving 'mystical' computer network problems.

Many thanks to Dr. C. Janssen, Dr. O. Ritter, Dr. E. Rybacki, and Dr. U. Weckmann, who volunteered to read and correct parts of this thesis and of whom I received many valuable comments.

In that context I am much obliged to the reviewers who have to deal with the *final* version of the thesis: Prof. Dr. G. Dresen, Prof. Dr. V. Haak and Dr. habil T. Ryberg.

I have to mention two platforms of discussion that helped not to loose the broader context of this study: Thanks to the members of the SFB267 seminars and workshops and to participants of the MT seminar.

Never underestimate the importance of the non-geoscientific environment. I am grateful to Ruth ter Huerne and my family, of course, for providing me with the essential spirit to bring this work to an end. Not to be forgotten: thanks to a bunch of great people at GFZ/PIK/FU/PU . . .

This thesis was accomplished with the financial support of the German Scientific Foundation (DFG) within the framework of the Sonder Forschungs-Bereich (SFB) 267 » Deformation processes in the Andes«.

## Curriculum vitae

Name: Arne Hoffmann-Rothe  
Born: 24.02.1973, Tripolis / Libya  
Citizenship: German

### School

1979 – 1983 Primary school in Essen, Germany  
1983 – 1988 Grammar school (Gymnasium)  
German International School Jakarta, Indonesia  
1988 – 1992 Grammar school (Gymnasium) Essen, Germany, Degree: Abitur

### University

1992-1999 University of Bonn, Germany, Department of Geology  
Degree: Diploma in Geology (with main focus on Geophysics)  
Diploma Thesis (Uni Bonn, GFZ Potsdam):  
2D- and 3D-modelling and interpretation of magnetotelluric and geo-  
magnetic data from Central-Java, Indonesia.  
1995-1996 University of Edinburgh, Scotland, Grant Institute  
Scholarship of the German Academic Exchange Service (DAAD)

### Career

1999-2002 Scientist in Sonderforschungsbereich 267 »Deformation processes in the Andes« at the GeoForschungsZentrum Potsdam, Germany; Department 3.2 »Rheology and Tectonophysics« (Prof. Dr. Georg Dresen)

# Geological map of the Gorila region

Geology based on: Maksaev, V., Dilles, H. H. and Tomlinson, A. J., 1999: Mapa geológico del Cuadrángulo Cerros de Paqui, Región

**Map symbols**

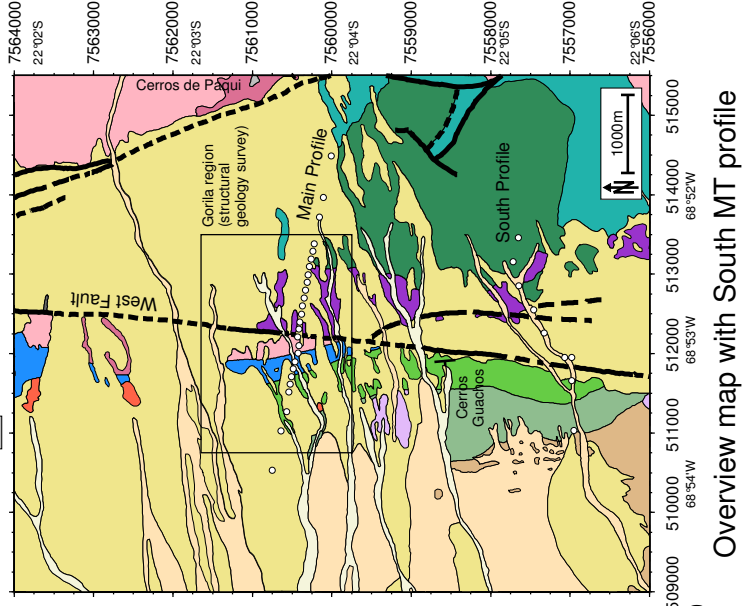
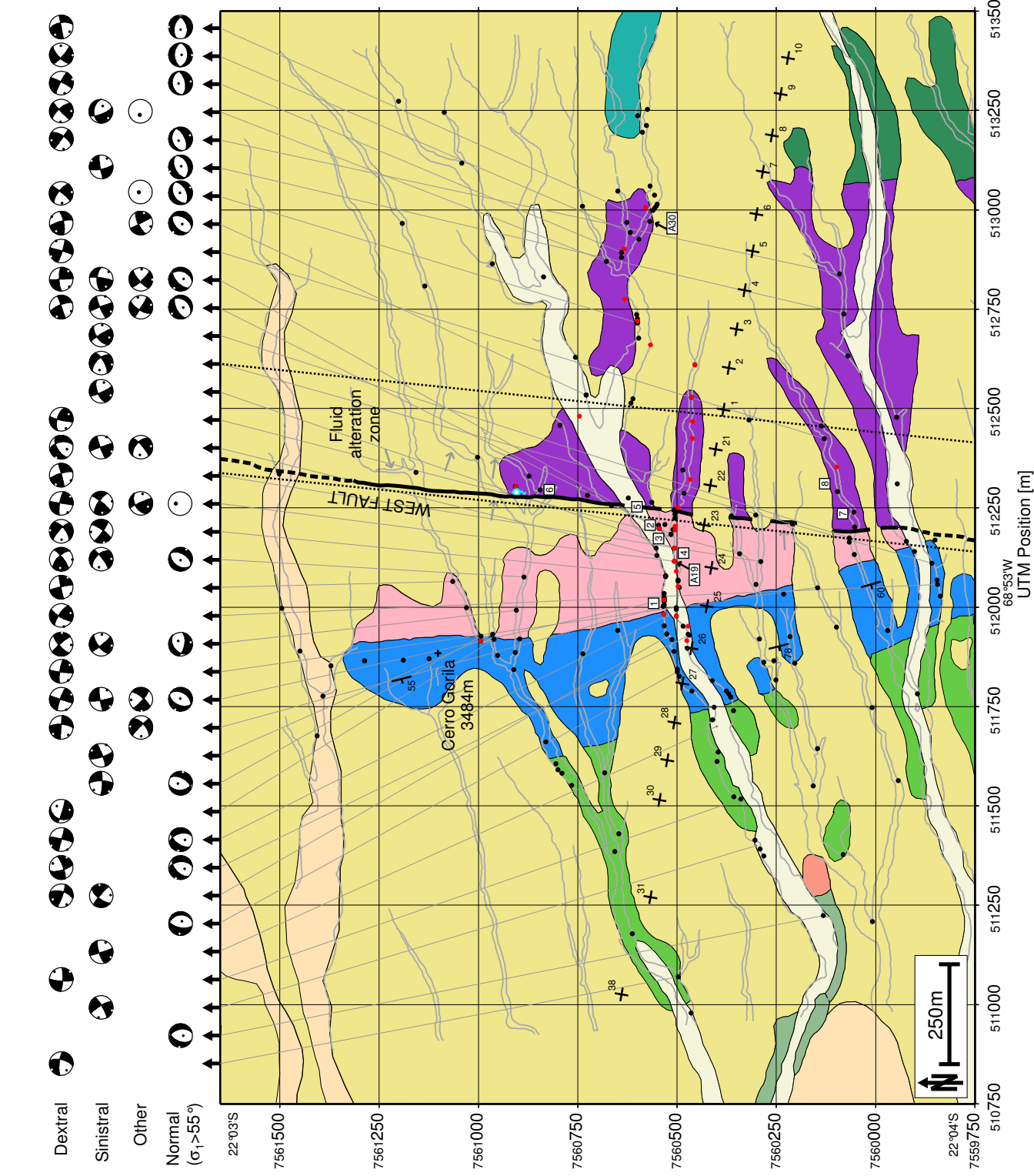
- Drainage valleys
- WF parallel segments
- Bedding
- Faults / inferred
- Photo locations (Appx. A.3.)
- Sites of structural investigation
- Sample sites for geochemical analysis
- Cold spring on West Fault
- MT / GDS Site; O on overview map

**Formación**

Quatern.	Aluvial deposits, not consolidated
Pliocene - Pleisto.	Aluvial deposits, not consolidated
E. Mio- Pliocene	Piedmont deposits
Icanche	Andesites, Dacites
Cerro Empexa	Lavas, porphyric Andesites, Pyroclastics
Tolar	Sedimentary breccias, conglomerates
	Sandstones
	Conglomerates
Late Cretaceous - Eocene	Limestone, calcareous pelites and sandstones with marine fossils
Jurassic	Limestone, calcareous pelites and sandstones with marine fossils
Carbon. - Perm. Triassic	Rhyolites and Dacites
	Andesites
INTRUSIVES	Monzodiorite, quartziferous, Eocene (two different generations)
	Porphyric Andesite, Eocene
	Granodiorite, Triassic

*erosion unconformity*

Quehuila  
Collahuasi



UTM Position [m]

Overview map with South MT profile